SINGLE-MOLECULE FLUORESCENCE STUDIES OF METALLOREGULATORS, METALLOENZYMES, AND NANOCATALYSTS

A Dissertation

Presented to the Faculty of the Graduate School

of Cornell University

In Partial Fulfillment of the Requirements for the Degree of

Doctor of Philosophy

by

Nesha May Octavio Andoy

January 2011

SINGLE-MOLECULE FLUORESCENCE STUDIES OF METALLOREGULATORS, METALLOENZYMES, AND NANOCATALYSTS

Nesha May Octavio Andoy, Ph. D.

Cornell University 2011

This work presents the development and application of single-molecule fluorescence-based methodologies to study bio-inorganic systems and catalysis of nanostructured materials. Single-molecule fluorescence microscopy was used to examine: (i) protein-DNA interactions using single-molecule fluorescence resonance energy transfer (smFRET), (ii) single-molecule enzymology of tyrosinase using fluorescence quenching via energy transfer, and (iii) structure-activity correlation of gold nanoparticle catalysis using super-resolution imaging.

Engineered DNA Holliday junction (HJ) was used as the smFRET reporter for interactions of a metalloregulator, CueR, with DNA for transcriptional regulation. Both the apo- and holo-forms of CueR interact with and change the structures and dynamics of interconversion between the two conformations of the HJ. Single-molecule kinetic analyses revealed differences between apo- and holo- CueR in their interactions with DNA. These changes observed on HJ upon CueR binding reflect the protein actions on DNA for regulating gene transcription.

The single-molecule enzymology of tyrosinase was also investigated. Catalysis coupled fluorescence quenching (CCFQ) was used to monitor the state of the binuclear-copper active site of the enzyme. The intermediates of this metal center exhibit different absorption features as the enzyme goes through the catalytic cycle. Using a fluorescent probe whose fluorescence spectrum overlaps with the absorption

spectrum of one of the intermediates of the active site, the state of the active site of the enzyme was directly monitored.

The structure-activity correlation of single nanoparticle catalysts was achieved by applying super-resolution fluorescence imaging on single-particle catalysis. The generation of a fluorescent product from a non-fluorescent reactant on the surface of nanoparticles was imaged using single-molecule fluorescence microscopy. Precise nanometer localization of where the products are generated, with a resolution of ~25 nm, was obtained by fitting the point spread function of the emission of a product molecule with a two-dimensional Gaussian function. By taking the SEM image of the same nanoparticles and overlaying them to those obtained from super-resolution imaging, direct correlation of the activity and structure of nanocatalysts was achieved at the single-particle level.

BIOGRAPHICAL SKETCH

Nesha May Andoy received her B.S. in Chemistry in 2001 from the University of the Philippines in Diliman. She studied the biodesulfurization products of dibenzothiophene using R. erythropolis in the presence of Tween-80 and Triton X-100 detergents in her undergraduate research under the supervision of Prof. James Villanueva. She then joined the faculty of the Institute of Chemistry in the same university as an instructor after finishing her undergraduate degree.

In 2005, she moved to Cornell University as a graduate student and joined the group of Peng Chen. There, she applied single-molecule fluorescence detection to study protein-DNA interactions, enzymology of tyrosinase, and to spatially resolve catalysis on individual gold nanoparticles. Her research on the use engineered DNA Holliday junctions to study the dynamics of protein-DNA interactions was featured on the cover of the Biophysical Journal in August 2009, and also in the Natural Product Reports for their 5th issue in 2010. She is also a recipient of the 2010 Tunis Wentink Prize award for outstanding academic and research performance.

Outside the lab, she plays the banduria, a 14-string instrument that is part of the Rondalla ensemble. She has been a member of 14 Strings! Cornell Filipino Rondalla since she saw their very first performance in the spring of 2008.

To my Lola Ramona

ACKNOWLEDGMENTS

Any task of this enormity would have been impossible if not for the help and guidance of those who supported me throughout my graduate school life. I owe my deepest gratitude to my supervisor Peng Chen whose help has been instrumental in my journey as a researcher. His passion and enthusiasm for research and his zeal for exploring challenging frontiers and addressing key scientific problems have taught me the qualities of a good scientist. He has been very supportive and considerate especially at times when I had difficulties in making my experiments work. His concern for his students' well-being is a living example that great scientists can also be good mentors.

I am also grateful to my committee members for all their insightful comments that helped me improve my work. Prof. Tadhg Begley, for his relevant feedbacks during my A exam. Prof. John Marohn, for the very insightful discussions and suggestions during my B exam. Also, for taking the time to carefully read and edit my dissertation. Prof. Barbara Baird, for her invaluable suggestions and useful insights during both my A and B exams, and also for helping me improve my dissertation.

To the members of the Chen group, both past and present. Special thanks to Susanta for showing me the ins and outs of working with Holliday junction and for teaching me how to pay attention to details (how they make a world of difference!). Also, many thanks to Xiachun for helping me with MatLab and for bearing with me every time I have problems with the codes. Thanks to Jaime, his expertise in using the FPLC helped me in many ways during the protein purification process. Guokon, for his help in TEM imaging, and to Hao for sharing with me his quartz slide with etched markers.

To 14 Strings! for all the fun and good music that made graduate life less

stressful. To my kiwar buddies, for making my life in Ithaca gorges! To all my friends, for making my world goes round.

My heartfelt gratitude goes to my family, for all their love and unwavering support. Despite the distance, their prayers and encouragement kept me going all throughout my graduate school years. I never would have made it without them! And most important of all, to God to whom I owe everything!

TABLE OF CONTENTS

LIST OF FIGURES

LIST OF TABLES

CHAPTER ONE

APPLICATIONS OF SINGLE-MOLECULE FLOURESCENCE MICROSCOPY

1.1 Introduction

Advances in optical spectroscopy and microscopy have made it possible to detect, image and conduct spectroscopic measurements on single molecules.[1,2] One of the simplest reasons that makes the single-molecule approach appealing is that it represents detection at the ultimate sensitivity level – detecting *exactly one* molecule in the presence of trillions of solvent/host molecules.[3] Single-molecule detection is also capable of directly measuring the distribution of a molecular property, thus removing the effect of ensemble averaging. [1-4] This capability is useful when the system under study is heterogeneous (e.g. biomolecules and nanoparticles). With direct measurement of the behavior of each member in the ensemble, system heterogeneity that could give rise to functionally relevant subpopulations can be analyzed. In addition, single-molecule measurements remove the need for synchronization to probe the actions of each molecule that undergoes time-dependent processes. [1-4] With proper time resolution, intermediates can be directly probed, and in the case of catalysis new insights into the reaction mechanism can be obtained.

Among the optical techniques in single-molecule detection, single molecule fluorescence microscopy is the most common.[1] This method monitors fluorescence intensity, spectrum, polarization, or lifetime in order to investigate the molecular property of the system.[4] Among these techniques, detecting fluorescence intensity is commonly used. For non-fluorescent molecules, fluorescent probes attached to the molecule of interest enable single molecule fluorescence measurements.

To achieve single molecule detection, fluorescence experiments are done at low fluorophore concentrations (10^{-9} to 10^{-12} M) to spatially separate the individual molecules at distances much larger than the typical diffraction-limited resolution, which is a few hundred nanometers. Also, the signal to noise ratio (SNR) of the collected fluorescence signal is maximized.[1] This is done by confining the excitation and detection to a small volume. Two experimental set-ups are widely used to achieve this goal: confocal fluorescence microscopy and total internal reflection fluorescence (TIRF) microscopy.

The confocal set-up focuses the laser excitation beam to a diffraction-limited volume and uses a pinhole to confine the signal detection around the focus (~300 × 300 × 600 nm^3). It uses point detectors (e.g. avalanche photodiodes) and examines one molecule at a time, with a temporal resolution that can be up to microseconds. In TIRF microscopy, the evanescent field from TIR confines the laser excitation to a thin layer (~50 – 300 nm). It typically uses electron multiplying cameras as detectors, thus its time resolution is limited by the camera's speed, which is about milliseconds. TIRF is slower than confocal microscopy but it can image hundreds of molecules simultaneously.[4]

Single-molecule fluorescence methods have found wide applications, especially in the field of biology. New knowledge is emerging from single-molecule studies of gene expression,[5,6] protein folding,[7,8] motor proteins,[9,10] nucleic acids,[11,12] and many other systems. This methodology has also been applied to study heterogeneous catalysis.[13-17] The following sections present examples of the wide applications of single-molecule fluorescence microscopy.

1.2 Single-molecule fluorescence resonance energy transfer (smFRET) in protein-DNA interactions

Protein-DNA interactions are fundamentally important in regulating gene replication, transcription and recombination.[18] What defines this regulation process is the dynamics of how proteins interact with and change the structure of DNA. Quantifying these dynamic interactions is essential for elucidating the mechanisms of their biological function. Dynamic protein-DNA interactions are challenging to study quantitatively in ensemble experiments due to their highly asynchronous and stochastic nature.[19] Distributions of conformational states are also difficult to determine in ensemble-averaged experiments. Single molecule fluorescence measurements, in particular single-molecule fluorescence resonance energy transfer (smFRET) pioneered by Weiss and Ha,[20,21] have enabled measurements of dynamic protein-DNA interactions and the associated structural changes on proteins and DNA. The use of smFRET in studying protein-DNA interactions elucidated some unprecedented details in the mechanisms of DNA replication and transcription.[19,22-23]

FRET was first observed and described theoretically by Perin and Förster[24] as a process of non-radiative long-range dipole-dipole interaction that leads to transfer of energy from a donor to an acceptor molecule. The rate of energy transfer k_{FRET}:[25]

$$k_{\mathrm{FRET}} = \frac{1}{\tau_D}\left(R_o/R\right)^6 \quad \text{where} \quad R_{\mathrm{o}} = \frac{9000(\ln 10)\kappa^2 Q_D J}{128\pi^5 n^4 N_A} \qquad \text{Equation 1.1}$$

The rate of FRET is a function of the fluorescence lifetime (τ_D, s) and the quantum efficiency (Q_D) of the donor in the absence of the acceptor, the refractive index of the medium (n), Avogadro's number (N_A), the normalized spectral overlap integral (J, $M^{-1}cm^3$), the orientation factor (κ^2; 2/3 for freely rotating chromophores), the Förster distance (the separation at which 50% of the excitation energy is transferred to the

acceptor: R_0, cm), and the distance between the donor and acceptor molecules (R, cm). From Equation (1.1), the FRET transfer efficiency, E_{FRET}, is therefore:

$$E_{FRET} = \frac{1}{1+(R/R_0)^6} \qquad \text{Equation 1.2}$$

$$E_{FRET} = 1-(\Phi_D^A/\Phi_D) = 1-(I_D^A/I_D) = 1-(\tau_D^A/\tau_D) \qquad \text{Equation 1.3}$$

where Φ_D^A and Φ_D are the quantum yields, I_D^A and I_D are the fluorescence intensities, and τ_D^A and τ_D are the lifetimes of the donor in the presence and absence of acceptor, respectively. Equation 1.3 is used to calculate E_{FRET} experimentally.[25]

In a typical FRET experiment, a biomolecule is labeled with a donor-acceptor fluorophore pair at two different locations. The labeling positions are chosen in such a way that the internal motion of a molecule would change the distance between the two fluorophores within the range of FRET sensitivity. This distance range lies within the Förster radius by a factor of two (e.g. ~ 2 - 6 nm for FRET pair with R_0 = 4 nm).[25] Due to this inherent mechanism of FRET and the suitable probes that can be used in single molecule detection, smFRET methods rely largely on detecting nanometer-scale distance changes (Figure 1.1).[20,21] However, many DNA-binding proteins such as the MerR-family regulators may not cause DNA structural changes of large enough magnitude for conventional smFRET to detect.[26]

Recently, we have developed engineered DNA Holliday junctions (HJ), 4-way DNA junctions, as single-molecule reporters in smFRET measurements to study protein-DNA interactions.[19] As the effects of protein actions on DNA are converted to the changes in the structure and dynamics of HJ, interactions that are weak and only involve small structural changes can be studied by this method. We have used this methodology to study interactions of PbrR691 protein, a Pb^{2+} responsive member of

the MerR-family, and we have shown that engineered HJs can probe how PbrR691 interacts with DNA. Changes in the structure and dynamics of the HJ were observed upon protein binding. Being able to quantify these changes simultaneously with protein binding provides a new opportunity to elucidate the correlation between structure, dynamics, and function of DNA-binding proteins. In Chapter 2 of this dissertation, the use of engineered HJ to study the protein-DNA interactions of a Cu^{1+}-responsive metalloregulator, CueR, is presented.

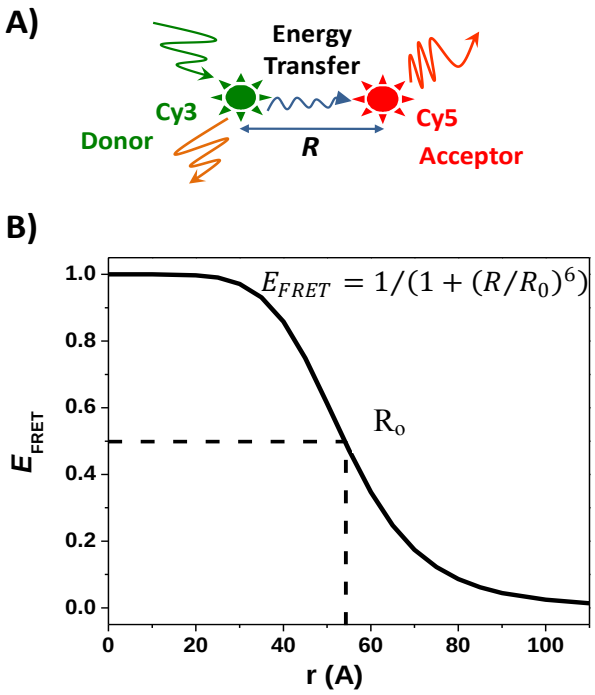

Figure 1.1 (A) Scheme of fluorescence resonance energy transfer (FRET) for a single pair of donor (Cy3) and acceptor (Cy5), two fluorophores commonly used as a FRET pair in single-molecule experiment. (B) Theoretical distance dependence of E_{FRET} value for Cy3-Cy5 FRET pair generated using Equation 1.2 using R_o = 55 nm.

1.3 Single-molecule enzymology

A continuing challenge in enzymology is to understand the contribution of conformational dynamics to enzyme function.[27] As expected from the known stability of folded proteins, most enzymes should transition between different conformational states with different reactivity. [28-29] We would thus expect many enzymes to switch from a fully active conformation to less active forms (and back) while undergoing catalysis. This would give rise to a highly dynamic enzyme molecule that has time-dependent catalytic properties (so-called dynamic disorder). Although ensemble assays have provided a great wealth of information about enzymes, probing these time-dependent heterogeneities could be very challenging for conventional bulk measurements since they would be lost in ensemble averaging.[27,30-31] Following the catalytic activity of individual enzyme molecules is therefore necessary for these time-dependent fluctuations to be resolved.[4,27,30-43]

In addition to dynamic disorder, enzymes are known to have static heterogeneity, where identical copies of enzyme molecules display different catalytic properties.[30,31,42] It has been shown that enzyme activity can vary and sometimes the range can span an order of magnitude.[29,44,45] Since single-molecule detection can directly measure the distribution of molecular properties, subpopulations due to this static heterogeneity can be resolved by single-molecule measurements which would be otherwise masked by ensemble averaging.

Enzymatic reactions are moreover typically unsynchronized, that is, each molecule at a given point in time is at a different stage of the reaction sequence.[30] As a consequence, the steady-state concentrations of transient intermediates are usually too low to be detected.[42] It is therefore necessary, for bulk experiments, to synchronize the enzymatic reaction in order to probe reaction intermediates in the enzyme's mechanism. Singe molecule experiments, on the other hand, allow the direct

observation of the individual steps or intermediates of enzymatic reactions without the need for synchronization. It can therefore permit the observation of transient intermediates that could sometimes be lost in ensemble measurements.[27,30,31,42]

Many innovative strategies have been recently developed for carrying out single-molecule enzymology experiment.[27,31] The single-enzyme study done by Xie and coworkers is one of the best examples showing the wealth of information uncovered by using single-molecule methods to study enzyme reactions.[46] In their work, they utilized the intrinsic fluorescence properties of the flavin adenine dinucleotide (FAD) active site to study the catalytic dynamics of cholesterol oxidase (COx) (Figure 1.2 upper panel). The real-time single turnover trajectories (Figure 1.2 lower panel) obtained allowed them to analyze the time-dependent activity of each enzyme. They found that individual COx molecules show temporal activity fluctuations (i.e., dynamic disorder), which they attributed to slow conformational dynamics of the enzyme. The timescale of the conformational dynamics could be obtained from the decay constant of the autocorrelation function of the waiting times which equals the time scale of the activity fluctuations. This experiment established that dynamics-coupled enzyme catalysis is a fundamental characteristic of enzymatic reactions.

This approach of probing a fluorescent active site, which was also used by Palfey, Steel, Gafni and coworkers to study dihydroorotate dehydrogenase[47] and p-hydroxybenzoate hydroxelase,[48] is one of the fluorescence methods that have been utilized in single molecule enzymology. Another strategy is to observe a fluorogenic reaction in which a non-fluorescent substrate is catalytically converted to a fluorescent product. This is the most popular approach in single-molecule enzymology. Two experimental designs have been used to date: (1) detect the generation of every product molecule at a single-turnover resolution[34,36,49-51] and (2) monitor the

accumulation of product molecules produced by a single encapsulated enzyme over time[44,45]. Besides detecting the fluorescent product, a fluorescent substrate can also be used in singe-molecule enzymology. For this strategy, one can use either naturally fluorescent molecules or fluorescently-labeled substrate molecules.[52]

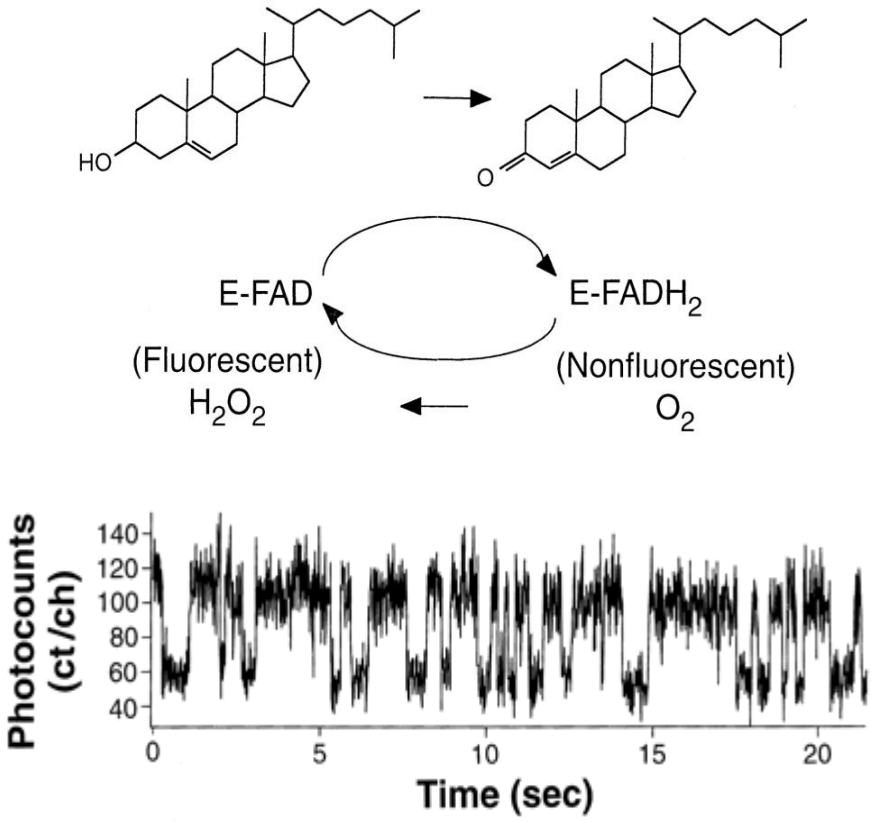

Figure 1.2 Enzymatic cycle of cholesterol oxidase (COx), top, and real time observation of enzymatic turnovers of a single COx molecule, bottom. Each on-off cycle in the fluorescence intensity trajectory corresponds to a single enzymatic turnover. In the y-axis, ct/ch stands for counts per channel. Reprinted with permission from Ref. [46]. Copyright 1998 American Association for the Advancement of Science.

FRET is another approach widely used to monitor single enzyme catalysis. This method utilizes the nanometer-scale distance changes between parts of an enzyme molecule accompanying a catalytic reaction. A fluorescent donor-acceptor pair is attached to the appropriate locations on the enzyme and the fluctuations in energy transfer between the probes report on the enzymatic turnovers. This methodology has been used by Weiss and coworkers in a study of the conformational dynamics and reaction mechanism of staphylococcal nuclease.[53]

Fluorescence quenching via energy transfer has also been used to study enzyme reactions. Instead of using a FRET pair, only one fluorescent probe is introduced and acts as the donor. The acceptor, either a substrate or intrinsic to the enzyme, is nonfluorescent and acts as a quencher – it has strong absorption bands that overlap spectrally with the fluorescence of the donor. The resulting quenching by the acceptor changes the donor fluorescence, from which the chemical state of the acceptor (enzyme or enzyme-bound substrate) can be deduced. This method has been applied to study substrate binding and catalysis of dihydrofolate reductase.[43,54] Canters and coworkers used this method in a study in which the metal co-factor (type-1 copper site) of nitrite reductase was used as the natural quencher.[55]

1.4 Single-molecule super-resolution optical imaging

It is well known that diffraction effects limit the resolution of standard optical microscopy to a dimension defined by the Rayleigh criterion:[56]

$$d_r = \frac{0.61\lambda}{N.A.} \qquad \text{Equation 1.4}$$

where d_r is the minimum distance by which two objects can be resolved; λ the optical wavelength; and *N.A.* is the numerical aperture of the objective lens. In a typical

experiment, d_r is roughly half of the wavelength, λ, or ~250 nm for visible light of 500 nm wavelength. This Rayleigh resolution limit renders conventional optical imaging methods not useful for high resolution imaging. Unfortunately, most systems especially in the field of molecular biology and nanocatalysis, have interesting features having dimensions smaller than the diffraction limit.

Great progress has been made to overcome this diffraction limit in optical imaging. Technological advances in optical spectroscopy and single molecule detection have led to the development of techniques capable of producing optical images with resolution beyond the diffraction limit.[57-62] These methods are known as "super-resolution optical imaging". These methods produce optical images having spatial resolutions as high as ~10 nm. These super-resolution methods include near field microscopy, which can achieve resolution down to ~12 nm.[63] Other techniques use nonlinear effects to sharpen the point-spread function of the microscope, including stimulated emission depletion (STED) and the related concept of ground-state depletion (GSD) microscopy, which can achieve resolution as high as ~30-40nm.[64-66] In addition, saturated structured illumination microscopy (SSIM) and reversible saturable optical linear fluorescence transitions (RESOLFT) can achieve a resolution of <50 nm and 100 nm, respectively.[67]

Recent advances in single-molecule fluorescence microscopy have provided a way to achieve resolution even closer to the molecular scale.[60-62,68-71] Techniques have been developed to localize the position of a single emitting molecule with nanometer precision. Such high-accuracy localization is possible because even though the details within a diffraction limited spot is not resolvable under optical fluorescence imaging, the center of its emission pattern, and hence the location of the emitter, can be determined to a much greater precision.[61,62] This precision is achieved by fitting the point spread function (PSF) of the fluorescence image to a two-dimensional Gaussian

function.[72] Selvin and coworkers applied this precise localization methodology to unravel the "walking mechanism" of a molecular motor, myosin, using FIONA (fluorescence imaging with one nanometer accuracy).[62] The precision of localization is determined by the standard error of the mean (σ) of the PSF and was theoretically derived by Webb and coworkers:[61]

$$\sigma_i = \sqrt{\frac{s_i^2 + a^2/12}{N} + \frac{8\pi s_i^4 b^2}{a^2 b N^2}} \qquad \text{Equation 1.5}$$

where s_i is the standard deviation of the Gaussian function, a is the pixel size, N is the number of collected photons and b is the background noise in photon counts. This analytical expression indicates that a more precise localization can be achieved by collecting more photons and minimizing the background noise. This localization, however, does not work if multiple emitters are in close proximity, for their PSFs will overlap making it difficult to resolve their locations. This problem has been partly addressed by making use of the natural blinking of quantum dots[59,73] and the photobleaching of fluorophores, like in NALMS (nanometer-localized multiple single-molecule) fluorescence microscopy, where a few (2-5) molecules have been resolved in a diffraction limited spot.[74,75] However, it becomes increasingly challenging to apply these methods to higher number of fluorophores.[58]

Resolving many emitters located within a diffraction-limited spot has recently been achieved by applying high-precision localization of probes that can be actively photoswitched between a fluorescent and a dark state.[57,58,60,71] To isolate the location of a single molecule from this otherwise overlapping fluorescence images, the fluorescence from each emitter is separated in the time domain before localization analysis is performed. A few fluorophores, well separated from each other, are activated at different time points so they can be localized with high precision. They are

then photobleached (or photoswitched to their dark state) before another set of fluorophores are activated. This serial photoactivation and subsequent bleaching of numerous sparse subsets of photoactivable fluorophores gives data which can be recombined to yield a super-resolution image of the system of interest.[58]

Three different techniques using single-molecule super-resolution fluorescence microscopy were developed independently and published almost at the same time in 2006.[57,60,71] These are (1) stochastic optical reconstruction microscopy (STORM),[60] (2) photoactivated localization microscopy (PALM)[57] and (3) fluorescence photoactivation localization microscopy (FPALM)[71]. All these methods construct a high-resolution image from locations of individual photoactivable organic dyes (STORM) or fluorescent proteins (PALM and FPALM) that turn on and off by light of different wavelengths. By controlling the fraction of fluorophores that get activated (by modulating the intensity of the activating laser), such that their fluorescence images are not overlapping, the positions of these fluorophores can be determined with high precision. Repeating this imaging cycle allows the positions of many fluorophores to be localized and thus the whole image can be constructed with very high resolution (~10-20 nm).[57,58,60,71]

These single-molecule super-resolution optical imaging techniques have mostly been used to study biological systems but recent developments in single-molecule heterogeneous catalysis have paved the way to apply these high resolution imaging methods to visualize single-molecule electrocatalysis on carbon nanotubes.[76] Super-resolution imaging of the fluorescent product formation showed that the reaction occurs at discrete, nanometer-dimension sites on single-walled carbon nanotube. This methodology has also been applied to spatially resolve the reactive sites on zeolite particles.[16] The results showed that zones of different activity exist within a single zeolite rod particle which would otherwise be smeared out in

conventional fluorescence imaging.

1.5 Scope of the thesis

Single-molecule TIRF microscopy was used for all experiments presented in this dissertation. With its high data throughput, TIRF microscopy was used to study protein-DNA interactions involved in metal regulation (Chapter 2), single molecule enzymology of tyrosinase probing the metal active site (Chapter 3), and super-resolution imaging of the reactivity on gold nanoparticles (Chapter 4).

In Chapter 2, engineered HJ was used to study CueR, a Cu^{1+}-responsive member of the MerR-family, binding with its DNA substrate. The application of this methodology to CueR corroborated the general applicability of using engineered HJs as smFRET reporters for protein-DNA interactions. Results from single-molecule experiments on CueR-HJ interactions revealed similarities and differences in the mechanism of transcription activation and suppression of members of the MerR-family of regulators.

For Chapter 3, fluorescence quenching via energy transfer was applied to study the single molecule enzymology of tyrosinase. Utilizing the spectroscopic features of its metal active site, single enzymatic turnover was monitored via catalysis-coupled fluorescence quenching (CCFQ) of a fluorescent probe attached near the enzyme's active site. The single-molecule fluorescence intensity fluctuation of each probe monitors the enzymatic reaction in real-time.

In Chapter 4, the application of super-resolution imaging on nanoparticle catalysis is presented. The high spatio-temporal resolution and sensitivity of single-molecule super-resolution fluorescence microcopy makes it ideal for *in situ* studies of nanometer sized catalysts. Together with scanning electron microscopy (SEM), the structure-activity correlation of individual nanocatalyst is explored. The structure-

activity correlation obtained from this combination of SEM imaging and super-resolution fluorescence microscopy provides insights into the fundamental principles of nanocatalysis that could help to improve current nanocatalysts and design new ones.

Chapter 5 summarizes the entire thesis and also includes recommendations for future work.

REFERENCES

(1) Moerner, W. E.; Fromm, D. P. *Rev. Sci. Instrum.* **2003**, *74*, 3597-3619.

(2) Xie, X. S.; Trautman, J. K. *Annual Review of Physical Chemistry* **1998**, *49*, 441-480.

(3) Moerner, W. E. *The Journal of Physical Chemistry B* **2002**, *106*, 910-927.

(4) Chen, P.; Andoy, N. M. *Inorganica Chimica Acta* **2008**, *361*, 809-819.

(5) Cai, L.; Friedman, N.; Xie, X. S. *Nature* **2006**, *440*, 358-362.

(6) Yu, J.; Xiao, J.; Ren, X.; Lao, K.; Xie, X. S. *Science* **2006**, *311*, 1600-1603.

(7) Deniz, A. A.; Laurence, T. A.; Beligere, G. S.; Dahan, M.; Martin, A. B.; Chemla, D. S.; Dawson, P. E.; Schultz, P. G.; Weiss, S. *Proceedings of the National Academy of Sciences of the United States of America* **2000**, *97*, 5179-5184.

(8) Rhoades, E.; Cohen, M.; Schuler, B.; Haran, G. *J. Am. Chem. Soc.* **2004**, *126*, 14686-14687.

(9) Yildiz, A.; Selvin, P. R. *Accounts of Chemical Research* **2005**, *38*, 574-582.

(10) Yildiz, A.; Forkey, J. N.; McKinney, S. A.; Ha, T.; Goldman, Y. E.; Selvin, P. R. *Science* **2003**, *300*, 2061-2065.

(11) McKinney, S. A.; Declais, A. C.; Lilley, D. M. J.; Ha, T. *Nat. Struct. Biol.* **2003**, *10*, 93-97.

(12) Zhuang, X. *Annu. Rev. Biophys. Biomol. Struct.* **2005**, *34*, 399-414.

(13) Xu, W.; Kong, J. S.; Yeh, Y.-T. E.; Chen, P. *Nature Mater.* **2008**, *7*, 992-996.

(14) Xu, W.; Shen, H.; Kim, Y. J.; Zhou, X.; Liu, G.; Park, J.; Chen, P. *Nano Lett.* **2009**, doi:10.1021/nl900988f.

(15) Zhou, X. C.; Xu, W. L.; Liu, G. K.; Panda, D.; Chen, P. *Journal of the*

American Chemical Society, *132*, 138-146.

(16) Roeffaers, M. B. J.; De Cremer, G.; Libeert, J.; Ameloot, R.; Dedecker, P.; Bons, A. J.; Buckins, M.; Martens, J. A.; Sels, B. F.; De Vos, D. E.; Hofkens, J. *Angewandte Chemie-International Edition* **2009**, *48*, 9285-9289.

(17) Shen, H.; Xu, W. L.; Chen, P. *Physical Chemistry Chemical Physics*, *12*, 6555-6563.

(18) Cooper, G. M. *The Cell, A Molecular Approach*; 1st ed.; ASM Press: Washington, 1997.

(19) Sarkar, S. K.; Andoy, N. M.; Benitez, J. J.; Chen, P. R.; Kong, J. S.; He, C.; Chen, P. *J. Am. Chem. Soc.* **2007**, *129*, 12461-12467.

(20) Ha, T. *Methods* **2001**, *25*, 78-86.

(21) Weiss, S. *Science* **1999**, *283*, 1676-1683.

(22) Ha, T. *Biochemistry* **2004**, *43*, 4055-4063.

(23) Myong, S.; Rasnik, I.; Joo1, C.; Lohman, T. M.; Ha, T. *Nature* **2005**, *437*, 1321-1325.

(24) Forster, T. *Discussions of the Faraday Society* **1959**, 7-17.

(25) van der Meer, B. W.; Coker, G., III; Chen, S.-Y. S. *Resonance Energy Transfer: Theory and Data*; VCH Publishers, Inc.: New York, 1994.

(26) Hobman, J. L.; Wilkie, J.; Brown, N. L. *BioMetals* **2005**, *18*, 429-436.

(27) Chen, P.; Andoy, N. M. In *Comprehensive Natural Products Chemistry II Chemistry and Biology*; Mander, L., Lui, H.-W., Eds.; Elsevier: Oxford, 2010; Vol. 9, p 751-769.

(28) Bagshaw, C. R. *The Biochmemist* **2003**, *25*, 24-27.

(29) Engelkamp, H.; Hatzakis, N. S.; Hofkens, J.; De Schryver, F. C.; Nolte, R. J. M.; Rowan, A. E. *Chemical Communications* **2006**, 935-940.

(30) Smiley, R. D.; Hammes, G. G. *Chemical Reviews* **2006**, *106*, 3080-3094.

(31) Xie, S. N. *Single Molecules* **2001**, *2*, 229-236.

(32) Antikainen, N. M.; Smiley, R. D.; Benkovic, S. J.; Hammes, G. G. *Biochemistry* **2005**, *44*, 16835-16843.

(33) Brender, J. R.; Dertouzos, J.; Ballou, D. P.; Massey, V.; Palfey, B. A.; Entsch, B.; Steel, D. G.; Gafni, A. *J. Am. Chem. Soc.* **2005**, *127*, 18171-18178.

(34) Edman, L., FiSldes-Papp, Z., Wennmalm, S. & Rigler, R. *Chem. Phys.* **1999**, *247*, 11-22

(35) Edman, L.; Rigler, R. *Proceedings of the National Academy of Sciences of the United States of America* **2000**, *97*, 8266-8271.

(36) English, B. P.; Min, W.; van Oijen, A. M.; Lee, K. T.; Luo, G.; Sun, Y.; Cherayil, B. J.; Kou, S. C.; Xie, X. S. *Nat. Chem. Biol.* **2005**, *2*, 87 - 94

(37) Kuznetsova, S.; Zauner, G.; Aartsma, T.; Engelkamp, H.; Hatzakis, N.; Rowan, A. E.; Nolte, R. J. M.; Christianen, P. C. M.; Canters, G. W. *Proceedings of the National Academy of Sciences of the United States of America* **2008**, *105*, 3250-3255.

(38) Lu, H. P.; Xun, L. Y.; Xie, X. S. *Science* **1998**, *282*, 1877-1882.

(39) Min, W.; English, B. P.; Luo, G.; Cherayil, B. J.; Kou, S. C.; Xie, X. S. *Acc. Chem. Res.* **2005**, *36*, 923-931.

(40) Qian, H.; Elson, E. L. *Biophysical Chemistry* **2002**, *101*, 565-576.

(41) Velonia, K.; Flomenbom, O.; Loos, D.; Masuo, S.; Cotlet, M.; Engelborghs, Y.; Hofkens, J.; Rowan, A. E.; Klafter, J.; Nolte, R. J. M.; de Schryver, F. C. *Angewandte Chemie-International Edition in English* **2005**, *44*, 560-564.

(42) Xie, X. S.; Lu, H. P. *Journal of Biological Chemistry* **1999**, *274*, 15967-15970.

(43) Zhang, Z.; Rajagopalan, P. T. R.; Selzer, T.; Benkovic, S. J.; Hammes, G. G. *Proc. Natl. Acad. Sci. USA* **2004**, *101*, 2764-2769.

(44) Craig, D. B.; Arriaga, E. A.; Wong, J. C. Y.; Lu, H.; Dovichi, N. J. *Journal of*

the American Chemical Society **1996**, *118*, 5245-5253.

(45) Xue, Q.; Yeung, E. S. *Nature* **1995**, *373*, 681-683.

(46) Lu, H. P.; Xun, L. Y.; Xie, X. S. *Science* **1998**, *282* 1877-1882

(47) Shi, J.; Dertouzos, J.; Gafni, A.; Steel, D.; Palfey, B. A. *Proceedings of the National Academy of Sciences* **2006**, *103*, 5775-5780.

(48) Brender, J. R.; Dertouzos, J.; Ballou, D. P.; Massey, V.; Palfey, B. A.; Entsch, B.; Steel, D. G.; Gafni, A. *J. Am. Chem. Soc.* **2005**, *127*, 18171-18178

(49) Edman, L.; Rigler, R. *Proc. Natl. Acad. Sci. USA* **2000**, *97*, 8266-8271.

(50) Paige, M.; Fromm, D. P.; Moerner, W. E. *Proc. Soc. Photo Opt. Instrum. Engr.* **2002**, *4634*, 92-103

(51) Velonia, K.; Flomenbom, O.; Loos, D.; Masuo, S.; Cotlet, M.; Engelborghs, Y.; Hofkens, J.; Rowan, A. E.; Klafter, J.; Nolte, R. J. M.; de Schryver, F. C. *Angew. Chem., Int. Ed.* **2005**, *44*, 560-564

(52) Funatsu, T.; Harada, Y.; Tokunaga, M.; Saito, K.; Yanagida, T. *Nature* **1995**, *374*, 555-559.

(53) Ha, T.; Ting, A. Y.; Liang, J.; Caldwell, W. B.; Deniz, A. A.; Chemla, D. S.; Schultz, P. G.; Weiss, S. *Proc. Natl. Acad. Sci. USA* **1999**, *96*, 893-898.

(54) Rajagopalan, P. T. R.; Zhang, Z.; McCourt, L.; Dwyer, M.; Benkovic, S. J.; Hammes, G. G. *Proc. Natl. Acad. Sci. USA* **2002**, *99* 13481-13486.

(55) Kuznetsova, S.; Zauner, G.; Aartsma, T.; Engelkamp, H.; Hatzakis, N.; Rowan, A.; Nolte, R.; Christianen, P.; Canters, G. *Proc. Natl. Acad. Sci. USA* **2008**, *105*, 3250-3255.

(56) Born, M.; Wolf, E. *Principles of optics*; Cambridge University Press: Cambridge, 1999.

(57) Betzig, E.; Patterson, G. H.; Sougrat, R.; Lindwasser, O. W.; Olenych, S.; Bonifacino, J. S.; Davidson, M. W.; Lippincott-Schwartz, J.; Hess, H. F.

Science **2006**, *313*, 1642-1645.

(58) Huang, B.; Bates, M.; Zhuang, X. *Annual Review of Biochemistry* **2009**, *78*, 993-1016.

(59) Lidke, K.; Rieger, B.; Jovin, T.; Heintzmann, R. **2005**, - *13*, - 7062.

(60) Rust, M. J.; Bates, M.; Zhuang, X. W. *Nature Methods* **2006**, *3*, 793-795.

(61) Thompson, R. E.; Larson, D. R.; Webb, W. W. *Biophysical Journal* **2002**, *82*, 2775-2783.

(62) Yildiz, A.; Selvin, P. R. *Accounts of Chemical Research* **2005**, *38*, 574-582.

(63) Betzig, E.; Trautman, J. K. *Science* **1992**, *257*, 189-195.

(64) Hell, S. W.; Wichmann, J. *Optics Letters* **1994**, *19*, 780-782.

(65) Hell, S. W. *Science* **2007**, *316*, 1153-1158.

(66) Hell, S. W.; Kroug, M. *Applied Physics B-Lasers and Optics* **1995**, *60*, 495-497.

(67) Gustafsson, M. G. L. *Proceedings of the National Academy of Sciences of the United States of America* **2005**, *102*, 13081-13086.

(68) Ghosh, R. N.; Webb, W. W. *Biophysical Journal* **1994**, *66*, 1301-1318.

(69) Zurner, A.; Kirstein, J.; Doblinger, M.; Brauchle, C.; Bein, T. *Nature* **2007**, *450*, 705-708.

(70) Hell, S. W.; Jakobs, S.; Kastrup, L. *Applied Physics a-Materials Science & Processing* **2003**, *77*, 859-860.

(71) Hess, S. T.; Girirajan, T. P. K.; Mason, M. D. *Biophysical Journal* **2006**, *91*, 4258-4272.

(72) Cheezum, M. K.; Walker, W. F.; Guilford, W. H. *Biophysical Journal* **2001**, *81*, 2378-2388.

(73) Nan, X.; Sims, P. A.; Chen, P.; Xie, X. S. *The Journal of Physical Chemistry B* **2005**, *109*, 24220-24224.

(74) Gordon, M. P.; Ha, T.; Selvin, P. R. *Proceedings of the National Academy of Sciences of the United States of America* **2004**, *101*, 6462-6465.

(75) Qu, X. H.; Wu, D.; Mets, L.; Scherer, N. F. *Proceedings of the National Academy of Sciences of the United States of America* **2004**, *101*, 11298-11303.

(76) Xu, W. L.; Shen, H.; Kim, Y. J.; Zhou, X. C.; Liu, G. K.; Park, J.; Chen, P. *Nano Letters* **2009**, *9*, 3968-3973.

CHAPTER TWO

SINGLE-MOLECULE STUDY OF METALLOREGULATOR CUER-DNA INTERACTIONS USING ENGINEERED HOLLIDAY JUNCTIONS[a]

2.1 Introduction

Metal ions are essential in biology and play key roles in the structure and function of a large number of proteins.[1] Despite their importance, they can also be cytotoxic, especially at high concentrations.[2,3] Intracellular metal ion concentrations and their bioavailability must therefore be tightly regulated to maintain normal cell metabolism. Bacteria, being susceptible to either limiting or toxic levels of metal ions in their living environment, have developed highly sensitive and selective metal homeostasis mechanisms.[3-15] A key step in bacteria's response to varying levels of metal ions in their environment is through metal-sensing regulatory proteins.[4-16] These proteins, also known as metalloregulators, respond to specific metal ions within the cell and regulate gene expression for metal specific homeostasis.[3-6]

A large class of bacterial metalloregulators belongs to the MerR-family; they respond to metal ions such as Hg^{2+}, Pb^{2+} and Cu^{1+} with high selectivity and sensitivity.[4-6,16-22] All MerR-family regulators are homodimers with two DNA-binding domains. They regulate gene transcription via a unique DNA distortion mechanism,[5,17,18,23,24] in which both the apo- and the holo-regulator bind tightly to a dyad-symmetric sequence in the promoter region, with one DNA-binding domain binding to each half of the dyad sequence. In the apo-regulator bound form, DNA is slightly bent and the transcription is suppressed. Upon metal binding, the holo-regulator further unwinds DNA slightly, and transcription is activated. As the

[a] This chapter was reproduced in part with permission from Andoy, N. M., Sarkar, S., Wang, Q., Panda,D., Benitez, J., Kalininskiy, A., and Chen, P. *Biophysical Journal* **2009**, *97*, 844-852. (© 2009 Elsivier).

regulator–DNA interactions dictate the transcription process, there is an interest in defining the associated protein–DNA interactions quantitatively as a fundamental step to understand their detailed structure–dynamics–function relationships.

Single-molecule fluorescence resonance energy transfer (smFRET) measurements are a powerful tool for studying protein–DNA interactions and associated structural changes of proteins and DNA.[25-27] Owing to both the FRET mechanism and the fluorescent probes suitable for single-molecule detection, smFRET relies largely on detecting nanometer-scale distance changes.[25,26] The structural changes associated with MerR-family regulator–DNA interactions are mainly on the angstrom scale, however.[23,24] To detect small structural changes, we recently developed engineered DNA Holliday junctions (HJs) as generalizable single-molecule reporters in smFRET measurements for protein–DNA interaction studies.[28]

The methodology used in this study builds on the intrinsic structural dynamics of DNA HJs and the ease of following the dynamics by smFRET. In the presence of Na^+ and Mg^{2+}, each HJ molecule folds into two X-shaped stacked conformers that interconvert dynamically at room temperature (conf-I and conf-II, Figure 1).[28-33] With a FRET donor-acceptor pair labeled at the ends of two HJ arms, the two conformers have distinct FRET signals, one having high FRET efficiency (E_{FRET}) and the other low E_{FRET}, and their interconversion dynamics are reflected by their two-state FRET fluctuation behaviors.[28,29,31] E_{FRET} is sensitive to both changes in distance and relative orientation of the donor-acceptor pair.[25,26,28] In this study, however, I did not distinguish between changes in distance and relative orientation of the chromophores.

To use a HJ as a single-molecule protein–DNA interaction reporter, I encode in its arms the dyad-symmetric sequence recognized by a metalloregulator (Figure 1). Because the encoded sequence has distinct distance and orientation in the two conformations, the metalloregulator binds to the two conformers differentially and

causes changes in their structures and dynamics, which are readily measurable by smFRET and thus report the associated protein–DNA interactions. Since the effects of protein actions on DNA are converted to -- and amplified by -- the changes in the structures and dynamics of the engineered HJ, small protein-induced structural changes can be studied.[28] Using this approach, we have previously shown that a specifically engineered HJ can report how the Pb^{2+}-responsive MerR-family metalloregulator PbrR691 interacts with DNA.[28] To test the general applicability of this methodology and to gain further insight into the functions of MerR-family regulators, here I extend this engineered HJ approach to examine the actions on DNA of a crystallographically defined Cu^{1+}-responsive MerR-family metalloregulator, CueR, which regulates gene expression for copper resistance in *E. coli*.[34-38]

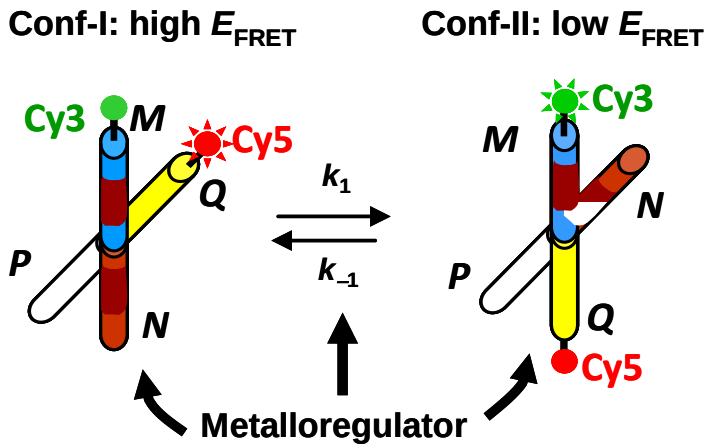

Figure 2.1 Structural dynamics of engineered Holliday junction (HJ) between its two conformers, conf-I and conf-II. Cy3 and Cy5 are labeled at the ends of arms *M* and *Q* to differentiate conf-I (high E_{FRET}) from conf-II (low E_{FRET}). The stripes on arms *M* and *N* indicate the encoded dyad-symmetric sequence recognized by a metalloregulator. Protein binding will perturb both the structures and the dynamic equilibrium of the HJ, which are readily followed by the FRET signal.

2.2 Results and Analysis

2.2.1 CueR-specific engineered HJ

Figure 2.2A shows the design of the engineered Holliday junction, HJC2, targeting the metalloregulator CueR and using four oligo-DNA strands. The sequence of strand **a** is taken from the wild-type promoter that CueR binds, and it contains the CueR-specific dyad-symmetric sequence, which spans the arms *M* and *N*. The ends of arms *M* and *Q* are labeled with the FRET pair, Cy3 (donor) and Cy5 (acceptor), to distinguish between the two stacked conformers of HJC2: conf-I has a higher E_{FRET} and conf-II has a lower E_{FRET} (reference Figure 2.1). A biotin is attached at the end of arm *P* for surface immobilization.[29] The assembly of HJC2 is confirmed by gel electrophoresis in reference to a characterized HJ,[28] and by its absorption spectrum, in which the absorption bands of Cy3 and Cy5 indicate their 1:1 labeling ratio (Figure 2.2A, inset).

The intrinsic structural dynamics of a single HJC2 molecule is clear from its anti-correlated two-state fluorescence intensity fluctuations in both the Cy3-donor and the Cy5-acceptor channel (Figure 2.2B, upper). The corresponding E_{FRET} trajectory shows a two-state fluctuation between a high E_{FRET} (~0.59) and a low E_{FRET} (~0.17) state, corresponding to the structural interconversions between conf-I and conf-II (Figure 2.2B, bottom). Past studies have shown that the two stochastic waiting times in the E_{FRET} trajectory, τ_I and τ_{II}, follow exponential distributions and the exponential decay constants are the interconversion rate constants.[28,29] Therefore, $\langle \tau_I \rangle^{-1}$, where $\langle\ \rangle$ denotes averaging and which represents the time-averaged single-molecule rate of conf-I $\rightarrow$ conf-II transition, equals k_1, the ensemble average rate constant for the conf-I $\rightarrow$ conf-II transition. The rate $\langle \tau_{II} \rangle^{-1}$, which represents the time-averaged single-molecule rate of conf-II $\rightarrow$ conf-I transition, equals k_{-1}, the ensemble average rate

constant for conf-II → conf-I transition (Supporting Information (SI), Section 2.8.2.1). For HJC2, the rate constants determined are $\langle \tau_I \rangle^{-1} = k_1 = 5.1 \pm 0.1\ s^{-1}$ and $\langle \tau_{II} \rangle^{-1} = k_{-1} = 0.85 \pm 0.02\ s^{-1}$.

2.2.2 Apo-CueR–HJC2 interaction dynamics

In the presence of CueR without Cu^{1+} bound, i.e., apo-CueR, significant perturbations are observed in the E_{FRET} trajectory of individual HJC2 molecules (Figure 2.3A), indicating that apo-CueR binding alters HJC2 structural dynamics. The E_{FRET} trajectory shows a shift towards the high E_{FRET} state, i.e., conf-I. This shift in structural equilibrium is clearer in the E_{FRET} histogram (Figures 2.3B, C), where the intensity of the peak corresponding to conf-I increases relative to that of conf-II. This equilibrium shift reports the preferential binding of apo-CueR to conf-I over conf-II.

The structural equilibrium shift of HJC2 caused by apo-CueR binding is accompanied by changes in the interconversion kinetics. The time-averaged single-molecule rate of conf-I → conf-II transition, $\langle \tau_I \rangle^{-1}$, depends on the apo-CueR concentration, [apo-CueR], decreasing asymptotically to zero with increasing [apo-CueR] (Figure 2.4A). This dependence indicates that apo-CueR binding slows down conf-I → conf-II structural transition, lengthening the lifetime of conf-I. In contrast, the time-averaged single-molecule rate of conf-II → conf-I transition, $\langle \tau_{II} \rangle^{-1}$, increases initially with increasing [apo-CueR], but decays at higher [apo-CueR] after reaching a maximum (Figure 2.4B). This biphasic behavior of $\langle \tau_{II} \rangle^{-1}$ indicates that the initial apo-CueR binding facilitates conf-II → conf-I transition while a higher-order apo-CueR interaction slows it down.

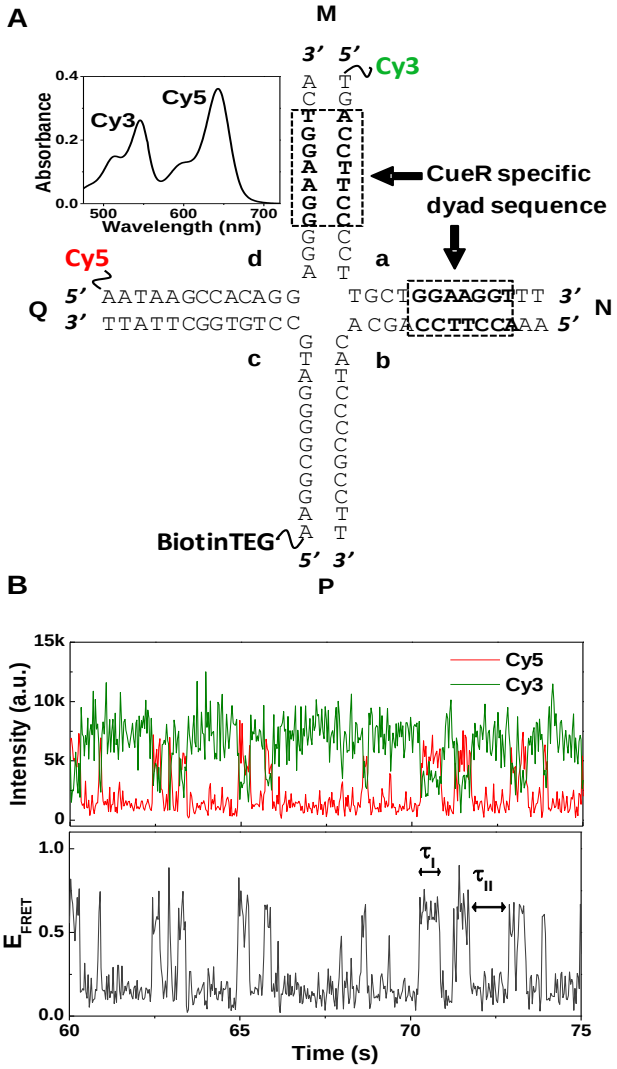

Figure 2.2 CueR-specific Holliday junction, HJC2. (A) Design of HJC2 with the dyad-symmetric sequence in arms *M* and *N*, Cy3 and Cy5 labels on strands a and d, and BiotinTEG on strand c. Inset: Absorption spectrum of the Cy3 and Cy5 labeled HJC2. (B) Exemplary single-molecule fluorescence (top) and E_{FRET} (bottom) trajectories of HJC2, showing two-state fluctuations. E_{FRET} is approximated as $I_{Cy5}/(I_{Cy3} + I_{Cy5})$ (I: fluorescence intensity). τ_I and τ_{II} are the waiting times on the E_{FRET} states of conf-I and conf-II, respectively. a.u. = arbitrary units.

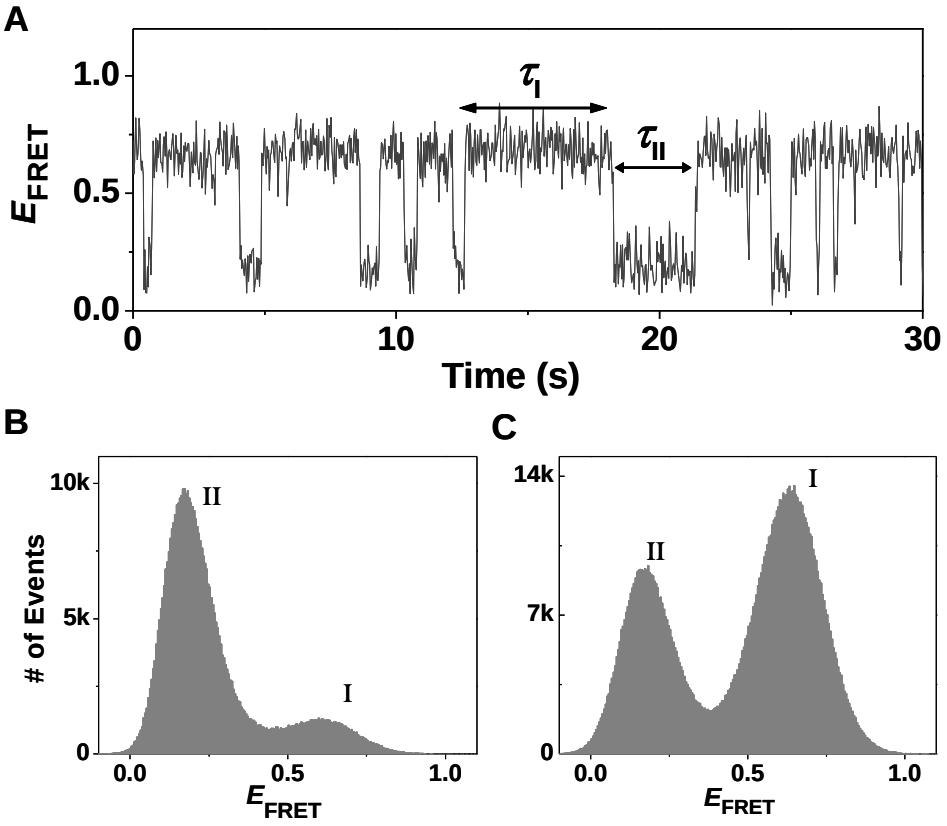

Figure 2.3 (A) Representative HJC2 E_{FRET} trajectory in the presence of 1.0 μM apo-CueR. (B, C) Histograms of HJC2 E_{FRET} trajectories in the absence (B) and presence (C) of 1.0 μM apo-CueR. Bin size: 0.005. Approximately 250 molecules were analyzed for each histogram.

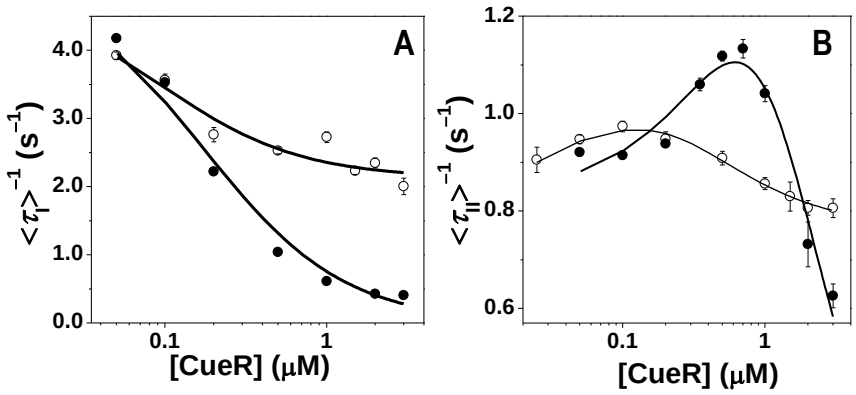

Figure 2.4 Apo-CueR (●) and holo-CueR (○) concentration dependence of $\langle \tau_I \rangle^{-1}$ (A) and $\langle \tau_{II} \rangle^{-1}$ (B). Each data point is an average of the waiting times from ~250 trajectories. The solid lines are the fits with Equation 1 (apo) and Equation 3 (holo) for (A) and Equation 2 (apo) and Equation 4 (holo) for (B). Results from the fit are summarized in Table 1.

The [apo-CueR] dependence of $\langle \tau_I \rangle^{-1}$ can be described by a simple kinetic mechanism in which apo-CueR (P) binds to conf-I to form a complex (P-I) that does not lead to structural transition to conf-II (Figure 2.5A, red box). Based on this kinetic scheme and following a single-molecule kinetic analysis (SI, Section B), it is derived that:

$$\langle \tau_I \rangle^{-1} = \frac{k_1}{1+[P]/K_{P\text{-}I}} \qquad \text{Equation 2.1}$$

Here $K_{P\text{-}I}$ (= k_{-2}/k_2) is the dissociation constant for the apo-CueR–conf-I complex, and k_2 and k_{-2} are the protein binding and unbinding rate constants to conf-I, respectively. Equation 2.1 predicts that with increasing protein concentration, $\langle \tau_I \rangle^{-1}$ decreases asymptotically to zero, consistent with the experimental results (Figure 2.4A). Using k_1 determined from the free HJC2 and fitting the data in Figure 2.4A gives $K_{P\text{-}I}$ = 0.17 ± 0.02 μM.

To account for the biphasic [apo-CueR] dependence of $\langle \tau_{II} \rangle^{-1}$, a two-step kinetic mechanism was considered: Apo-CueR initially binds to conf-II to form a complex (P-II) that can lead to structural transition to conf-I; this P-II complex can subsequently bind a second protein molecule to form a tertiary complex (P_2-II) that does not lead to structural transition to conf-I (Figure 2.5A, green box). Based on this two-step interaction scheme and following a single-molecule kinetic analysis:

$$\langle \tau_{II} \rangle^{-1} = \frac{k_{-1}+k_6[P]/K'_{P\text{-}II}}{1+[P]/K'_{P\text{-}II}+[P]^2/(K'_{P\text{-}II}K_{P_2\text{-}II})} \qquad \text{Equation 2.2}$$

Here $K'_{P\text{-}II} = (k_{-4} + k_6)/k_4$, $K_{P_2-II} = k_{-5}/k_5$, and k's are the rate constants defined in Figure 5A. Equation 2.2 predicts that at low protein concentrations, $\langle \tau_{II} \rangle^{-1}$ increases with increasing protein concentration because the formation of complex P-II facilitates the

structural transition to conf-I, and at higher protein concentrations, $\langle \tau_{II} \rangle^{-1}$ decreases because the formation of complex P_2-II slows down the transition to conf-I. Using k_{-1} determined from the free HJC2 and fitting the data in Figure 2.4B give: $k_6 = 4 \pm 3\ s^{-1}$, the rate constant for P-II $\rightarrow$ I transition; $K'_{P\text{-}II} = 3 \pm 3\ \mu M$, the apparent protein dissociation constant of complex P-II; and $K_{P_2\text{-}II} = 0.5 \pm 0.5\ \mu M$, the first dissociation constant of complex P_2-II. The determined k_6 is higher than k_{-1}, indicating that the initial binding of apo-CueR to conf-II facilitates its structural transition to conf-I. Table 1 summarizes all the fitting results.

2.2.3 Holo-CueR–HJC2 interaction dynamics

Holo-CueR, i.e., Cu^{1+}-bound CueR, causes perturbations on HJC2 structural dynamics similar to apo-CueR. With increasing [holo-CueR], $\langle \tau_I \rangle^{-1}$, the time-averaged conf-I $\rightarrow$ conf-II transition rate, decreases gradually (Figure 2.4A), and $\langle \tau_{II} \rangle^{-1}$, the time-averaged conf-II $\rightarrow$ conf-I transition rate, increases initially and then decays at higher [holo-CueR] (Figure 2.4B). However, significant differences also exist: neither $\langle \tau_I \rangle^{-1}$ nor $\langle \tau_{II} \rangle^{-1}$ decays to zero at high [holo-CueR], in contrast to those of apo-CueR–HJC2 interactions. The nonzero values of $\langle \tau_I \rangle^{-1}$ and $\langle \tau_{II} \rangle^{-1}$ at high [holo-CueR] indicate that the relevant holo-CueR–HJC2 complexes can still allow transitions from one conformer of HJC2 to the other.

To account for these differences observed for holo-CueR–HJC2 interactions, two kinetic transitions were added on top of the kinetic mechanism of apo-CueR–HJC2 interactions (Figure 2.5B). One transition connects P-I to II (i.e., k_3), and the other connects P_2-II to I (i.e., k_7). Based on this kinetic mechanism, the corresponding equations connecting $\langle \tau_I \rangle^{-1}$ and $\langle \tau_{II} \rangle^{-1}$ with the kinetic parameters and the protein concentration are (SI, Section C):

$$\langle \tau_{\mathrm{I}} \rangle^{-1} = \frac{k_1 + [\mathrm{P}]k_3 / K'_{\mathrm{P\text{-}I}}}{1 + [\mathrm{P}]/ K'_{\mathrm{P\text{-}I}}} \qquad \text{Equation 2.3}$$

$$\langle \tau_{\mathrm{II}} \rangle^{-1} = \frac{k_{-1} + [\mathrm{P}]\left(k_{-1}k_7 /(k_6 K'_{\mathrm{P_2\text{-}II}}) + k_6 / K'_{\mathrm{P\text{-}II}}\right) + [\mathrm{P}]^2 k_7 /(K'_{\mathrm{P\text{-}II}} K'_{\mathrm{P_2\text{-}II}})}{1 + [\mathrm{P}]\left(k_7 /(k_6 K'_{\mathrm{P_2\text{-}II}}) + 1/ K'_{\mathrm{P\text{-}II}}\right) + [\mathrm{P}]^2 /(K'_{\mathrm{P\text{-}II}} K'_{\mathrm{P_2\text{-}II}})} \quad \text{Equation 2.4}$$

where $K'_{\mathrm{P\text{-}I}} = (k_{-2} + k_3)/k_2$, $K'_{\mathrm{P\text{-}II}} = k_6/k_4$, and $K'_{\mathrm{P_2\text{-}II}} = (k_{-5} + k_7)/k_5$. The individual kinetic parameters are defined in Figure 5B. In deriving Equation 2.4, it was that assumed $k_{-4} = 0$ to obtain a clean analytical expression; this assumption does not affect the analyses of $\langle \tau_{\mathrm{I}} \rangle^{-1}$ (Equation 2.3), from which $K'_{\mathrm{P\text{-}I}}$ and k_3 can be obtained and interpreted quantitatively.

Equation 2.3 predicts that with increasing [holo-CueR], $\langle \tau_{\mathrm{I}} \rangle^{-1}$ decreases and eventually approaches k_3, the rate constant for the P-I $\rightarrow$ II transition, consistent with experimental observations (Figure 2.4A) and resulting from that high [holo-CueR] drives the conversion of I $\rightarrow$ P-I. Using k_1 determined from the free HJC2 and fitting the data in Figure 2.4A give $k_3 = 2.3 \pm 0.2$ s^{-1} and $K'_{\mathrm{P\text{-}I}} = 0.05 \pm 0.02$ μM, which is the apparent dissociation constant of P-I. The determined k_3 is smaller than k_1, consistent with the expectation that holo-CueR binding stabilizes conf-I and slow down its structural transition to conf-II.

Equation 2.4 predicts the observed [holo-CueR] dependence of $\langle \tau_{\mathrm{II}} \rangle^{-1}$, with an initial rise followed by a decay. At high [holo-CueR], $\langle \tau_{\mathrm{II}} \rangle^{-1}$ approaches k_7, the rate constant of the P_2-II $\rightarrow$ I transition, as high [holo-CueR] drives the formation of P_2-II. Using k_{-1} determined from the free HJC2 and fitting the data in Figure 4B give $k_7 = 0.77 \pm 0.02$ s^{-1}, $K'_{\mathrm{P\text{-}II}} = 0.1 \pm 0.1$ μM, which is the apparent dissociation constant of complex P-II, and $K'_{\mathrm{P_2\text{-}II}} = 0.2 \pm 0.2$ μM, which is the apparent first protein dissociation constant of P_2-II. The kinetic parameters are summarized in Table 1.

To confirm that the interactions between CueR and HJC2 are specific, i.e. due

to the encoded specific dyad-symmetric sequence in HJC2, the structural dynamics of HJC2 was studied in the presence of another DNA-binding protein, PbrR691, which is also a MerR-family metalloregulator; no noticeable perturbation was observed (Figure S1). Additionally, another HJ that does not contain CueR-targeting sequence was studied; as expected, in the presence of CueR, no noticeable perturbation on this HJ's structural dynamics was observed.[28]

2.2.4 CueR-imposed HJ structural changes

The single-molecule kinetic analyses on the structure dynamics of HJC2 indicate that both apo- and holo-CueR can bind to the two conformers of HJC2 to form complexes P-I, P-II, and P_2-II (Figure 2.5). The changes in the E_{FRET} values of conf-I and conf-II in these complexes relative to those of free HJC2 can inform of the structural changes of HJC2 imposed by the CueR. For interactions with conf-I, at high [apo-CueR] (e.g., 2 μM) where I is converted to P-I, $E_{conf\text{-}I}$ increases from ~0.59 to ~0.64 (Figures 2.6A, B). This increase of $E_{conf\text{-}I}$ indicates that in the P-I complex, apo-CueR causes a shortening of the distance between the ends of arms *M* and *Q* where Cy3 and Cy5 are located (reference Figure 1.1, left). This protein-induced structural change of conf-I also confirms the binding of apo-CueR. Similarly, holo-CueR binding also increases $E_{conf\text{-}I}$ (Figure 2.6C), indicating a similarly shortened distance between the ends of arms *M* and *Q* in conf-I.

To determine structural changes of conf-II upon CueR binding, an alternatively labeled HJC2, referred to as HJC2a, which has the Cy5 placed at the end of arm *N* instead of arm *Q* was studied (reference Figure 2.1). This alternative labeling makes conf-II of HJC2a the high E_{FRET} state, rendering its E_{FRET} value ($E_{conf\text{-}II}$) more sensitive to structural changes imposed by protein binding. At low [apo-CueR] (e.g., 0.3 μM), where the complex P-II dominates the population of all forms of conf-II, no significant decrease in $E_{conf\text{-}II}$ is observed compared to that of free HJC2a (Figures 2.6D, E). At

high [apo-CueR] (e.g., 3 μM), where P_2-II dominates, $E_{conf\text{-}II}$ increases significantly (Figure 2.6F). This clear increase indicates that in the P_2-II complex, where two apo-CueR molecules are bound, the arms *M* and *N* are brought closer to each other. These protein-induced structural changes of conf-II also confirm the binding of apo-CueR. For holo-CueR and conf-II interactions, in contrast, no significant changes of $E_{conf\text{-}II}$ were observed.

Table 2.1 Kinetic parameters for CueR–HJC2 interaction dynamics

	Free HJC2	
k_1	$5.1 \pm 0.1\ s^{-1}$	
k_{-1}	$0.85 \pm 0.02\ s^{-1}$	
	apo-CueR	**Holo-CueR**
k_3	-	$2.3 \pm 0.2\ s^{-1}$
k_6	$4 \pm 3\ s^{-1}$	$1.2 \pm 0.3\ s^{-1}$
k_7	-	$0.77 \pm 0.02\ s^{-1}$
$(k_{-2} + k_3)/k_2$	0.17 ± 0.02 μM ($K_{P\text{-}I}$) [a]	0.05 ± 0.02 μM ($K'_{P\text{-}I}$)
$(k_{-4} + k_6)/k_4$	3 ± 3 μM ($K'_{P\text{-}II}$)	0.1 ± 0.1 μM ($K'_{P\text{-}II}$) [c]
$(k_{-5} + k_7)/k_5$	0.5 ± 0.5 μM ($K_{P_2\text{-}II}$) [b]	0.2 ± 0.2 μM ($K'_{P_2\text{-}II}$)

[a] $k_3 = 0$ (apo-CueR) [b] $k_7 = 0$ (apo-CueR) [c] k_{-4} is set to zero (holoCueR, SI-C).

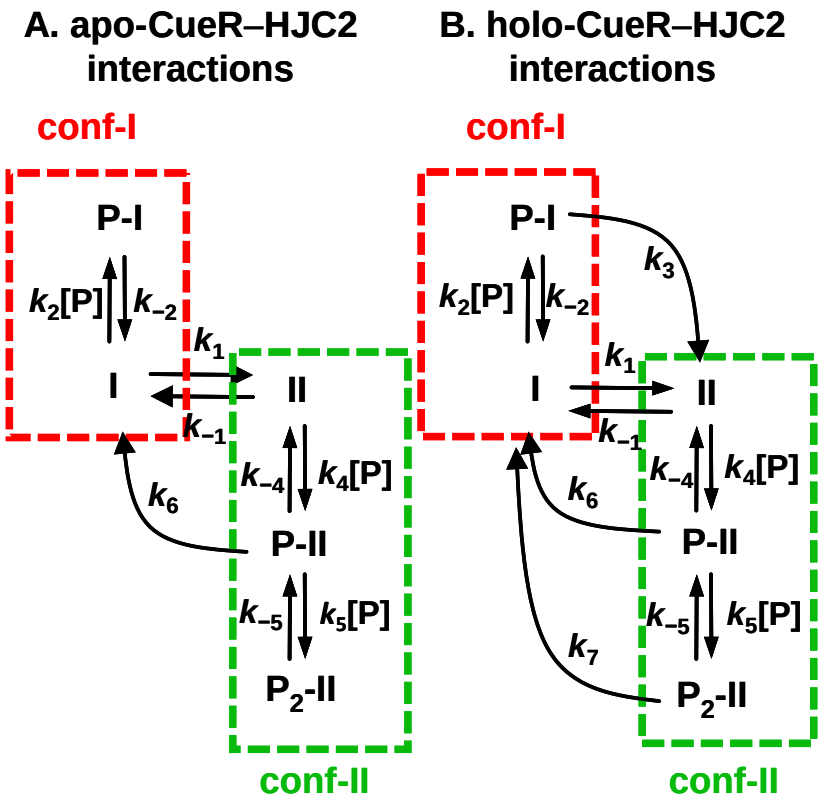

Figure 2.5 Kinetic schemes for HJC2 interactions with apo-CueR (A) and holo-CueR (B). I, conf-I; II, conf-II; P, apo-CueR or holo-CueR; and *k*'s, rate constants.

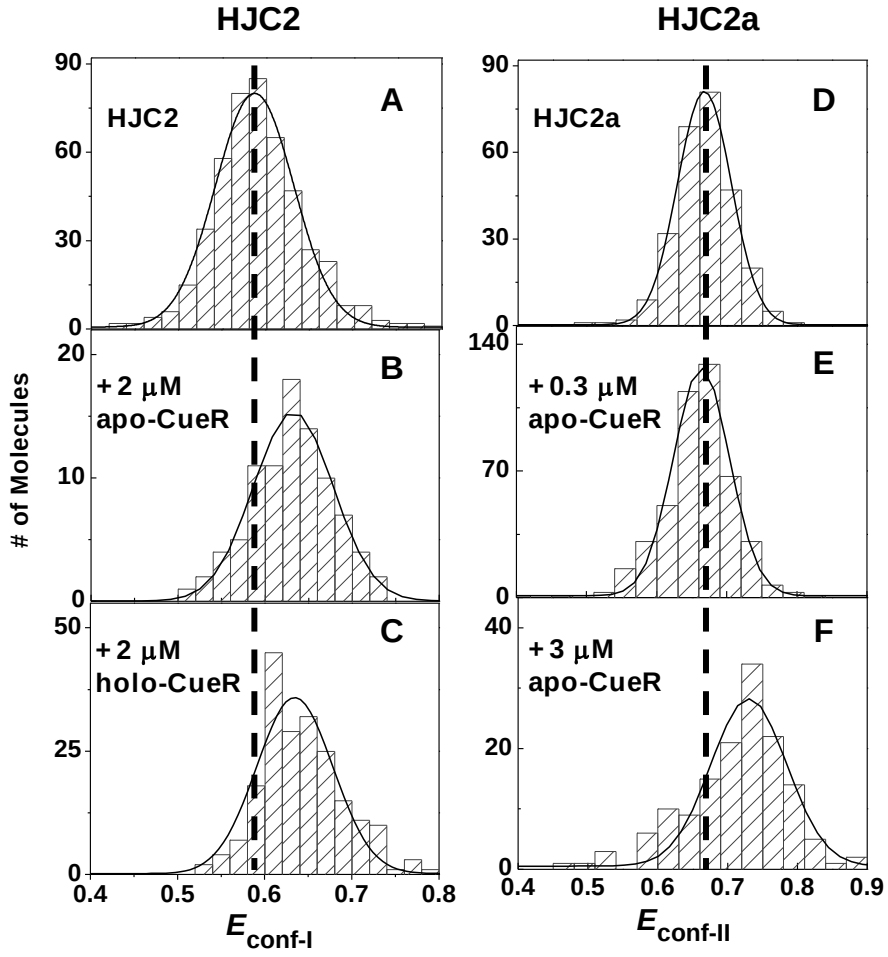

Figure 2.6 Histograms of E_{conf-I} of HJC2 (A, B, C) and $E_{conf-II}$ of HJC2a (D, E, F) in the presence of various apo-CueR and holo-CueR concentrations. Solid lines are Gaussian fits centered at 0.59 ± 0.01 (A), 0.64 ± 0.01 (B), 0.63 ± 0.01 (C), 0.67 ± 0.01 (D), 0.66 ± 0.01 (E), and 0.73 ± 0.01 (F). For each molecule, its E_{conf-I} or $E_{conf-II}$ was obtained by fitting the histogram of its E_{FRET} trajectory with two Gaussian functions. Histograms at another protein concentration are given in Figure S4.

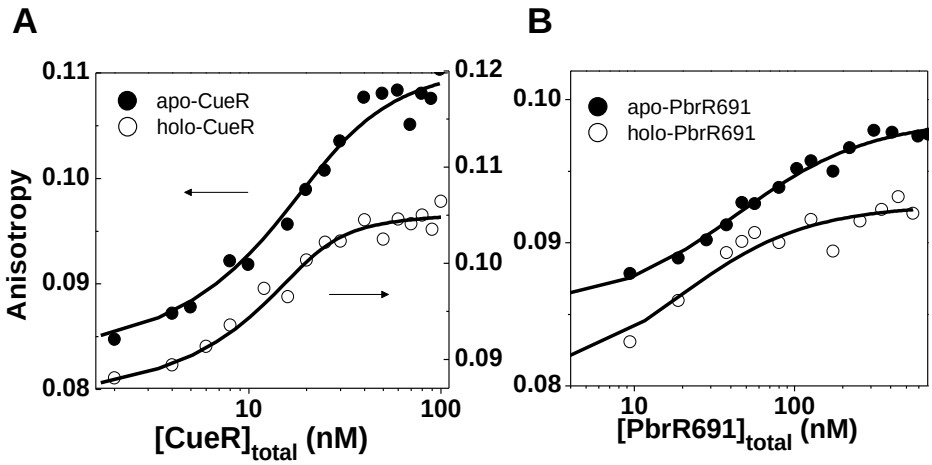

Figure 2.7 Fluorescence anisotropy titrations of CueR (A) and PbrR691 (B) binding to Cy3-labeled double-strand DNA. Solid lines are the fits with Equation 2.5, with dissociation constants of K_D(apo-CueR) = 9 ± 2 nM, K_D(holo-CueR) = 1.6 ± 0.8 nM, K_D(apo-PbrR691) = 43 ± 9 nM, and K_D(holo-PbrR691) = 23 ± 9 nM. The x-axes are total protein concentrations. Plots with x-axes being the free protein concentration are given in Figure S5 (Anisotropy for PbrR691 was done by Qi Wang, Cornell University).

2.2.5 Ensemble CueR–DNA affinity determination

For the apo-CueR interaction with conf-I of HJC2, the dissociation constant $K_{P\text{-}I}$ (= k_{-2}/k_2) directly reflects the binding affinity of apo-CueR to conf-I (Equation 2.1). For holo-CueR, only the apparent dissociation constant $K'_{P\text{-}I}$ (= $(k_{-2} + k_3)/k_2$) can be obtained by analyzing the waiting times (Equation 2.3), and it gives an upper limit for the dissociation constant of holo-CueR–conf-I interactions, since $(k_{-2} + k_3)/k_2 > k_{-2}/k_2$. The binding affinity to conf-I is important, as conf-I has its arms *M* and *N*, which contain the dyad-symmetric sequence, coaxially stacked as in a B-form DNA.[32,33] Experimentally, $K_{P\text{-}I}$ (= 0.17 ± 0.02 μM) for apo-CueR is larger than $K'_{P\text{-}I}$ (= 0.05 ± 0.02 μM) for holo-CueR (Table 1), indicating that apo-CueR binds more weakly to conf-I than does holo-CueR.

On the other hand, previous results from the gel-shift assays suggested a slightly stronger binding affinity for apo-CueR than for holo-CueR to a double-strand DNA containing the promoter sequence, with the dissociation constants K_D(apo-CueR) = 17 ± 2 nM and K_D(holo-CueR) = 25 ± 7 nM,[36] although the error bars of these values preclude a reliable comparison. To test if there is indeed a discrepancy that could come from the DNA used (i.e., using engineered HJ versus using a double-strand DNA), the binding affinity of both apo- and holo-CueR to a double-strand DNA was determined using ensemble fluorescence anisotropy titration, a more accurate quantitation method than the gel-shift assay. A Cy3-labeled 25-basepair double-strand DNA with the same sequence as that spanning the *M, N* arms of HJC2 was used. The results in Figure 2.7A confirm that apo-CueR does bind more weakly to DNA than does holo-CueR, with K_D(apo-CueR) = 6 ± 2 nM and K_D(holo-CueR) = 1.9 ± 0.8 nM, consistent with the results using the engineered HJC2 as a single-molecule reporter. The affinities of apo- and holo-CueR to conf-I of HJC2 are weaker than to the double-strand DNA, possibly due to the presence of the other helix or the perturbation of the

junction structure of HJC2 on the protein–DNA interactions.

2.3 Discussion

2.3.1 Nature of CueR–HJC2 interactions and relation to protein function

The single-molecule studies of CueR–HJC2 interactions indicate that both apo- and holo-CueR preferentially bind and stabilize conf-I of HJC2. This preferential interaction is directly reflected by HJC2's structural equilibrium shift toward conf-I (Figures 2.3B, C), as well as the decrease of $\langle \tau_I \rangle^{-1}$ with increasing protein concentration due to the formation of the P-I complex (Figures 2.4A and 2.5). The preferential interaction with conf-I is also reflected by the protein concentration dependence of $\langle \tau_{II} \rangle^{-1}$, which shows that the P-II complex can induce structural transition from conf-II to conf-I with a larger rate constant (k_6) than that (k_{-1}) of the intrinsic II $\rightarrow$ I transition (Table 2.1 and Figure 2.5). All these observations are consistent with CueR's normal function as a double-strand DNA-binding protein, as conf-I mimics the natural substrate of CueR and has its arms *M* and *N*, which encodes the dyad-symmetric sequence, coaxially stacked to form a B-form DNA-like structure (Figure 2.1, left).[32,33]

Both apo- and holo-CueR binding to conf-I bring the arms *M* and *Q* closer, reflected by the increase of $E_{\text{conf-I}}$ of HJC2 (Figures 2.6B, C). This structural change could be associated with the bending of the *M*–*N* helix of conf-I, as observed in the previous study of PbrR691 [28] and typical among MerR-family metalloregulators.[5,23,24] For conf-II, no significant structural change is observed upon initial binding of one apo-CueR or holo-CueR molecule.

A distinct feature of CueR–HJC2 interactions is the initial-rise-followed-by-

decay of $\langle \tau_{II} \rangle^{-1}$ with increasing protein concentrations (Figure 2.4B). This biphasic protein concentration dependence of $\langle \tau_{II} \rangle^{-1}$ indicates that at high protein concentrations, both apo- and holo-CueR interact with conf-II to form the P_2-II complex, in which two protein molecules are bound (Figure 2.5). This tertiary complex was not observed in the study of PbrR691,[28] suggesting that differences exist among MerR-family metalloregulators in their interactions with DNA. The formation of this tertiary complex could be related to the highly bent orientation of the two halves of the dyad-symmetric sequence in conf-II, which largely deviates from the structure of a B-form DNA (Figure 2.1, right). Consequently, only half of the dyad sequence could be bound to one of the two DNA-binding domains of CueR, leaving the other half to bind another CueR molecule. The double binding of apo-CueR then leads to the *M* and *N* arms being pushed closer in conf-II, reflected by the increase in $E_{\text{conf-II}}$ of HJC2a (Figure 2.6F). Double binding of holo-CueR, however, does not result in observable changes in $E_{\text{conf-II}}$, indicating that apo- and holo-CueR interact differently with DNA.

To support the model that CueR binds to half of the dyad-symmetric sequence, a Cy3-labeled double-strand DNA that encodes only half of the CueR-specific dyad-symmetric sequence was constructed. Fluorescence anisotropy titration was then used to probe CueR binding. The results (Figure S4) show that apo-CueR can indeed bind to this DNA with a K_D of ~0.7 μM, which is in the concentration range where the P_2-II complex forms (Figure 2.4B).

Further differences exist between apo-CueR and holo-CueR. Unlike apo-CueR, holo-CueR binding can still allow P-I → II and P_2-II → I transitions (k_3 and k_7, Figure 2.5B). As conf-I and conf-II are largely different in their spatial arrangements of the dyad-symmetric sequence (Figure 2.1), being more accommodating in allowing HJC2 structural interconversion suggests that holo-CueR has a more flexible conformation

than does apo-CueR. This conformational flexibility of holo-CueR could play important roles in its interaction with the RNA polymerase (RNAp) for transcription, given that past studies on MerR, the prototype MerR-family metalloregulator, showed that the holo-MerR–DNA–RNAp tertiary complex undergoes structural rearrangements in transcription initiation.[5,17,18,39]

2.3.2 Implications for transcriptional suppression after activation

The single-molecule studies and the ensemble fluorescence anisotropy titration both indicate that holo-CueR binds more strongly to DNA than does apo-CueR. The stronger DNA binding of the holo-protein is also observed for PbrR691 from fluorescence anisotropy titrations (Figure 2.7B), with the dissociation constants of K_D(apo-PbrR691) = 43 ± 9 nM and K_D(holo-PbrR691) = 23 ± 9 nM. Furthermore, BmrR, another MerR-family regulator that responds to organic effectors, also has a higher affinity to its substrate in its holo-form compared to its apo-form.[40]

This stronger DNA binding by the holo-protein is surprising, however, given that past studies on MerR have shown that the holo-protein binds more weakly to DNA than does the apo-protein (K_D(apo-MerR) = 0.14 ± 0.04 nM, K_D(holo-MerR) = 0.42 ± 0.07 nM).[17] As the direct dissociation of the metal ion from the metalloregulator is believed to be difficult due to strong metal coordination, it was thought that the weaker binding of holo-protein would facilitate its replacement from the DNA by the apo-protein, thus switching off the transcription after transcriptional activation and once the cell is relieved of the metal stress. Therefore, the opposite relative DNA binding affinity of apo-protein versus holo-protein for CueR (as well as PbrR691 and BmrR) suggests possible differences in the mechanism by which MerR-family regulators switch off transcription.

Moreover, unlike MerR, which might involve another protein MerD to help the dissociation of the holo-MerR–DNA complex, no evidence has so far been found for a

co-regulator role of a MerD homologue in the regulatory mechanism of CueR.[16] For CueR to switch off transcription after activation, one simple scenario is a direct dissociation of holo-CueR from DNA followed by binding of apo-CueR, which would be the dominant form of CueR inside the cell after activation of Cu-resistance genes. For this scenario to be viable, the dissociation kinetics of holo-CueR from DNA has to be in a relevant timescale to gene regulation. From single-molecule kinetic analyses, the rate constants for CueR unbinding (k_{-2}) and binding (k_2) to conf-I of HJC2 cannot be obtained. Nevertheless, as the CueR binding and unbinding are contained in the observed structural dynamics of HJC2, which was measured experimentally, it can be concluded that CueR binding and unbinding should occur at a comparable timescale to HJC2's structural dynamics, i.e., hundreds of milliseconds to seconds, a relevant timescale for gene expression regulation.

2.4 Summary

Using the engineered HJC2 as a single-molecule protein–DNA interaction reporter, I have studied how CueR, a Cu^{1+}-responsive MerR-family metalloregulator, interacts with DNA. Both apo- and holo-CueR preferentially bind conf-I of HJC2, in which the protein-recognition sequence is arranged similarly to B-form DNA. This preferential binding stabilizes conf-I and slows down its structural conversion to conf-II. Both protein forms also bend the *M*–*N* helix of conf-I, reflecting the protein-induced DNA structural changes for transcriptional regulation. In their interactions with conf-II of HJC2, apo- and holo-CueR exhibit a biphasic behavior — at low protein concentrations, a 1:1 protein–conf-II complex is present, whereas at high protein concentrations a 2:1 protein–conf-II tertiary complex dominates. Many differences also exist between apo- and holo-CueR in their interactions with HJC2. While apo-CueR causes clear structural changes of both conf-I and conf-II of HJC2,

holo-CueR only causes measurable structural changes of conf-I. Holo-CueR is more accommodating to structural interconversions of HJ, suggesting that it has a comparatively more flexible conformation, which could be important for its cooperation with RNAp in initiating transcription. Moreover, holo-CueR binds more strongly to DNA than apo-CueR, a surprising finding and contrary to the behaviors of the prototype metalloregulator MerR. This contrast suggests functional differences among MerR-family regulators, in particular possible different mechanisms in switching off transcription after activation. This study demonstrates the general applicability of engineered HJs as single-molecule reporters for protein–DNA interactions, which are fundamental in gene replication, transcription, recombination, and regulation.

2.5 Materials and Methods

2.5.1 Expression and purification of CueR

E. coli CueR protein was expressed and purified as previously described.[34] Briefly, CueR was cloned in an expression vector pET30a, transformed and expressed in *E. coli* BL21(DE3). The cells were grown until the OD_{600} was 0.6 before IPTG (1 mM) was added. After an additional 4-hour growth at 37°C, cells were harvested by centrifugation and then disrupted by French press in lysis buffer (10 mM Tris, 300 mM NaCl, 10 mM BME, 10% glycerol at pH 7.3). The cell debris was removed by centrifugation and the protein in the supernatant was purified first by precipitating with 45% $(NH_4)_2SO_4$ and then by gel filtration in a Sephadex G-25 column. The collected fractions were further purified through a Heparin affinity column (16/10 Heparin FF, GE Healthcare) and a gel filtration column (HILOAD 26/60 Superdex 200 PR, GE Healthcare). Purified CueR was checked by SDS-PAGE, confirmed by ESI-MS, and quantified via BCA assay (Pierce). Purified protein was stored at –80^{o}C

in 50 mM pH 8.0 Tris Buffer, with 250 mM NaCl, 5 mM BME, and 20% glycerol. The as-purified CueR was shown to be in its apo-form via a BCA copper quantitation assay.[41]

2.5.2 HJ preparation and purification

CueR-specific HJC2 was designed and purified as described previously.[28] The four DNA strands (Figure 2A) were purchased from Integrated DNA Technologies, and dissolved in 10 mM Tris buffer pH 7.3 with 100 mM NaCl. HJC2 was assembled by annealing strands **a**, **b**, and **c** first at 50°C; after slow cooling to 37°C, strand **d** was added. The solution was then incubated for 30 min at 37°C before cooling down to room temperature. The annealed HJC2 was purified by electrophoresis in 20% polyacrylamide gel.

2.5.3 Single-molecule fluorescence experiments and data analysis

A prism-type total internal reflection (TIR) microscope based on an Olympus IX71 inverted microscope was used for single-molecule fluorescence measurements. The Cy3 probe on HJC2 was directly excited by a continuous wave circularly polarized 532 nm laser (CrystaLaser, GCL-025-L-0.5%) of ~6 mW focused onto an area of ~150 × 75 mm^2 on the sample. The fluorescence of both Cy3 and Cy5 was collected by a 60X NA 1.2 water-immersion objective (UPLSAPO60XW, Olympus), with an extra 1.6X magnification, and split by a dichroic mirror (635DCXR) into two channels using a Dual-View system (Optical Insights, Inc.). An HQ550LP filter was used to reject the excitation laser light and each channel of fluorescence was further filtered (HQ580-60m or HQ660LP) and projected onto half of the imaging area of a camera (Andor Ixon EMCCD, DV887DCS-BV), controlled by the Andor IQ software. The time resolution for all the single-molecule experiments is 30 ms. A custom IDL program was used to extract individual fluorescence trajectories of Cy3 and Cy5 for

each HJC2 from a movie.

Single-molecule experiments were carried out using a flow cell, formed by double-sided tapes sandwiched between a quartz slide (Technical Glass) and a borosilicate coverslip (Gold Seal). All samples were in 10 mM Tris buffer, pH 7.3 with 10 mM NaCl and 2 mM $MgCl_2$. To minimize nonspecific protein adsorption on glass surfaces, quartz slides were first amine functionalized (Vectabond, Vector Laboratories) and then coated with PEG polymers (100 mg/mL m-PEG-SPA-5000, Sunbio, Inc. and 1 mg/mL biotin-PEG-NHS-3400, JenKem Technology USA).[26] 1% of the PEG polymers contain a biotin terminal group to form biotin-streptavidin (Molecular Probes) linkages for immobilizing biotinylated HJC2 molecules. Oxygen scavenging system (0.1 mg/mL glucose oxidase (Sigma), 0.025 mg/mL catalase (Roche), and 4% glucose (Aldrich)) and 1 mM Trolox (Sigma) were added into the sample solution just before each experiment to prolong the lifetime and suppress the blinking of the fluorescence probes.[42]

E_{FRET} trajectories were obtained from Cy3 and Cy5 intensity trajectories as $E_{FRET} = I_{Cy5}/(I_{Cy3} + I_{Cy5})$. Data in which photobleaching or blinking of either dye was apparent were removed before performing threshold analysis on each trajectory based on the distribution of the E_{FRET} values to obtain individual waiting times.[29] The average waiting time was then calculated from all trajectories obtained at a given protein concentration using the standard error of the mean as the error bar.

2.5.4 Fluorescence anisotropy

Fluorescence of Cy3 labeled double-strand DNA was measured using a Cary Eclipse fluorescence spectrophotometer (Varian). The CueR titration was in 10 mM Tris buffer with 10 mM NaCl and 2 mM $MgCl_2$ at pH 7.3, and PbrR691 titration in 10 mM Tris buffer with 100 mM $NaNO_3$ at pH 7.2. The sequence of the double-stand DNA for PbrR691 titration is 5'-TGACTCTATATCTACTAGAGGTT-3', where the

PbrR691-specific dyad-symmetric sequence is underlined. Fluorescence was excited at 532 nm. Anisotropy (r) was calculated as $r = (I_{//} - G*I_{\perp})/(I_{//} + 2*G*I_{\perp})$, where $I_{//}$ and $I_{\perp}$ are the fluorescence intensity parallel and perpendicular to the excitation polarization, respectively, and G is the correction factor for the instrument's different responses to light of parallel and vertical polarizations. The fluorescence anisotropy titration curves were fitted with the following equation:[43]

$$r = r_D + (r_{PD} - r_D)\frac{[D]_T + [P]_T + K_D - \sqrt{([D]_T + [P]_T + K_D)^2 - 4[P]_T[D]_T}}{2[D]_T} \quad \text{Equation 2.5}$$

where r_D and r_{PD} are the anisotropy values for free and protein-bound DNA, respectively, $[D]_T$ is the total DNA concentration, $[P]_T$ is the total protein concentration, and K_D is the dissociation constant of the protein-DNA complex.

2.6 Supporting Information

2.6.1 Supporting Figures

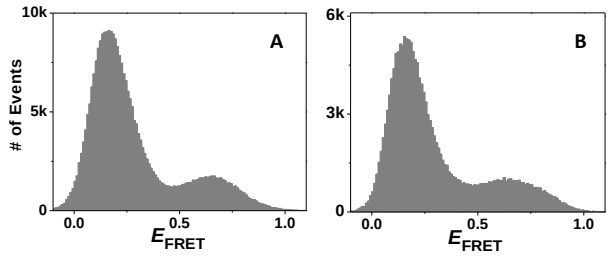

Figure S1 Histograms of HJC2 E_{FRET} trajectories in the absence (A) and presence of 1.0 μM apo-PbrR691 (B). Bin size: 0.01. Each histogram is compiled from more than 100 trajectories

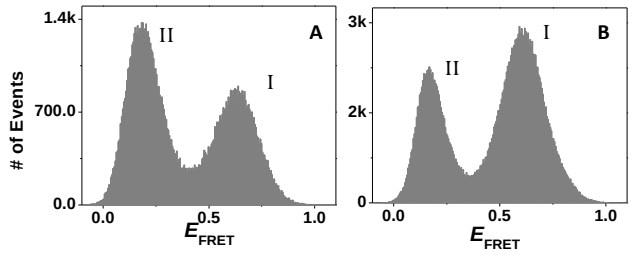

Figure S2 Histograms of HJC2 E_{FRET} trajectories in the presence of 0.5 μM apo-CueR (A) and 3 μM apo-CueR (B). Bin size: 0.005.

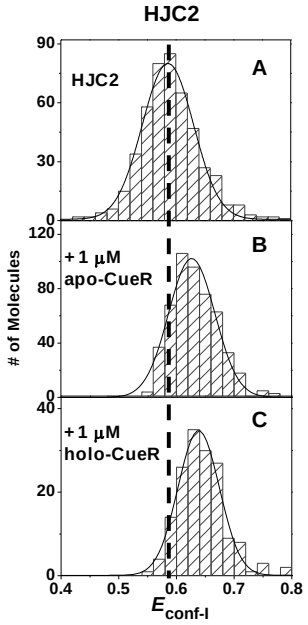

Figure S3 Histograms of E_{conf-I} of HJC2 (A) in the presence of 1 μM apo-CueR (B) and 1 μM holo-CueR (C). Solid lines are Gaussian fits centered at 0.59 ± 0.01 (A), 0.63 ± 0.01 (B), and 0.64 ± 0.01 (C).

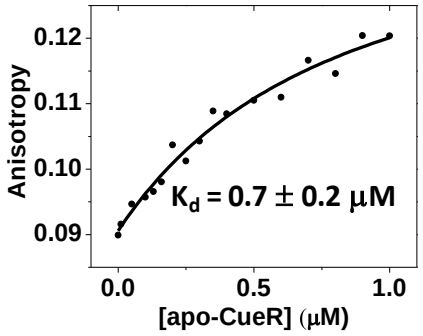

Figure S4 Fluorescence anisotropy experiment on Cy-3 labeled double-strand DNA containing only half of the dyad-symmetric sequence (5'-TGACCTTCCCCTTGCTTGGCTTGTT-3', the half sequence is underlined) titrated with apo-CueR. The solid line is the fit using Equation 5 which gave a K_D ~ 0.7 μM.

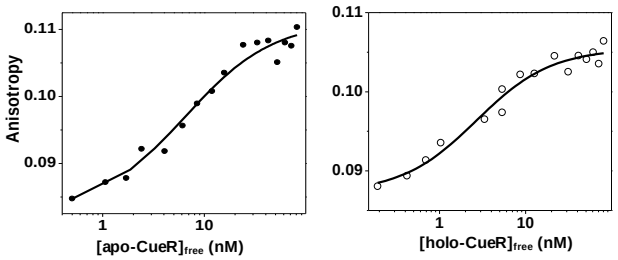

Figure S5 Data from Fig. 7 plotted against free protein concentrations.

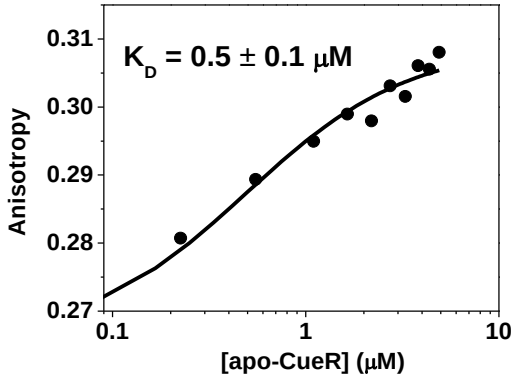

Figure S6 Fluorescence anisotropy experiment on Cy3-labeled HJC2 titrated with apo-CueR. The solid line is the fit using Equation 5 giving a $K_D \sim 0.5$ μM which is in between the affinity of apo-CueR to conf-I and to conf-II of HJC2 determined from single-molecule measurements.[b]

[b] Ensemble fluorescence anisotropy data obtained by Debashis Panda.

2.6.2 Derivation of single-molecule kinetics for HJC2 structural dynamics

2.6.2.1 Free HJC2

The structural dynamics of a HJ, if measured at the single-molecule level at tens of milliseconds time resolution, follows a two-state kinetic model effectively:

$$\mathrm{I} \underset{k_{-1}}{\overset{k_1}{\rightleftharpoons}} \mathrm{II}$$

where I denotes conf-I and II denotes conf-II (see also Figure 1 in the main text). The waiting time τ_{I} in the E_{FRET} trajectories is the time needed to complete I $\rightarrow$ II transition; the waiting time τ_{II} is the time required to complete the II $\rightarrow$ I transition; both are simple one-step kinetic reactions. The probability density functions for τ_{I} and τ_{II}, $f_{\mathrm{I}}(\tau)$ and $f_{\mathrm{II}}(\tau)$, are both single-exponential functions, with $f_{\mathrm{I}}(\tau) = k_1\exp(-k_1\tau)$ and $f_{\mathrm{II}}(\tau) = k_{-1}\exp(-k_{-1}\tau)$. The inverse of the average waiting times, $\langle\tau_{\mathrm{I}}\rangle^{-1}$ and $\langle\tau_{\mathrm{II}}\rangle^{-1}$, which represent the time-averaged single-molecule rates of I $\rightarrow$ II and II $\rightarrow$ I transitions respectively, are:

$$\langle\tau_{\mathrm{I}}\rangle^{-1} = \frac{1}{\int_0^\infty \tau\ f_{\mathrm{I}}(\tau)\mathrm{d}\tau} = k_1 \qquad \text{A1}$$

$$\langle\tau_{\mathrm{II}}\rangle^{-1} = \frac{1}{\int_0^\infty \tau\ f_{\mathrm{II}}(\tau)\mathrm{d}\tau} = k_{-1} \qquad \text{A2}$$

2.6.2.2 Apo-CueR and HJC2 interactions

The kinetic mechanism of apo-CueR interactions with HJC2 is shown in Figure 5A. The kinetic processes happening during τ_{I} are the following kinetic steps:

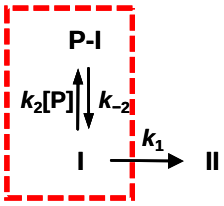

Figure S7 Kinetic scheme for apo-CueR interactions with conf-I of HJC2.

The corresponding single-molecule rate equations are:

$$\mathrm{d}P_{\mathrm{II}}(t)/\mathrm{d}t = k_1 P_{\mathrm{I}}(t) \qquad \text{B1}$$

$$\mathrm{d}P_{\mathrm{I}}(t)/\mathrm{d}t = -(k_1 + k_2[\mathrm{P}])P_{\mathrm{I}}(t) + k_{-2}P_{\mathrm{P\text{-}I}}(t) \qquad \text{B2}$$

$$\mathrm{d}P_{\mathrm{P\text{-}I}}(t)/\mathrm{d}t = k_2[\mathrm{P}]P_{\mathrm{I}}(t) - k_{-2}P_{\mathrm{P\text{-}I}}(t) \qquad \text{B3}$$

where $P(t)$'s are the probabilities of finding HJC2 in the corresponding states at time t and k's are the rate constants for the transitions. At the on-set of each τ_{I}, i.e., right after a II $\rightarrow$ I transition, the first state that HJC2 reaches is I; so the initial conditions for solving the above differential equations are: $P_{\mathrm{I}}(0) = 1$, $P_{\mathrm{II}}(0) = 0$, $P_{\mathrm{P\text{-}I}}(0) = 0$, where $t = 0$ is defined as the on-set of each τ_{I}. At any time, $P_{\mathrm{I}}(t) + P_{\mathrm{II}}(t) + P_{\mathrm{P\text{-}I}}(t) = 1$.

The probability density function of τ_{I}, $f_{\mathrm{I}}(\tau)$, can be evaluated. The probability of finding a particular τ is $f_{\mathrm{I}}(\tau)\Delta\tau$, which is equal to the probability for HJC2 to switch from I to II between τ and $\tau + \Delta\tau$, $\Delta P_{II}(\tau)$.[45,46] Therefore, $f_{\mathrm{I}}(\tau)\Delta\tau = \Delta P_{II}(\tau)$. In the limit of infinitesimal $\Delta\tau$, $f_{\mathrm{I}}(\tau)$ is equal to $dP_{II}(\tau)/d\tau$. Solving for $P_{II}(\tau)$ using equations B1-B3 by Laplace transform, the probability density function of τ_{I} is:

$$f_{\mathrm{I}}(\tau) = \frac{k_1 e^{(\alpha+\beta)\tau}}{2\alpha}\left[\alpha(1+e^{-2\alpha\tau}) + (\beta + k_{-2})(1-e^{-2\alpha\tau})\right]$$

where $\alpha = -\sqrt{\frac{1}{4}(k_1 + k_{-2} + k_2[\mathrm{P}])^2 - k_1 k_{-2}}$ and $\beta = -\frac{(k_1 + k_{-2} + k_2[\mathrm{P}])}{2}$.

Then:

$$\langle \tau_{\mathrm{I}} \rangle^{-1} = 1/\int_0^\infty \tau f_{\mathrm{I}}(\tau)\mathrm{d}\tau = \frac{k_1}{1+[P]/K_{P-I}}$$

where $\mathrm{K_{P-I}} = \mathrm{k_{-2}}/\mathrm{k_2}$ is the dissociation constant for the apo-CueR–conf-I complex. This equation is given as Equation 1 in the main text.

The kinetic processes happening during τ_{II} are the following kinetic steps:

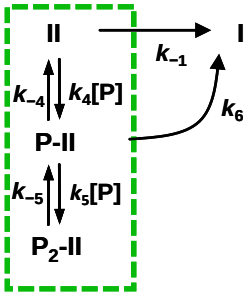

Figure S8 Kinetic scheme for interactions of apo-CueR with HJC2's conf-II.

The corresponding single-molecule rate equations are:

$$\mathrm{d}P_{\mathrm{I}}(t)/\mathrm{d}t = k_{-1}P_{\mathrm{II}}(t) + k_6 P_{\mathrm{P\text{-}II}}(t) \qquad \text{B4}$$

$$\mathrm{d}P_{\mathrm{II}}(t)/\mathrm{d}t = -(k_{-1} + k_4[\mathrm{P}])P_{\mathrm{II}}(t) + k_{-4}P_{\mathrm{P\text{-}II}}(t) \qquad \text{B5}$$

$$\mathrm{d}P_{\mathrm{P\text{-}II}}(t)/\mathrm{d}t = k_4[\mathrm{P}]P_{\mathrm{II}}(t) - (k_{-4} + k_6 + k_5[\mathrm{P}])P_{\mathrm{P\text{-}II}}(t) + k_{-5}P_{\mathrm{P_2\text{-}II}}(t) \qquad \text{B6}$$

$$\mathrm{d}P_{\mathrm{P_2\text{-}II}}(t)/\mathrm{d}t = k_5[\mathrm{P}]P_{\mathrm{P\text{-}II}}(t) - k_{-5}P_{\mathrm{P_2\text{-}II}}(t) \qquad \text{B7}$$

The initial conditions for solving above equations are: $P_{\mathrm{II}}(0) = 1$, $P_{\mathrm{I}}(0) = 0$, $P_{\mathrm{P\text{-}II}}(0) = 0$, and $P_{\mathrm{P_2\text{-}II}}(0) = 0$. At any time, $P_{\mathrm{I}}(t) + P_{\mathrm{II}}(t) + P_{\mathrm{P\text{-}I}}(t) + P_{\mathrm{P_2\text{-}II}}(t) = 1$.

Similarly, $f_{\mathrm{II}}(\tau) = \mathrm{d}P_{\mathrm{I}}(\tau)/\mathrm{d}\tau$. Using equations B4-B7 to solve for $P_{\mathrm{I}}(\tau)$, $f_{\mathrm{II}}(\tau)$ can be obtained:

$$\langle \tau_{\mathrm{II}} \rangle^{-1} = 1/\int_0^{\infty} \tau f_{\mathrm{II}}(\tau)\mathrm{d}\tau = \frac{k_{-1} + k_6[\mathrm{P}]/K'_{\mathrm{P\text{-}II}}}{1 + [\mathrm{P}]/K'_{\mathrm{P\text{-}II}} + [\mathrm{P}]^2/(K'_{\mathrm{P\text{-}II}} K_{\mathrm{P_2\text{-}II}})}$$

where $K'_{\mathrm{P\text{-}II}} = (k_{-4} + k_6)/k_4$ and $K_{\mathrm{P_2\text{-}II}} = k_{-5}/k_5$. This equation is given as Eq 2 in the main text.

2.6.2.3 Holo-CueR and HJC2 interactions

The kinetic mechanism for holo-CueR–HJC2 interactions is shown in Figure 5B. The kinetic processes happening during τ_{I} are:

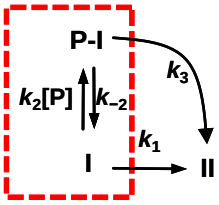

Figure S9 Kinetic scheme for holo-CueR interactions with conf-I of HJC2.

The corresponding single-molecule rate equations are:

$$\mathrm{d}P_{\mathrm{II}}(t)/\mathrm{d}t = k_1 P_{\mathrm{I}}(t) + k_3 P_{\mathrm{P\text{-}I}}(t) \qquad \text{C1}$$

$$\mathrm{d}P_{\mathrm{I}}(t)/\mathrm{d}t = -(k_1 + k_2[\mathrm{P}])P_{\mathrm{I}}(t) + k_{-2} P_{\mathrm{P\text{-}I}}(t) \qquad \text{C2}$$

$$\mathrm{d}P_{\mathrm{P\text{-}I}}(t)/\mathrm{d}t = k_2[\mathrm{P}]P_{\mathrm{I}}(t) - (k_{-2} + k_3)P_{\mathrm{P\text{-}I}}(t) \qquad \text{C3}$$

The initial conditions are $P_{\mathrm{I}}(0)=1$, $P_{\mathrm{II}}(0)=0$ and $P_{\mathrm{P\text{-}II}}(0)=0$ and at any time, $P_{\mathrm{I}}(t)+P_{\mathrm{II}}(t)+P_{\mathrm{P\text{-}I}}(t)=1$. Similarly, $f_{\mathrm{I}}(\tau)=\mathrm{d}P_{\mathrm{II}}(\tau)/\mathrm{d}\tau$, and solving equations C1-C3 for $P_{\mathrm{II}}(\tau)$, $f_{\mathrm{I}}(\tau)$ can be calculated and therefore:

$$\langle\tau_{\mathrm{I}}\rangle^{-1}=1/\int_0^{\infty}\tau f_{\mathrm{I}}(\tau)\mathrm{d}\tau=\frac{k_1+[\mathrm{P}]k_3/K'_{\mathrm{P\text{-}I}}}{1+[\mathrm{P}]/K'_{\mathrm{P\text{-}I}}}$$

where $K'_{\mathrm{P\text{-}I}}=(k_{-2}+k_3)/k_2$. This equation is given as Equation 3 in the main text.

The kinetic processes happening during τ_{II} are:

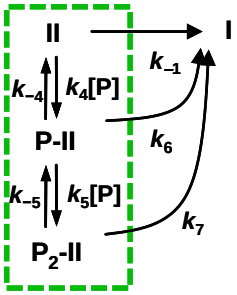

Figure S10 Kinetic scheme for interactions of holo-CueR with HJC2's conf-II.

The corresponding single-molecule rate equations are:

$$\mathrm{d}P_{\mathrm{I}}(t)/\mathrm{d}t=k_{-1}P_{\mathrm{II}}(t)+k_6P_{\mathrm{P\text{-}II}}(t)+k_7P_{\mathrm{P_2\text{-}II}}(t) \qquad \text{C4}$$

$$\mathrm{d}P_{\mathrm{II}}(t)/\mathrm{d}t=-(k_{-1}+k_4[\mathrm{P}])P_{\mathrm{II}}(t)+k_{-4}P_{\mathrm{P\text{-}II}}(t) \qquad \text{C5}$$

$$\mathrm{d}P_{\mathrm{P\text{-}II}}(t)/\mathrm{d}t=k_4[P]P_{II}(t)-(k_{-4}+k_6+k_5[\mathrm{P}])P_{\mathrm{P\text{-}II}}(t)+k_{-5}P_{\mathrm{P_2\text{-}II}}(t) \qquad \text{C6}$$

$$\mathrm{d}P_{\mathrm{P_2\text{-}II}}(t)/\mathrm{d}t=k_5[P]P_{P-II}(t)-(k_{-5}+k_7)P_{\mathrm{P_2\text{-}II}}(t) \qquad \text{C7}$$

The initial conditions for solving above equations are: $P_{\mathrm{II}}(0)=1$, $P_{\mathrm{I}}(0)=0$, $P_{\mathrm{P\text{-}II}}(0)=0$, and $P_{\mathrm{P_2\text{-}II}}(0)=0$. And at any time, $P_{\mathrm{I}}(t)+P_{\mathrm{II}}(t)+P_{\mathrm{P\text{-}I}}(t)+P_{\mathrm{P_2\text{-}I}}(t)=1$.

Similarly, $f_{\mathrm{II}}(\tau) = \mathrm{d}P_{\mathrm{I}}(\tau)/\mathrm{d}\tau$. Using equations C4-C7 to solve for $P_{\mathrm{I}}(\tau)$, $f_{\mathrm{II}}(\tau)$ and $\langle\tau_{\mathrm{II}}\rangle^{-1}$ can be obtained for holo-CueR–HJC2 interactions.

Inconveniently, the expressions of the solutions to equations C4–C7 are too complex to present here. To get a tractable analytical expression for $\langle\tau_{\mathrm{II}}\rangle^{-1}$, k_{-4} was arbitrarily set to zero and get:

$$\langle\tau_{\mathrm{II}}\rangle^{-1} = \frac{k_{-1} + [\mathrm{P}]\left(k_{-1}k_7/(k_6K'_{\mathrm{P_2\text{-}II}}) + k_6/K'_{\mathrm{P\text{-}II}}\right) + [\mathrm{P}]^2 k_7/(K'_{\mathrm{P\text{-}II}}K'_{\mathrm{P_2\text{-}II}})}{1 + [\mathrm{P}]\left(k_7/(k_6K'_{\mathrm{P_2\text{-}II}}) + 1/K'_{\mathrm{P\text{-}II}}\right) + [\mathrm{P}]^2/(K'_{\mathrm{P\text{-}II}}K'_{\mathrm{P_2\text{-}II}})}$$

where $K'_{\mathrm{P\text{-}II}} = k_6/k_4$ and $K'_{\mathrm{P_2\text{-}II}} = (k_{-5} + k_7)/k_5$. This equation is given as Equation 4 in the main text. As this equation can satisfactorily interpret the [holo-CueR] dependence of $\langle\tau_{\mathrm{II}}\rangle^{-1}$, it was used to fit the holo-CueR data in Figure 4B to obtain other relevant kinetic parameters.

APPENDIX

2.7 Probing DNA-unwinding by holo-CueR

2.7.1 Design of unwinding-sensitive Holliday-junction (HJC3)

The crystal structures of the holo-protein-bound DNA duplex for other members of the MerR family (i.e. MtaN and BmrR) indicate that binding of holo-protein would induce DNA unwinding (~30^{o}) on top of DNA bending.[23,24] These crystal structures support the proposed DNA distortion mechanism by O'Halloran.[18] The proposed mechanism suggests that binding of apo-protein bends the DNA without unwinding it, at which transcription is suppressed. When metal binds (i.e. holo-protein), unwinding occurs on top of bending and this structural change leads to the formation of a transcription active complex with RNAp. To fully understand this mechanism of activation, there is a need to structurally differentiate holo-protein-DNA complex from that of apo-protein-DNA complex. Though crystal structures of DNA-bound holo-form of other members of the MerR family are already available, the DNA-bound apo-form still remains to be elucidated. Thus, the structural differences between the two DNA-bound forms have not yet been fully resolved.

Here an engineered HJ (HJC2) has been applied to study the dynamics of interactions of CueR and DNA. In HJC2, due to the helical nature of DNA, unwinding of arms *M* and *N* would bring Cy3 around the axis of the *M*-*N* helix (Figure 2.8 A); this motion would lead to a possible increase in distance between Cy3 and Cy5 and a concomitant decrease in the value of $E_{\text{conf-I}}$. However, data from HJC2 showed no difference, within the experimental error, in the $E_{\text{conf-I}}$ between the apo-CueR bound state (0.64 ± 0.01) and the holo-CueR bound state (0.63 ± 0.01) (Figures 2.6B, C). In order to report DNA unwinding more sensitively, I redesigned HJC2, referred to as HJC3, by transferring Cy3 to the other strand of arm *M* (Figure 2.8 B). In HJC3, Cy3

is now on the other side of the helix compared with that in HJC2 (i.e. outer side helix of arm *M*, away from arm *Q*) as shown in Figure 2.8B(i) (inside the box). Unwinding of the *M-N* helix of HJC3 conf-I would bring Cy3 to the inner side of arm *M*'s helix, thus decreasing the distance between the two fluorophores (Figure 2.8B(ii)). As a result, $E_{\text{conf-I}}$ is expected to increase. From molecular modeling using Swiss Pdb Viewer 4.0.1, the magnitude of the increase in E_{FRET} expected for HJC3 unwinding (by ~1 base pair) is larger than the expected decrease in the E_{FRET} for unwinding in HJC2. It is therefore expected that HJC3 is more sensitive to DNA unwinding than HJC2. Figure 2.9 shows the sequence design of HJC3 where one base pair (A-T) was added to arm *M* and Cy3 was moved from the 5' end of strand *a* (for HJC2) to the 3' end of strand *d*.

2.7.2 Preliminary results and analysis

Single-molecule experiments on HJC3 were done in a similar manner to experiments performed on HJC2. Preliminary results on the values of $E_{\text{conf-I}}$ before and after addition of apo- and holo-CueR are shown in Figure 2.10A (first panel). The $E_{\text{conf-I}}$ value of free HJC3 is 0.57 ± 0.01 which is slightly smaller than that of HJC2 (0.59 ± 0.01). This difference is expected since the distance between Cy3 and Cy5 in HJC3 is larger than in HJC2. After addition of apo-CueR, an increase in $E_{\text{conf-I}}$ of HJC3 was observed (Figure 2.10A, middle panel: $E_{\text{conf-I}} = 0.61 \pm 0.01$). This is consistent with the results obtained from HJC2 where binding of apo-CueR led to an increase of $E_{\text{conf-I}}$ (Figure 2.6B), attributable to the bending of arm *M* towards arm *Q*, decreasing the distance between Cy3 and Cy5 (Figure 2.10B). When holo-CueR was added, a further increase in $E_{\text{conf-I}}$ was observed, 0.67 ± 0.01 (Figure 2.10A, lowest panel). This difference in $E_{\text{conf-I}}$ values between holo-bound and apo-bound HJC3 indicates structural differences between the two complexes, possibly due to the further

DNA unwinding imposed by holo-CueR (Figure 2.10C).

The above preliminary results suggest that HJC3 could monitor structural changes between apo- and holo-CueR bound DNA. However, it still remains to be proven that the changes in E_{FRET} values observed here are due to holo-CueR induced unwinding on top of DNA bending. It has been shown that the energy transfer between Cy3 and Cy5 terminally attached to 5' ends of a DNA duplex is significantly influenced by the fluorophores' relative orientation.[44] Since these fluorophores have been shown to stack on the ends of the helix, the E_{FRET} values obtained could be influenced by the orientation of the dyes and not just the distance between them. Nevertheless, since the same HJ was used for both apo- and holo-CueR binding, differences between the $E_{conf\text{-}I}$ obtained for HJC3 are indeed differences in the structural changes on DNA imposed by the protein. Our lab is currently in the process of probing these DNA structural differences between apo- and holo-CueR bound HJ.

Differences between apo- and holo-CueR, both in the dynamics of protein-DNA interactions as well as in the protein-induced DNA structural changes, define the biological function of CueR, as well as other members of the MerR-family of regulators. Though crystal structures of holo-protein-DNA complex of other members of the MerR family are available, [23,24] no DNA-bound apo-form crystal structures exist to date. Thus, the structural differences between the apo- and holo-protein bound DNA have not yet been fully resolved. By using an engineered HJ as an smFRET reporter, these subtle differences were detected not only in the structure but also in the dynamics of regulator-DNA interactions, which would otherwise be challenging to measure using conventional ensemble and single molecule FRET experiments.

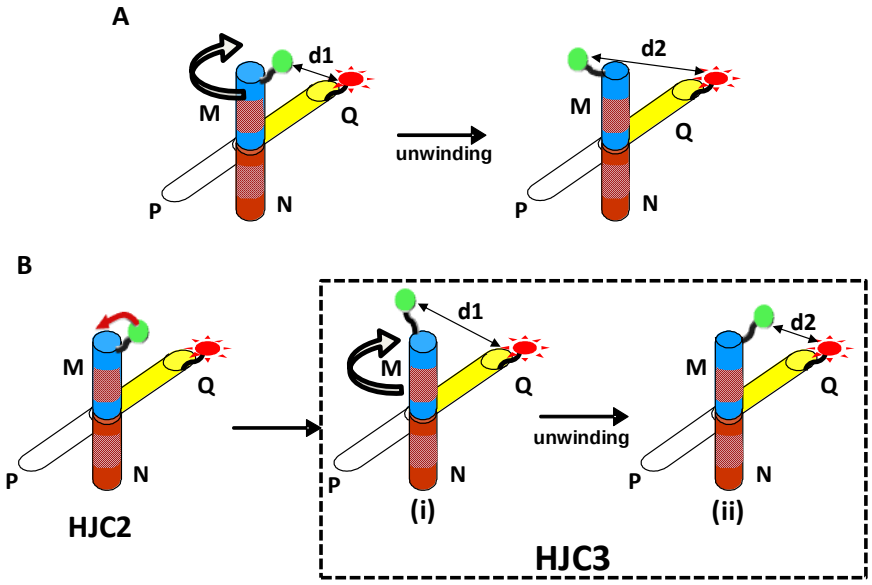

Figure 2.8 Holliday-junction design to probe DNA unwinding by holo-CueR. (A) Unwinding of HJC2 brings Cy3 to the outer portion of the DNA helix, thus increasing the inter-dye distance, d1 < d2. The E_{FRET} value is therefore expected to decrease upon unwinding. (B) Transfer of Cy3 to the other strand of arm *M* (of HJC2) to form HJC3 (inside box (i)). Cy3 is now attached to the outer portion of the DNA helix. Unwinding of HJC3 (inside box (ii)) will bring Cy3 closer to Cy5, d2 < d1, thus increasing the E_{FRET} value. The parameters d1 and d2 are the distances between the fluorophores before and after unwinding.

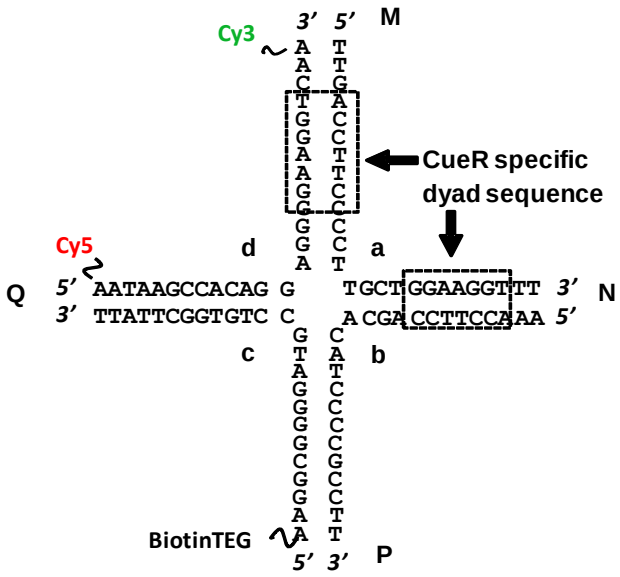

Figure 2.9 CueR-specific HJC3 design. Compared with HJC2, HJC3 has one base pair added to arm *M* and Cy3 was transferred to the 3' end of strand *d* (on arm M). The rest of the HJ was kept similar to HJC2.

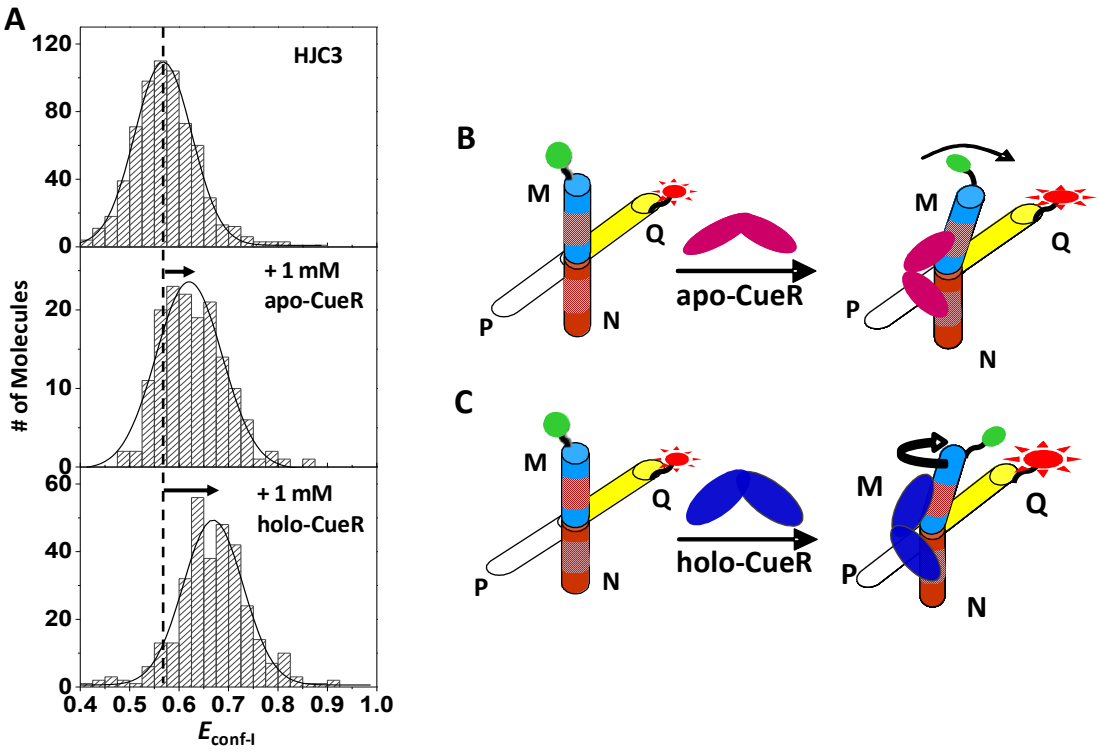

Figure 2.10 (A) Histograms of E_{conf-I} of HJC3 in the presence of 1 mM apo-CueR and holo-CueR. Solid lines are Gaussian fits centered at: 0.57 ± 0.01 (HJC3 only), 0.62 ± 0.01 (w/ 1 mM apo-CueR), and 0.67 ± 0.01 (w/ 1 mM holo-CueR). (B-C) Scheme of HJC3-CueR interaction based on E_{conf-I} values in panel A. (B) Apo-CueR-imposed helix bending of conf-I brings arms *M* and *Q* (i.e. the two fluorophores) closer together. (C) In addition to bending, holo-CueR unwinds arms *M* and *N*. This brings Cy3 and Cy5 even closer together as compared to just bending in panel B.

REFERENCES

(1) Holm, R. H.; Kennepohl, P.; Solomon, E. I. *Chem. Rev.* **1996**, *96*, 2239-2314.

(2) Finney, L. A.; O'Halloran, T. V. *Science* **2003**, *300*, 931-936.

(3) O'Halloran, T. V. *Science* **1993**, *261*, 715-725.

(4) Barkey, T.; Miler, S. M.; Summers, A. O. *FEMS Microbiol. Rev.* **2003**, *27*, 355-384.

(5) Brown, N. L.; Stoyanov, J. V.; Kidd, S. P.; Hobman, J. L. *FEMS Microbiol. Rev.* **2003**, *27*, 145-163.

(6) Busenlehner, L.; Pennella, M. A.; Giedroc, D. P. *FEMS Microbiol. Rev.* **2003**, *27*, 131-143.

(7) Andrews, S. C.; Robinson, A. K.; Rodriguez-Quinones, F. *FEMS Microbiol. Rev.* **2003**, *27*, 215-237.

(8) Cavet, J. S.; Borrelly, G. P. M.; Robinson, N. J. *FEMS Microbiol. Rev.* **2003**, *27*, 165-181.

(9) Kehres, D. G.; Maguire, M. E. *FEMS Microbiol. Rev.* **2003**, *27*, 263-290.

(10) Lloyd, J. R. *FEMS Microbiol. Rev.* **2003**, *27*, 411-425.

(11) Mergeay, M.; Monchy, S.; Vallaeys, T.; Auquier, V.; Benotmane, A.; Bertin, P.; Taghavi, S.; Dunn, J.; van der Lelie, D.; Wattiez, R. *FEMS Microbiol. Rev.* **2003**, *27*, 385-410.

(12) Mulrooney, S. B.; Hausinger, R. P. *FEMS Microbiol. Rev.* **2003**, *27*, 239-261.

(13) Nies, D. H. *FEMS Microbiol. Rev.* **2003**, *27*, 313-339.

(14) Rensing, C.; Grass, G. *FEMS Microbiol. Rev.* **2003**, *27*, 197-213.

(15) Solioz, M.; Stoyanov, J. V. *FEMS Microbiol. Rev.* **2003**, *27*, 183-195.

(16) Hobman, J. L.; Wilkie, J.; Brown, N. L. *BioMetals* **2005**, *18*, 429-436.

(17) O'Halloran, T. V.; Frantz, B.; Shin, M. K.; Ralston, D. M.; Wright, J. G. *Cell* **1989**, *56*, 119-129.

(18) Frantz, B.; O'Halloran, T. V. *Biochemistry* **1990**, *29*, 4747-4751.

(19) Giedroc, D. P.; Arunkumar, A. I. *Dalton Trans.* **2007**, 3107-3120.

(20) Chen, P. R.; He, C. *Curr. Opin. Chem. Biol.* **2008**, *12*, 214-221.

(21) Permina, E. A.; Kazakov, A. E.; Kalinina, O. V.; Gelfand, M. S. *BMC Microbiology* **2006**, *6*, 49.

(22) Chen, P.; He, C. *J. Am. Chem. Soc.* **2004**, *126*, 728-729.

(23) Zheleznova, E. E.; Brennan, R. G. *Nature* **2001**, *409*, 378-382.

(24) Newberry, K. J.; Brennan, R. G. *J. Biol. Chem.* **2004**, *279*, 20356-20362.

(25) Michalet, X.; Weiss, S.; Jaeger, M. *Chem. Rev.* **2006**, *106*, 1785-1813.

(26) Ha, T. *Methods* **2001**, *25*, 78-86.

(27) Zhuang, X. *Annu. Rev. Biophys. Biomol. Struct.* **2005**, *34*, 399-414.

(28) Sarkar, S. K.; Andoy, N. M.; Benitez, J. J.; Chen, P. R.; Kong, J. S.; He, C.; Chen, P. *J. Am. Chem. Soc.* **2007**, *129*, 12461-12467.

(29) McKinney, S. A.; Declais, A. C.; Lilley, D. M. J.; Ha, T. *Nat. Struct. Biol.* **2003**, *10*, 93-97.

(30) Lilley, D. M. J. *Q. Rev. of Biophys.* **2000**, *33*, 109-159.

(31) Karymov, M. A.; Chinnaraj, M.; Bogdanov, A.; Srinivasan, A. R.; Zheng, G.; Olson, W. K.; Lyubchenko, Y. L. *Biophys J.* **2008**, *95*, 4372-4383.

(32) Ortiz-Lombardía, M.; González, A.; Eritja, R.; Aymamí, J.; Azorín, F.; Coll, M. *Nat. Struct. Biol.* **1999**, *6*, 913-917.

(33) Eichman, B. F.; Vargason, J. M.; Mooers, B. H. M.; Ho, P. S. *Proc. Natl. Acad. Sci. USA* **2000**, *97*, 3971-3976.

(34) Outten, F. W.; Outten, C. E.; Hale, J.; O'Halloran, T. V. *J. Biol. Chem.* **2000**, *275*, 31024-31029.

(35) Petersen, C.; Moller, L. B. *Gene* **2000**, *261*, 289-298.

(36) Stoyanov, J. V.; Hobman, J. L.; Brown, N. L. *Mol. Microbiol.* **2001**, *39*, 502-511.

(37) Changela, A.; Chen, K.; Xue, Y.; Holschen, J.; Outten, C. E.; O'Halloran, T. V.; Mondragon, A. *Science* **2003**, *301*, 1383-1387.

(38) Yamamoto, K.; Ishihama, A. *Mol. Microbiol.* **2004**, *56*, 215-227.

(39) Heltzel, A.; Lee, I. W.; Totis, P. A.; Summers, A. O. *Biochemistry* **1990**, *29*, 9572-9584.

(40) Ahmed, M.; Borsch, C.; Taylor, S. S.; Vazquez-Laslop, N.; Neyfakh, A. A. *J. Biol. Chem.* **1994**, *269*, 28506-28513.

(41) Brenner, A. J.; Harris, E. D. *Anal. Biochem.* **1995**, *226*, 80-84.

(42) Rasnik, I.; McKinney, S. A.; Ha, T. *Nat. Methods* **2006**, *3*, 891-893.

(43) Heyduk, T.; Lee, J. C. *Proc. Natl. Acad. Sci. USA* **1990**, *87*, 1744-1748.

(44) Iqbal, A.; Arslan, S.; Okumus, B.; Wilson, T. J.; Giraud, G.; Norman, D. G.; Ha, T.; Lilley, D. M. J. *Proc. Natl. Acad. Sci. USA* **2008**, *105*, 11176-11181.

(45) Xie, X. S. *Single Mol.* **2001**, *2*, 229-236.

(46) Xu, W.; Kong, J. S.; Chen, P. *J. Phys. Chem. C* **2009**, *113*, 2393-2404.

CHAPTER THREE

CATALYSIS COUPLED FLUORESCENCE QUENCHING (CCFQ) TO STUDY THE SINGLE MOLECULE ENZYMOLOGY OF TYROSINASE

3.1 Introduction

Recent advances in single-molecule fluorescence spectroscopy have rapidly opened a new era of exploring the behaviors of individual enzyme molecules as they undergo catalytic reactions.[1-18] The power of the single-molecule approach in studying enzymes stems from its many distinctive features. First, it removes ensemble averaging so that heterogeneous behaviors are revealed and subpopulations analyzed. This ability is particularly important for enzymes since heterogeneity easily arises in these systems; seemingly identical copies of enzyme molecules often have non-identical properties (i.e. static disorder). Second, as one molecule can be monitored at a time, synchronization for studying time dependent processes is no longer needed. For enzymes, this allows visualizations of catalytic intermediates that could help elucidate the mechanisms of the enzymatic reactions. Third, since individual molecules can be monitored for an extended period of time, the fluctuations of the catalytic rates for each enzyme (i.e. dynamic disorder) can be probed. These studies will provide unprecedented information on the dynamics of enzymatic reactions which cannot easily be inferred from ensemble measurements.[19,20]

3.1.1 Single-molecule fluorescence methods in enzymology

Many single-molecule fluorescence methods have been developed for monitoring enzyme reactions in real time.[21] These methods include the use of fluorescent substrates,[8,11] fluorescent products (fluorogenic reaction),[4-7,14,16] naturally fluorescent enzyme active sites,[2,12] fluorescence resonance energy transfer (FRET),[1,3,9] and fluorescence quenching via energy transfer either by substrate binding[15,18] or

through a natural quencher in the enzyme like a metal cofactor.[10]

All of the above-mentioned methods probe different stages in the catalytic cycle of an enzyme and provide complementary information about how enzymes work as dynamic biomolecules. So far, most of the enzymes studied with single-molecule fluorescence spectroscopy were those in which the metal cofactors are either not needed or nonessential for the enzyme's function. Very limited single-molecule studies have been reported that probe metal cofactors directly involved in the catalytic reaction.[10] Although several single-molecule studies have directly probed metal centers with strong spectroscopic features, these did not involve enzyme catalysis studies.[22-25] Transition-metal-based catalyses have versatile chemistry and often involve intermediates with intense ligand-to-metal charge transfer absorptions.[26,27] Our approach is to capitalize on these spectroscopic features of metalloenzymes to develop a single-molecule catalysis-coupled fluorescence quenching (CCFQ) methodology. This method is based on the principles of fluorescence quenching via energy transfer. The methodology was applied to study the single-molecule enzymology of tyrosinase by probing the intermediates of the metal active site.

3.1.2 Tyrosinase

Tyrosinase is an enzyme with a binuclear copper (Cu_2) active site, with each copper ion coordinated by three His residues through Nε atoms. It catalyzes the ortho-hydroxylation of monophenol to diphenol (phenolase activity) and its subsequent oxidation to an ortho-quinone (catecholase activity) by activating O_2.[26,28-30] During the catalytic reaction, the copper center can exist in three redox states: (1) met-Tyr, which is the resting form of the enzyme, where both copper atoms are at the +2 oxidation state; (2) deoxy-form (deoxy-Tyr), which is the reduced species and has both coppers in the +1 oxidation state; (3) oxy-Tyr, which can be formed from O_2 binding to deoxy-Tyr and has oxygen bound as peroxide in a side-on fashion in between the two Cu(II)

atoms.[29,31] Oxy-Tyr has strong absorption features while deoxy-Tyr has no absorption features in the visible region.[31] For this study, I capitalize on this strong spectroscopic contrast between oxy-Tyr and deoxy-Tyr to monitor the catalytic turnover of a single tyrosinase molecule. By introducing an appropriate fluorescent probe on the protein, the switching of the copper active site between the tyrosinase's intermediates can be monitored.

3.2 Results and Discussion

3.2.1 Catalysis coupled fluorescence quenching (CCFQ)

Figure 3.1A depicts the approach to study tyrosinase catalysis at the single molecule level. In its catalytic cycle, the oxygenated active intermediate of tyrosinase, oxy-Tyr, reacts with the substrate before it is converted to its reduced state, deoxy-Tyr. This deoxygenated intermediate can then bind O_2 which converts the enzyme back to its oxy-form (Figure 3.1A). In oxy-Tyr, O_2 binds as peroxide to the two Cu(II) centers in a side-on bridging fashion, forming highly covalent Cu(II)-peroxide bonds (Figure 1B, inset). This destabilizes the O–O bond and activates it for hydroxylation reaction. This Cu(II)-peroxide covalent interaction also leads to two intense peroxide-to-copper charge transfer transitions in the absorption spectrum of oxy-Tyr, one centered at ~640 nm ($\varepsilon \sim 1500\ M^{-1}\text{- }cm^{-1}$) and the other at ~350 nm ($\varepsilon \sim 17000\ M^{-1}\text{-}cm^{-1}$). These two transitions arise from peroxide out-of-plane π^*_v and in-plane π^*_σ to Cu charge transfer transitions, respectively (Figure 3.1B). In contrast, deoxy-Tyr has no absorption features in the visible region because of the d^{10} electronic configuration of the two reduced Cu(I) centers.[26]

The CCFQ approach capitalizes on this spectral contrast between the reduced and oxidized intermediates of tyrosinase during the catalytic cycle. The intense absorption of the Cu_2O_2 center of oxy-Tyr can quench the fluorescence of a nearby

fluorescent probe by a fluorescence energy transfer mechanism, while deoxy-Tyr cannot (Figure 3.1A). By introducing an appropriate fluorescent probe close to the binuclear site, turnovers of the enzyme are reported as changes in the fluorescence intensity of the probe. Transitions between high and low levels are expected to accompany the transitions between deoxy-Tyr and oxy-Tyr. The fluorescence intensity fluctuations of each probe will thus monitor tyrosinase reactions in real-time on a single enzyme basis (Figure 3.1C).

In the subsequent sections, I present the development of this single-molecule catalysis coupled fluorescence quenching (smCCFQ) methodology to study and understand the dynamics of metalloenzyme catalysis, using tyrosinase as the prototype. With this method, the heterogeneity of enzyme catalysis (i.e. distribution of kinetic rates) can be investigated. Observing a single tyrosinase molecule undergoing catalysis over a period of time allows me to study dynamic fluctuations of its turnover rate. Both the distribution of kinetics and the dynamic fluctuations are uniquely obtainable from single-molecule measurements.[6,12,20] This approach also directly monitors an intermediate in a catalytic cycle. This fills the gap between substrate binding and product formation, which are the common methods used for single-molecule enzymology studies. And since the intermediate probed involves a transition metal center, CCFQ will open up opportunities for studying transition-metal-based enzyme catalysis on a single-molecule basis.

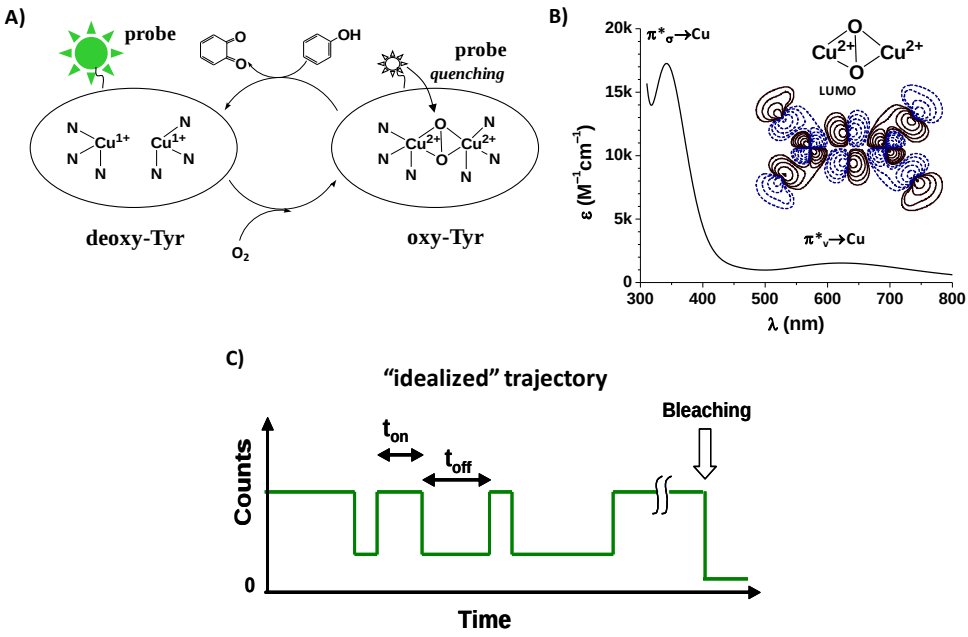

Figure 3.1 (A) Scheme of substrate turnover by tyrosinase and the catalysis-coupled fluorescence quenching (CCFQ) method. (B) Absorption spectrum of Oxy-tyrosinase. Inset: contour plot of the lower unoccupied molecular orbital (LUMO) of the side-on Cu_2O_2 core. The LUMO has large mixing between Cu^{II} d and peroxide π* orbitals, indicating the highly covalent Cu^{II}-peroxide interaction. (C) Scheme of "idealized" fluorescence intensity time trajectory of the probe showing switching events associated with tyrosinase catalysis.

3.2.2 Dye labeling and ensemble fluorescence quenching

Two schemes were tried for attaching a fluorescent probe to the protein: (1) labeling one of the five lysine residues with TAMRA-succinimidyl ester; (2) labeling the C-terminal residue, after D274C mutation, with Cy3-maleimide (see Section 3.4. Materials and Methods). Figure 3.2A displays the crystal structure of *S. castaneoglobisporus* (Sc) tyrosinase showing both the Cu_2-center, the location of the C-terminal residue mutated to Cys, and the five Lys residues targeted for labeling with the probe. These Lys residues are all conserved in *Streptomyces glaucescens* (Sg) tyrosinase, the enzyme used in this study (its crystal structure is not available).[29] Based on the Sc tyrosinase structure, these residues are all likely surface-accessible and the distances between their terminal amine groups and the binuclear Cu_2 active site are ~1.7-2.6 nm. The C-terminal residue of the mutant tyrosinase (Figure 3.2A), which was specifically labeled, is ~2.3 nm away from the Cu_2 center and is 21.5% accessible (Table 3.1). The solvent accessibility of these residues was determined using Swiss-Pdb Viewer 4.0.1. Their distances from the Cu_2 center were determined by measuring the average distance between each of the two copper ions in the active site and the nitrogen atom of the terminal amine for the Lys residues, or the sulfur atom for the C-terminal Cys residue.

TAMRA and Cy3, common dyes in single molecule spectroscopy, were used as the fluorescent probes for reporting catalysis.[32] These dyes were chosen because their fluorescence spectra have large overlaps with the peroxide $\pi^*_v \rightarrow$ Cu charge transfer absorption band of oxy-Tyr at ~640 nm (Figure 3.2B). The Förster radius (R_o) was calculated from the spectral overlap ($J = \int F_D(\lambda)\varepsilon_A(\lambda)\lambda^4 d\lambda \Big/ \int F_D(\lambda) d\lambda$) of the fluorescence spectrum (F_D) of the dye and the absorption spectrum (ε_A) of oxy-Tyr. The calculated R_o's are 3.0 nm and 3.6 nm for TAMRA ↔ oxy-Tyr and Cy3 ↔ oxy-Tyr, respectively (Equation 3.1).

$$Ro = 0.211\left[J\kappa^2 n^{-4} Q_D\right]^{1/6} \qquad \text{Equation 3.1}$$

$$E = \frac{1}{1+\left(R/R_o\right)^6} \qquad \text{Equation 3.2}$$

where Q_D is the quantum yield of donor (Cy3, Q_D = 0.25; TAMRA, Q_D = 0.28),[32,33] n is the refractive index of water and κ^2, the orientation factor, is assumed to be 2/3 for a freely rotating dye.[34] The probes are attached via a flexible linker to allow free rotation. From these Förster radii and the distances of the C-terminal and Lys residues from Cu_2 center, the efficiencies of energy transfer (E) from the probes to the Cu_2O_2 core of oxy-Tyr are estimated to be ~75-97% (Eqn. 3.2, Table 3.1). Therefore, upon formation of oxy-Tyr, there will be a significant fluorescence quenching of the probe (TAMRA or Cy3) labeled at any of these residues.

In the labeling reaction, the stoichiometry, especially for labeling a Lys residue, was controlled to ensure that there is only one probe attached on each protein. The labeling efficiency, [dye]/[Tyr], was calculated after purification, and the values obtained from both are under 50% (~47% for TAMRA and ~10% for C-terminal Cy3-labeled tyrosinase), which implies that on average, less than 1 probe is attached per enzyme molecule (Figure 3.4 A, B). Unlabeled tyrosinase does not affect the single molecule fluorescent measurements since they are non-fluorescent and thus unobservable. The viability of the labeled enzyme was tested using L-DOPA assay and both Cy3- and TAMRA-labeled tyrosinase were active at room temperature.[35] For TAMRA-labeled tyrosinase, the reactivity of the enzyme solution before and after labeling is ~51% and ~41% of the activity obtained for tyrosinase immediately after purification which is ~2000 U/mg (1U = 1 μmol product per minute).[36] For Cy3-labeled mutant tyrosinase, the enzyme viability was ~83% before and ~81% after labeling.

The catalysis-coupled fluorescence quenching of the probes was checked first in ensemble measurements by comparing the fluorescence intensity of the probes when tyrosinase is in its oxy-state and in its deoxy-Tyr state. Addition of NH_2OH reduces tyrosinase to deoxy-Tyr.[30] While taking the fluorescence spectrum, the solution was kept under N_2 to avoid direct formation of oxy-Tyr when deoxy-Tyr is exposed to air (Figure 3.3C, D - dashed lines). When the deoxy-Tyr solution was exposed to air, the enzyme was converted to oxy-Tyr,[31] which caused the fluorescence intensities of the probes to decrease by 58% for TAMRA-labeled and 62% for Cy3-labeled tyrosinase (Figure 3.4C, D – solid lines). This fluorescence quenching at the ensemble level indicates that I have successfully labeled the enzyme with the probes and that their distances from the Cu_2 center allow efficient energy transfer to the active site as it interconverts between oxy- and deoxy-states.

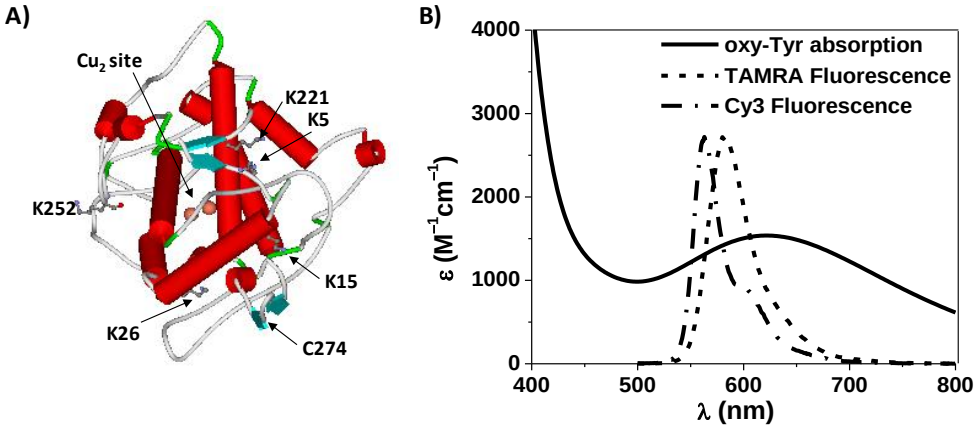

Figure 3.2 (A) Crystal structure of oxy-tyrosinase from *S. castaneoglobisporus* (PDB code 1WX2, Matoba et al. *J. Biol. Chem.* 2006, 281, 8981.) (B) Absorption spectrum of oxy-tyrosinase and fluorescence spectrum of TAMRA and Cy3.

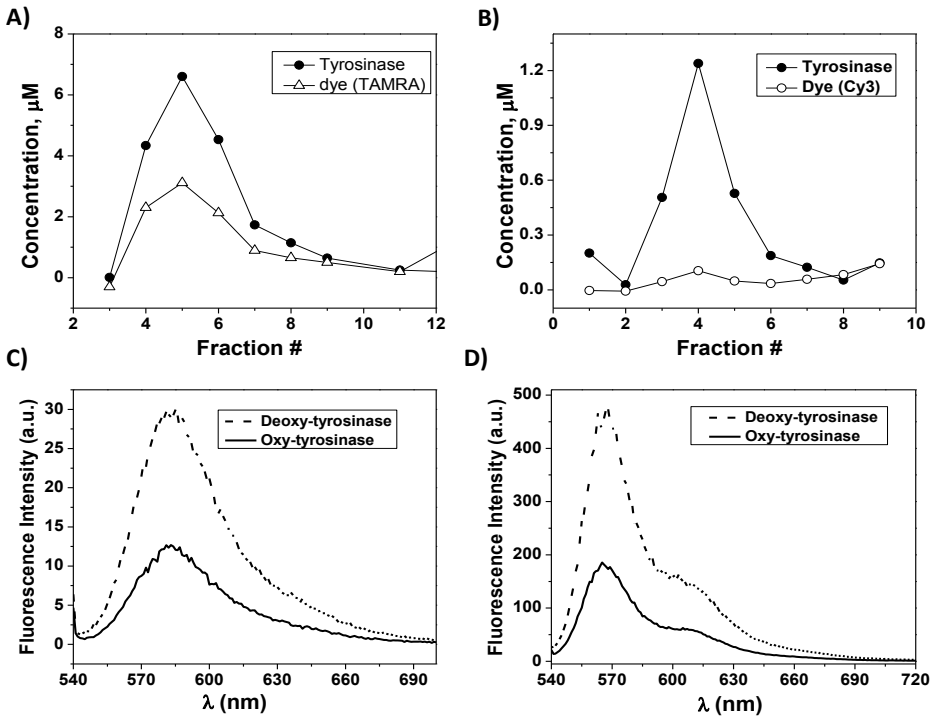

Figure 3.3 (A) Protein and TAMRA concentration of the dye labeled tyrosinase in the collection fractions after purification with a desalting column. Labeling efficiency is ~47%. (B) Protein and Cy3 concentration of labeled tyrosinase in the collected fractions after desalting column purification. Labeling efficiency is ~10%. (C) Ensemble fluorescence spectra of TAMRA-labeled oxy- and deoxy-Tyr excited at 532 nm. The fluorescence quenching in oxy-Tyr is ~58%. (D) Ensemble fluorescence spectra of Cy3-labeled oxy- and deoxy-Tyr excited at 532 nm. The fluorescence quenching in oxy-Tyr is ~62%.

3.2.3 Enzyme immobilization for single-molecule experiments

In order for a single enzyme molecule to be monitored undergoing catalysis over time, it has to be immobilized in the flow cell (sample chamber for single-molecule experiments) without altering its activity. To this end, two immobilization methods were tested. The first is via direct immobilization of TAMRA-labeled tyrosinase on amine-coated quartz slide. It was found that tyrosinase could be immobilized on a positively charged amine-coated surface via electrostatic interactions, since it is negatively charged (pI is ~6.8) at pH 8.5. To ensure that tyrosinase remains active under the immobilization condition, the ensemble activity (L-DOPA assay) of tyrosinase immobilized on amine-functionalized surfaces was checked prior to single-molecule experiments (See Materials and Methods Section 3.4.3). The increase in the absorption of the reaction solution at 475 nm confirms the formation of the oxidized product L-DOPA quinone (data not shown) and thus the activity of the enzyme.

The second form of immobilization is trapping the enzyme inside porous nanovescicles.[38,39] For these experiments, C-terminal Cy3-labeled tyrosinase was used. Since the labeled protein is encapsulated inside lipid vesicles, glass surface interactions with the protein and the probe are prevented.[37] Porous nanovesicle trapping would not only make it possible to immobilize tyrosinase, so its activity can be monitored over time, but also allow exchange of substrate (and product) molecules with the surrounding media (Figure 3.5A). I can therefore easily change solution conditions (e.g., change substrate concentration) and also wash out products as they are formed during the reaction by having a continuous solution flow. This ability to change solution conditions is particularly important for enzyme catalysis since substrate molecules are continuously consumed, and therefore have to be replenished. Products that are formed could also act as inhibitors, and therefore also have to be

removed from the vicinity of the enzyme.

The formation of pores on the nanovesicles comes from the characteristic property of the lipid membranes near the melting temperature (T_m) of its component phospholipid. At T_m, the phospholipid membrane equilibrates between its gel phase and fluid phase giving rise to defects in the lipid packing.[37-39] In my experiments, DMPC (1,2-dimyristoyl-*sn*-glycero-3-phosphocholine) whose T_m is close to room temperature, $23.5 \pm 2.5\ ^{o}C$, was used. In order to keep the DMPC-nanovesicle porous during the entire duration of the single molecule experiment, the sample chamber was kept at ~24 ^{o}C using a stage warmer (See Section 3.4.3 in Materials and Methods).

The porosity of the immobilized nanovesicles to small molecules and their ability to trap large molecules, Figure 3.4A, were tested by monitoring the structural interconversion of HJC2a in the presence and absence of divalent metal ions (reference Chapter 2 Section 2.2).[40] In the presence of $MgCl_2$ and NaCl, structural interconversions between the two HJ conformations, as reported by the E_{FRET} fluctuations, were observed (Figure 3.4 B). These structural interconversions did not occur when both $MgCl_2$ and NaCl were removed from the solution (Figure 3.4 C). When both salts were re-introduced into the sample chamber, fluctuations in E_{FRET} were again observed (Figure 3.4 D). These results confirm that the HJ molecule was successfully trapped inside the porous vesicles and that divalent and monovalent ions can freely pass through the membrane. Other studies have shown that these pores can allow exchange of ATP molecules through the pores while molecules only about twice the size of ATP remain encapsulated without leakage over long periods.[38] These pores could therefore allow exchange of L-tyrosine and its quinone product, which are smaller than ATP, while keeping the 30 kDa protein trapped inside.

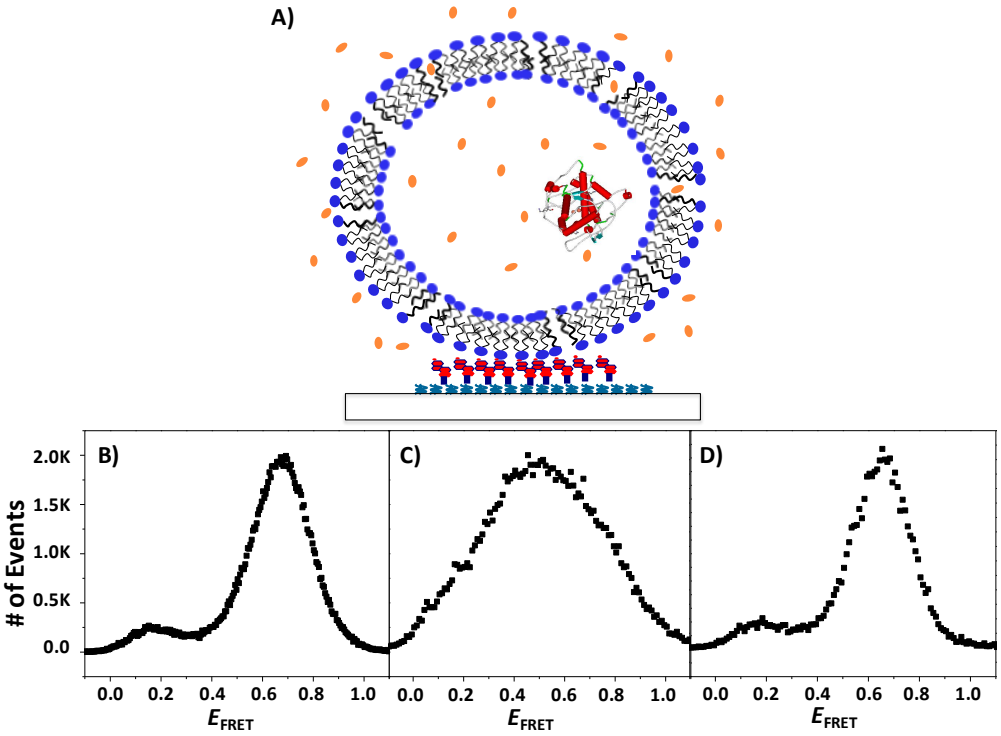

Figure 3.4 (A) Scheme of porous nanovesicle-trapped tyrosinase immobilized on quartz slide for single molecule experiment. Substrate molecules diffusing in and out of the vesicle through the pores are represented by the circles. (B-D) Single molecule (sm) E_{FRET} histogram of Holliday junction (HJ) labeled with Cy3 and Cy5 trapped inside the porous nanovesicle in 10 mM pH 7.35 Tris buffer: (B) in the presence of 2 mM $MgCl_2$ and 10 mM NaCl where HJ undergoes structural interconversion between a high- and a low-FRET state; (C) after washing out the salt with just plain buffer solution; (D) after re-introduction of 2 mM $MgCl_2$ and 10 mM NaCl in Tris buffer into the flow cell.

3.2.4 Sm-CCFQ on amine-immobilized tyrosinase

For single molecule experiments on TAMRA-labeled tyrosinase immobilized on amine-functionalized surfaces, a few of the single-molecule fluorescence intensity trajectories displayed clear two-state fluctuations, between a high emission intensity and a low one; the low state is still higher than the background. This type of emission intensity was observed under catalytic conditions (i.e., in the presence of the substrate L-tyrosine and O_2). Figures 3.5A and B are examples of these sm-traces (single-molecule traces) in the presence of 1.0 mM and 0.01 mM L-tyrosine, respectively. These transitions between high and low intensity states could represent real-time single enzymatic turnovers when the enzyme interconverts between oxy-Tyr (low intensity or *off-state*) and deoxy-Tyr (high intensity or *on-state*) as the substrate, L-tyrosine, is being oxidized to L-DOPA by O_2. Thus, each on-off cycle corresponds to one turnover event (during which a single reactant molecule is being converted to product). The average single-molecule turnover rate, i.e., number of turnovers per second per enzyme, was obtained using threshold analysis.[40,41] Here, the threshold used to differentiate the *on-state* from *off-state* was determined from the fluorescence intensity distribution. Once the threshold was set, the duration of *on-state* (τ_{on}) and *off-state* (τ_{off}) times were used to calculate the turnover rate. The calculated turnover rates for Figure 3.5A and B are ~5 s^{-1} and ~14 s^{-1}, respectively.

This type of two-state behavior, however, was also observed in the control experiments, where no substrate was introduced (Figure 3.5C, turnover rate ~2 s^{-1}). To differentiate between control and catalysis experiments, the distribution of turnover rates under different substrate concentrations was analyzed. Figure 3.6A and B show the distributions of these average turnover rates in the presence of 0.01 mM and 1.0 mM L-tyrosine, respectively. The substrate concentrations were chosen based on the

K_M of tyrosinase for L-tyrosine oxidation, 0.41 mM.[42] On average, a slower turnover rate is expected in the presence of 0.01mM L-tyrosine since it is well below the K_M of the reaction. At 1.0 mM L-tyrosine, the average turnover rate should be closer to the reaction's k_{cat}, which is ~13 s^{-1}.[42] The histogram for the control experiment (without substrate) is shown in Figure 3.6C. Comparing these histograms (Figure 3.6A-C), no significant differences were observed between the control experiment and that obtained from traces in the presence of L-tyrosine. The average single-molecule turnover rates, with errors from the standard error of the mean (sem), obtained from the histograms are 3.8 ± 0.2 s^{-1} (0.01mM L-tyrosine), 3.9 ± 0.2 s^{-1} (1.0 mM L-tyrosine), and 3.6 ± 0.3 s^{-1} (control). These results did not show significant differences in the "turnover rate" calculated between experiments under catalytic conditions and that from the control. This finding suggests that those traces showing clear two-state fluctuations cannot be reliably attributed to catalytic turnovers, since they can also result from the photophysical properties of the probe (i.e. TAMRA). The possible causes for this "on-dim" blinking behavior will be discussed below.

Not all fluorescence trajectory traces obtained from the single-molecule experiments show these 2-state fluctuations. In fact, the majority of the sm-traces show only large intensity fluctuations, Figure 3.8A, where the lowest intensity is still higher than the background. These fluctuations could either come from the fluorescence quenching/dequenching of the TAMRA-probe due to enzymatic turnovers or, like the 2-state fluctuations, or come from the emission fluctuations of TAMRA. To differentiate between these two possibilities, since thresholding analysis cannot be applied, the autocorrelation function of the intensity trajectory $C(t) = \langle \Delta I(0) \Delta I(t) \rangle / \langle \Delta I^2 \rangle$ was calculated, where *I(t)* is the time dependent fluorescence intensity and "$\langle\ \rangle$" denotes time averaging.[6,7,12,43] The resulting function shows a decay behavior and can be fitted by a single exponential function to obtain the

time constant, the inverse of which corresponds to the turnover rate (~5.9 s^{-1}, Figure 3.7B), assuming that the fluctuations result from catalytic turnovers. The autocorrelation functions shown in Figure 3.7 are plotted in a linear-log scale to clearly show the decay behavior (first point at t = 0 is 1 and is not included in the fit). The same analysis was also done for fluctuating trajectories that were detected in the absence of the substrate (i.e., control experiment). The resulting autocorrelation functions are similar to that shown in Figure 3.7B and were also fitted with a single exponential function. From the time constant of the fit, the turnover rate for each trajectory was then calculated. The distributions of the rates obtained are shown in Figure 3.8A-C with average turnover rates of: (A) ~5.4 $\pm$ 0.57 s^{-1} (1.0 mM L-tyrosine), (B) ~2.7 $\pm$ 0.29 s^{-1} (0.01 mM L-tyrosine), and (C) ~4 $\pm$ 1.03 s^{-1} (control). Although in the presence of 1.0 mM L-tyrosine, there was a slight increase in the number of molecules showing higher turnover rates, the majority of the traces still have similar behaviors to those from control experiments. Again, the results suggest that the fluorescence intensity fluctuations observed here cannot be reliably attributed to reflect the catalysis of the enzyme, but instead reflect just the photophysical properties of TAMRA.

Figure 3.7C is an example of another type of fluorescence trace observed in the absence of substrate (control) where no large intensity fluctuations (except for photon detection noise) were observed. Its intensity autocorrelation function also does not show a decay behavior (Figure 3.7D). Sm-traces that do not show fluctuations were also observed in the presence of L-tyrosine, which could be attributed to labeled-enzymes that are inactive.

Results obtained from both thresholding and autocorrelation analyses of single molecule fluorescence intensity trajectories, in the presence and absence of L-tyrosine, did not give any conclusive evidence that catalytic turnovers of single tyrosinase

molecules can be detected using CCFQ on TAMRA-labeled tyrosinase immobilized on amine-functionalized surfaces. One possible reason is that the labeled enzyme, the only ones detected from the single molecule experiments, is no longer active. Although the ensemble activity of the labeled tyrosinase was tested, the enzyme solution used for that experiment also includes the unlabeled protein since labeled and unlabeled enzyme molecules were not separated. Unlabeled enzymes will not contribute to single-molecule fluorescence measurements since they are not fluorescent. It is possible that the probe could interfere with substrate binding thus rendering the labeled-tyrosinase inactive. Although some of the Lys residues are located away from the active site, the most solvent-accessible Lys, which is more likely to be labeled, is located right next to the cavity of the enzymes active site (Lys 252 Figure3.2A). TAMRA attached to this residue could inhibit binding of the substrate by blocking the cavity where the substrate access the active site. Based on the ensemble activity assay and labeling results (See Section 3.2.2), however, enzyme activity before and after labeling decreased by only ~10% while the labeling efficiency was 47%. This observation suggests that some of the labeled enzymes are still active so the effect of labeling would not be enough to explain the observed results.

Another possible reason that I did not detect differences between control and catalysis experiments is the surface effects, since the labeled-protein is directly interacting with the amine-functionalized surface. Direct surface immobilization could render some of the enzymes inactive or could block the binding site of some enzymes due to the random orientation upon binding. Also, even though some of the labeled enzymes remain active after immobilization, interactions of the probe with the surface could affect the

intensity fluctuations. It has been shown that cyanine dyes immobilized on a glass surface exhibit intensity fluctuations similar to those seen here (i.e. high and low intensities, where the low intensity is still higher than the background).[44] These fluctuations could contribute significantly to the observe statistics since a large fraction of the probe is likely in direct contact with the glass surface.

The intrinsic photophysics of the probe could contribute significantly to the observed intensity fluctuations during single-molecule experiments. Photo-induced spectral shifts and changes in the emission yield can be some of the main contributors to the observed fluctuations. In addition, polarization effects and intersystem crossing (ISC) to a triplet state can be important contributions to the fluctuations.[33,34,44-46] Even though ISC is expected to bring the dye in a dark state known as "on-off blinking" (i.e. no fluorescence intensity, observed intensity should be equal to the background), if the lifetime of the triplet state is shorter than the time resolution, these would induce fluctuations with low intensities higher than the background, "on-dim blinking", just like what I observed from single-molecule experiments. Triplet state quenchers have been used in many single-molecule experiments to suppress its formation. β-mercaptoethanol (BME) and trolox are the most common reagents.[37,40] However, these cannot be used to study tyrosinase enzymology because the thiol group in BME can bind to the copper center rendering the enzyme inactive, and trolox is an inhibitor for tyrosinase (data not shown).

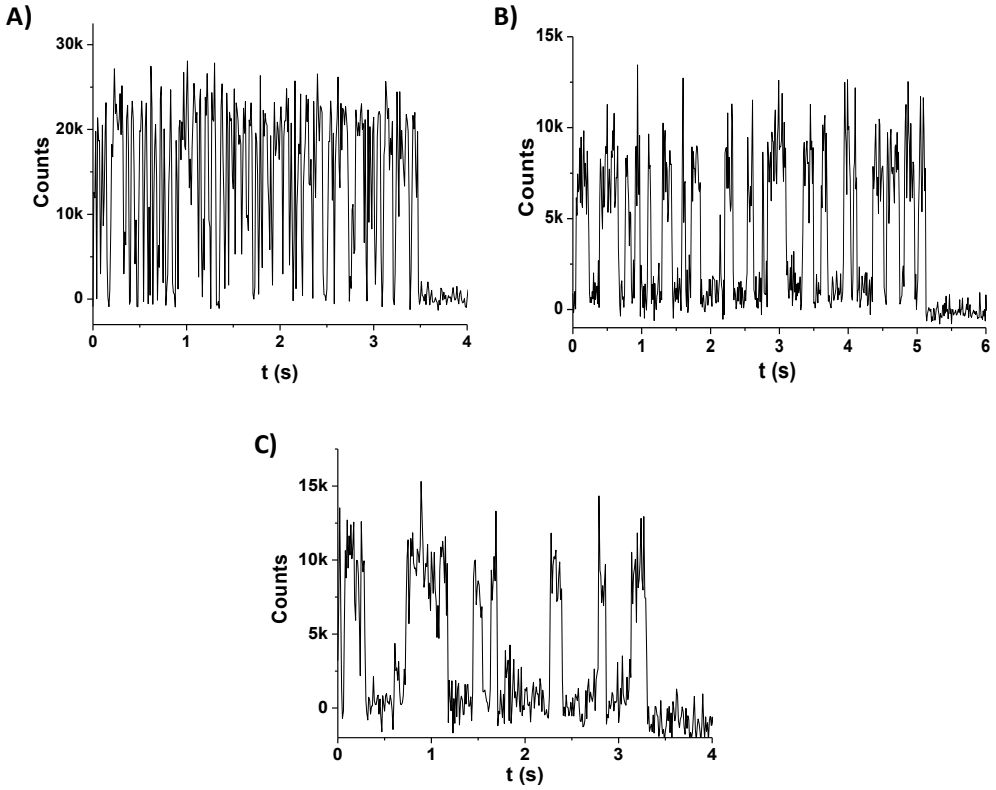

Figure 3.5 Fluorescence intensity trajectories of single TAMRA-labeled tyrosinase molecules in the presence of: (A) 1.0 mM L-tyrosine (turnover rate ~14 s^{-1}); (B) 0.01 mM L-tyrosine (turnover rate ~5 s^{-1}); and (C) control experiment, without substrate (turnover rate ~2 s^{-1}).

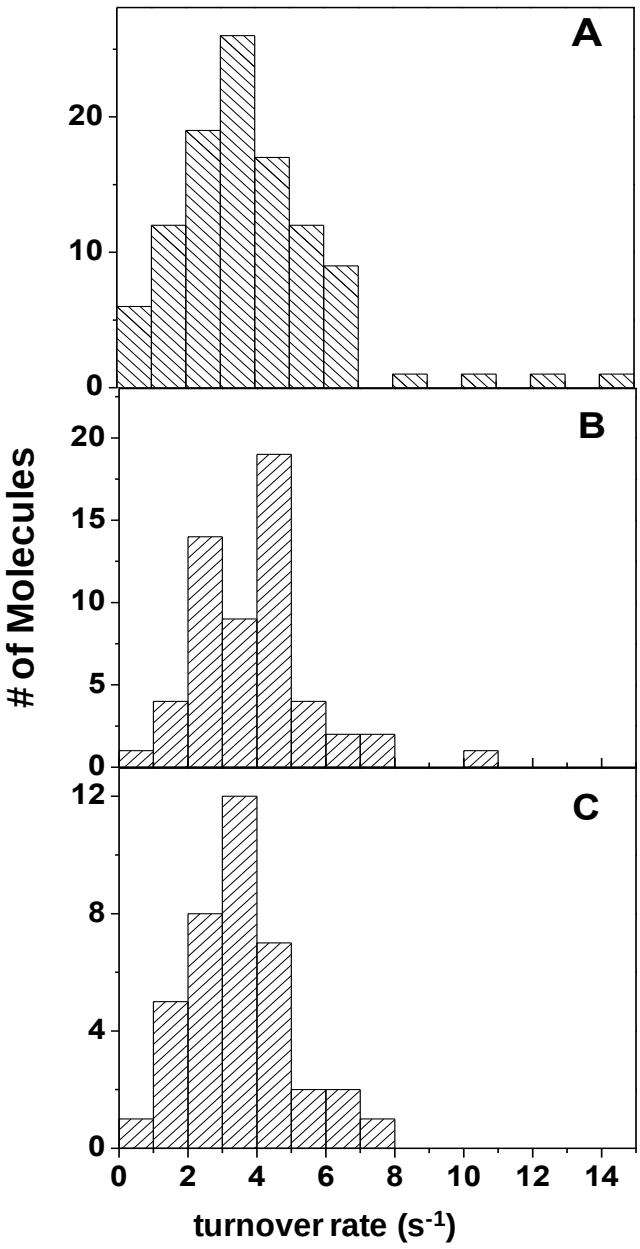

Figure 3.6 Histogram of the average turnover rates per molecule with (A) 1.0 mM L-tyrosine (B) 0.01 mM L-tyrosine (C) no substrate (control).

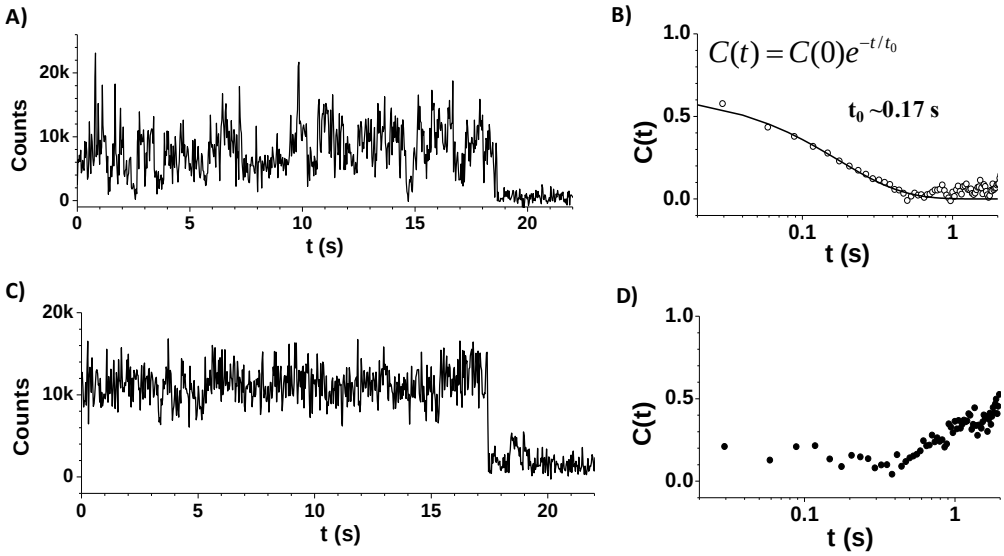

Figure 3.7 Fluorescence intensity trajectories of single TAMRA-labeled tyrosinase molecules in the presence (A) and absence (B) of the substrate L-tyrosine. (B,D) autocorrelation functions of the corresponding trajectories. Solid line in (C) fit with $C(t)=C(0)\exp(-t/t_o)$, t_o~0.17s.

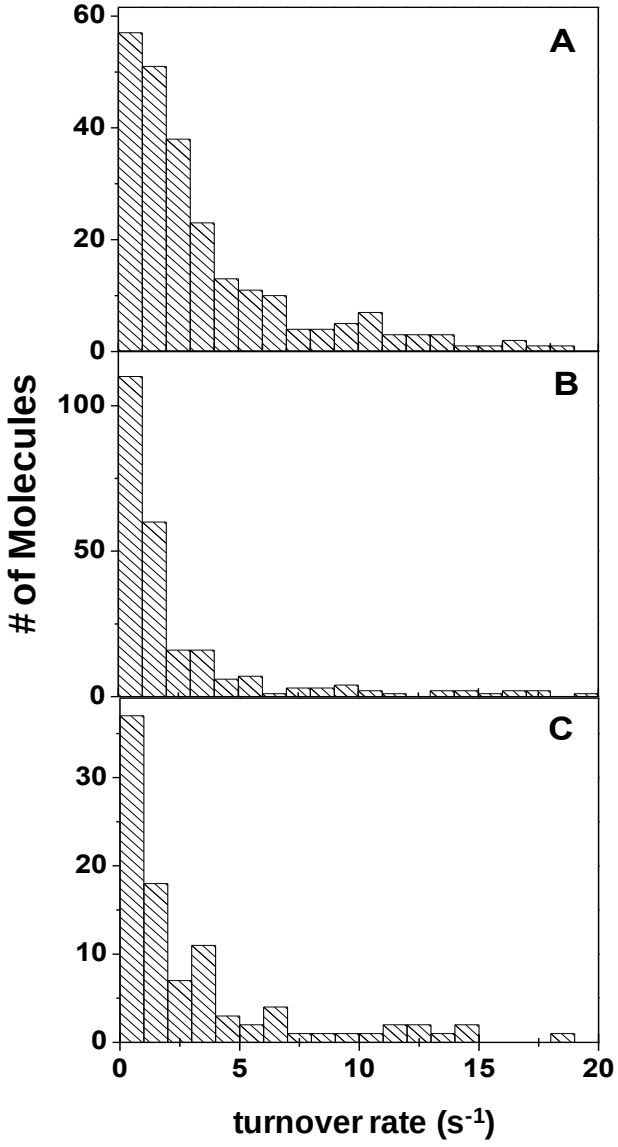

Figure 3.8 Histogram of decay constants obtained from the single exponential fit of the autocorrelation function of the fluorescence intensity trajectories of TAMRA-labeled tyrosinase immobilized on amine-coated quartz slide. (A) 1.0 mM L-tyrosine; (B) 0.01 mM L-tyrosine (C) control (no substrate).

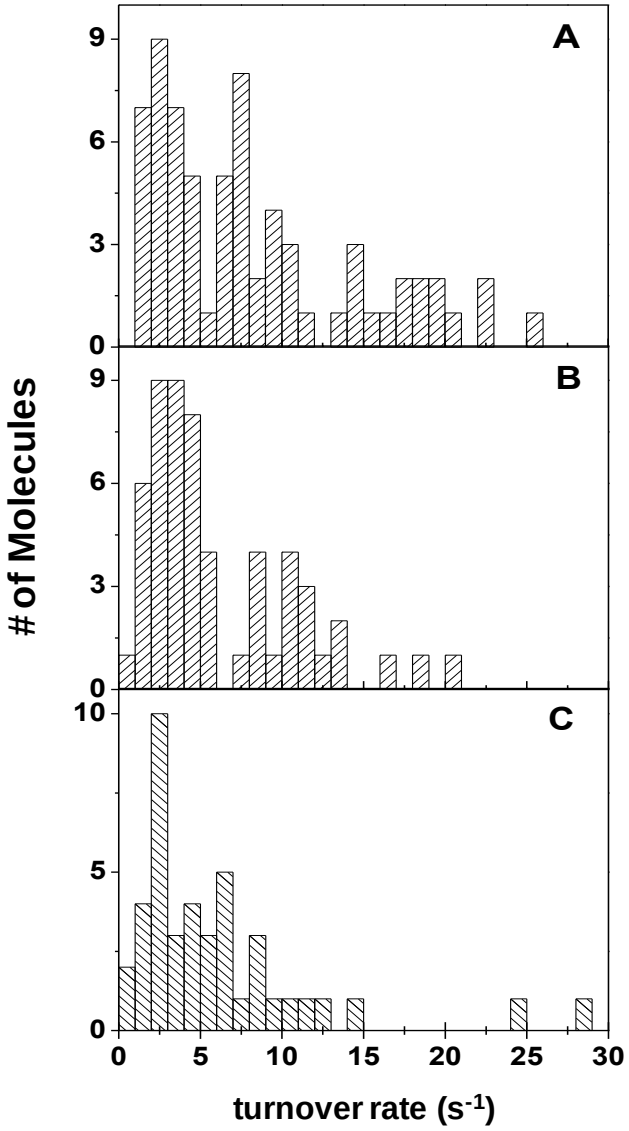

Figure 3.9 Histogram of decay constants from the autocorrelation functions of fluorescence trajectories of Cy3-labeled tyrosinase immobilized on porous nanovesicle fitted with a single exponential function. (A) 1 mM L-tyrosine (B) 0.01 mM L-tyrosine (C) control (no substrate).

3.2.5 Sm-CCFQ on tyrosinase trapped in porous nanovesicles

To eliminate possible surface effects, porous nanovesicle trapping was next used as the mode of immobilization. Possible substrate-binding inhibition and/or inactivation due to Lys residue labeling was eliminated by specifically labeling the tyrosinase at the C-terminal (D274C mutant) with Cy3. The C-terminal residue of tyrosinase is located at the back side of the enzyme, away from the active site (Figure 3.2A),[29] which ensures that labeling will not interfere with substrate binding. Single molecule experiments were done at 24^{o}C to keep the vesicles porous at all times. The sm-traces obtained from these experiments show similar behaviors to those from TAMRA-labeled tyrosinase immobilized on amine-functionalized surfaces: some show clear 2-state transitions (similar to traces in Figure 3.5) and some show large intensity fluctuations without having clear states (similar to Figure 3.7A). Both types of traces were analyzed by taking the autocorrelation function of the trace and fitting them with a single exponential function. From the time constant obtained, the individual turnover rates were calculated and the resulting histograms of these rates are shown in Figure 3.9. The histograms show that, upon addition of substrate (Figure 3.9A & B), the number of molecules that exhibit higher fluctuation rates increased compared with the control experiments (Figure 3.9C). The data also showed that, with higher substrate concentration at 1.0 mM L-tyrosine (Figure 3.9A), the number of enzyme molecules showing faster turnover rates increases compared with those from 0.01 mM L-tyrosine (Figure 3.9B). The average turnover rates, mean ± sem, are 10 ± 1 s^{-1} for 1.0 mM L-tyrosine, 8 ± 1 s^{-1} for 0.01 mM L-tyrosine, and 6.0 ± 1 s^{-1} from control experiment.

Although some differences were observed in the histogram of turnover rates between control experiments and those under catalytic conditions, the number of molecules that show this difference is few compared with the total number of

molecules that showed intensity fluctuations. The majority of the latter traces have similar rates to those obtained in control experiments. The average rate obtained from control experiments is only three times slower than the expected maximum turnover rate of the enzyme. This observation makes it more difficult to differentiate traces whose fluctuations are due to catalysis from that of the natural blinking of the dye, especially for lower substrate concentrations. As a result, the average turnover rates obtained for each substrate concentration could be heavily influenced by fluctuations not due to catalysis but rather the photophysical properties of the probe as discussed in Section 3.2.4. In addition, Cy3 is known to undergo photoinduced isomerization between its *cis*- and *trans*-isomers and this could also contribute to intensity fluctuations.

3.3 Summary and Conclusion

The development of catalysis coupled fluorescence quenching (CCFQ) method as a single molecule technique to study catalyses of transition-metal-based metalloenzymes was presented. As a first step, the single molecule enzymology of tyrosinase from *S. glaucescens* was investigated. This enzyme catalyzes the oxidation of phenols to its corresponding ortho-quinones and in the process, its Cu_2 active site goes through a cycle involving catalytic intermediates that have very different spectroscopic features: Oxy-Tyr, the active oxygenated intermediate, has strong absorption features in the visible region (~640 nm) while deoxy-Tyr, the reduced state, is spectroscopically silent. The CCFQ method capitalizes on this spectroscopic contrast by attaching a fluorescent probe near the Cu_2 center such that the intense absorption of oxy-Tyr can quench its fluorescence via an energy transfer mechanism. As a result, there will be a series of quenching and dequenching of the probe's fluorescence intensity as the enzyme goes through these two intermediates during

catalysis. By following the fluorescence intensity of each probe with single-molecule TIRF microscopy, catalytic behaviors of single metalloenzymes (i.e. tyrosinase) were investigated.

Two different immobilization methods were tested: amine coated surface and porous nanovesicle trapping. Two fluorescent probes were also used, TAMRA and Cy3, labeling them at one of the five natural Lys residues or at a C-terminal Cys residue, respectively. The fluorescent probes were successfully attached to the enzyme and the feasibility of CCFQ from ensemble fluorescence quenching experiment was tested. Single molecule experiments were done with TIRF microscopy and the fluorescence intensity of each probe was extracted out for analysis before it photobleaches. The single molecule results were analyzed by a thresholding method and by fluorescence intensity autocorrelation analysis.

Results obtained from tyrosinase immobilized on amine-functionalized surfaces did not show any difference between control experiments (without adding the substrate L-tyrosine into the flow cell) and those obtained under catalytic conditions (in the presence of 0.01 mM and 1.0 mM L-tyrosine). On the other hand, results from single molecule experiments done on tyrosinase trapped in porous nanovesicles showed some difference between control and catalytic conditions. That is, with increasing substrate concentration, the number of molecules that showed an increase in turnover rates also increased. However, since majority of the traces behaved very similar to those obtained from control experiments, whose "turnover rates" are only ~3X slower than that obtained from catalysis, it was difficult to extract out any physical information pertaining only to catalysis that is not heavily influenced by the natural blinking of the probe in the absence of catalysis.

Since the intrinsic blinking of the single molecule probes has so much effect on the kinetic analysis of enzyme catalysis, a non-blinking fluorescent probe would be

ideal to use for CCFQ. All organic dyes that are currently used in single molecule experiments, as well as fluorescent quantum dots, have this blinking problem. A lot of efforts have been put into minimizing the occurrence of these "dark/dim states". The methods that are available presently (addition of BME or Trolox) are not compatible with studying tyrosinase single-molecule enzymology. Recently, a nonblinking quantum dot (CdZnSe/ZnSe) with a fluorescent spectrum that overlaps with the absorption spectrum of oxy-Tyr has been synthesized.[47] This quantum dot could be a good probe for CCFQ single-molecule enzymology of tyrosinase since the control experiment will no longer complicate the kinetic analysis of the catalysis. Also, since quantum dots have exceptionally long photobleaching lifetimes, it should be possible to observe the catalytic behavior of each molecule over a much longer period of time than is possible with organic dyes. This long observation window would then allow the probing of dynamic fluctuations of the catalytic rate gaining insights into enzyme dynamics of longer timescales and directly test the phenomenon of dynamics-coupled catalysis of metalloenzymes.

3.4 Materials and Methods

3.4.1 Protein labeling and purification

Tyrosinase from *Streptomyces glaucescens* (Sg) was obtained as a purified 30 kDa monomer from our collaborator (Prof. Timothy Machonkin at Whitman College, Washington). The protein stock in Buffer A (10 mM Tris pH 8.5 with 20% glycerol, 50 mM NaCl, and 100 μM $CuCl_2$), was first buffer exchanged by running through a desalting column, Sephadex G-25 Superfine (GE Healthcare Life Sciences), with 25 mM phosphate buffer pH 8.5 containing 50 mM NaCl and 100mM $CuCl_2$. Tetramethylrhodamine succinimidyl ester (TAMRA-SE) (Invitrogen) was used as the probe targeting one of the five surface exposed Lys residues on the protein. TAMRA-

SE was added to tyrosinase solution, 10:1, allowing the reaction to run overnight at 4^oC with gentle shaking. The labeling reaction was quenched by adding excess NH_2OH (J. T. Baker), incubating for an hour to ensure quenching of all unreacted dye. The labeled protein was then purified from the excess dye by running through the desalting column using Buffer A. The labeling efficiency was calculated from concentrations of both tyrosinase, using BCA (bicinchoninic acid) protein assay, and TAMRA from the absorption spectrum of the purified dye-labeled enzyme using ε_{555} = 65,000 M^{-1}-cm^{-1}.

Site-specific labeling of the C-terminal of tyrosinase was also done by mutating the C-terminal Asp to a Cys residue (Dr. Cynthia Kirkland, Protein Facilities, Dept. of Chemistry & Chemical Biology, Cornell University). The mutant Tyr was expressed in B*R2(Chl^R) cells. Cells were lysed via freeze/thaw cycles, and proteins were purified from the lysate via anion exchange (HiLoad 26/10 Q Sepharose HP and Mono Q 10-100 GL), and gel filtration (HiLoad 26/60 Superdex 200 prep grade) chromatography using an FPLC system (GE Life Sciences). The protein's purity was determined by SDS-PAGE and confirmed by mass spectrometry of the trypsin digest of the protein. The protein was stored in 20 mM Tris, pH 7.5, 150 mM NaCl, 2 mM DTT, 100mM $CuCl_2$ in 20% Glycerol. The C-terminal Cys of the mutant tyrosinase was labeled with Cy3-maleimide (Amersham Biosciences) by mixing a 10:1 ratio of Cy3 and tyrosinase, respectively. The labeling reaction mixture was incubated at 4^oC overnight with gentle shaking before it was quenched with excess β-mercaptoethanol (BME) for 60 min, also at 4^oC. The labeled tyrosinase was then purified from excess dye by running through the desalting column using Buffer A and the labeling efficiency calculated using ε_{550} = 140,000 M^{-1}-cm^{-1} for Cy3.

3.4.2 Ensemble fluorescence and activity assay

Quenching of the probe upon formation of oxy-Tyr at the ensemble level was

first measured prior to single molecule CCFQ studies (See Section 3.2.1). The "resting" form of the enzyme, which is mostly met-Tyr, was first converted to its deoxy-state by treating the labeled enzyme with excess NH_2OH under N_2 atmosphere.[30] The fluorescence spectrum of the resulting solution was then obtained using a Cary Eclipse fluorescence spectrophotometer (Varian). The fluorescence spectrum of the oxy-Tyr was obtained from the same solution after exposure to air (24).[31] Quenching was confirmed by comparing the two spectra after correcting for dilution.

To check for the viability of the dye-labeled tyrosinase (wild type and C-terminal mutant), an enzymatic assay using L-dihydroxy phenylalanine (L-DOPA) as substrate was carried out.[35] 18 mM L-DOPA was prepared in 0.1 M phosphate buffer pH 6.8. The substrate solution was incubated at 25^{o}C before 1 μL of 70uM tyrosinase was added to 1.0 mL 18mM L-DOPA. The generation of the product, L-DOPA-quinone, was monitored by its absorbance at ~475 nm (ε = 3600 M^{-1} cm^{-1}) for 90 s at 1.5 s interval using a UV-Vis spectrophotometer.

3.4.3 Immobilization for single-molecule experiment

I tried two immobilization methods commonly used in single molecule experiment: (1) direct immobilization on amine coated quartz slide and (2) porous nanovesicle trapping. [38,39]

For direct immobilization on an amine coated surface, an aminoalkylsiloxane reagent, Vectabond (Vector Laboratories), was used as the silanizing agent to functionalize slides with amine. Freshly prepared 2% vectabond solution in acetone was added quickly to a clean quartz slide. The silane solution was allowed to dry for 10 mins before washing extensively with nanopure water. N_2 was used to dry the slide before assembling the flow cell, in which the protein molecules are immobilized for

single molecule experiments. The flow cell consists of a flow channel made from a quartz slide (Technical Glass) and a borosilicate coverslip (Gold Seal) glued by a double-sided adhesive tape. Immobilization of tyrosinase on the amine-functionalized slide surface was accomplished by flowing a 300 μL 20 nM of dye-labeled tyrosinase solution and incubating for 10 min. Unbound tyrosinase was washed out with Buffer A.

An ensemble L-DOPA activity assay was carried out prior to single molecule experiments to check the activity of tyrosinase immobilized on amine-functionalized quartz surfaces. A small glass container (~ 5 mL) was first amine functionalized with vectabond. After thorough washing of this container with nanopure water, 100 μL of 70 μM tyrosinase stock solution was immobilized. Excess enzyme was washed away with buffer before 18 mM L-DOPA solution was added. The absorbance at 475 nm was monitored for 90s at 1.5 s interval. For all experiments using amine-functionalized slide for immobilization, TAMRA-labeled tyrosinase was used.

Porous nanovesicle trapping was utilized to immobilize C-terminal Cy3-labeled tyrosinase and monitor its catalysis over time. A mixture of dimyristoyl phospatidylcholine (DMPC) and 1% 1,2-dipalmitoyl*sn*-glycero3-phosphoethanolamine-N-(cap biotinyl) (16:0 biotinyl cap PE) (Avanti Lipids) was dissolved in chloroform and dried under a constant flow of nitrogen. The lipid film was hydrated with 0.5 □M Cy3-labeled tyrosinase in Buffer A for 2 hours with occasional mixing. The concentration of the protein was kept low enough such that average number of dye-labeled tyrosinase trapped inside the vesicles is less than one per vesicle. The solution was repeatedly extruded, at least 33 times or until the solution becomes transparent, through a polycarbonate membrane with 100 nm pores (Avanti Mini Extruder) to form ~100-nm diameter protein-encapsulating unilamellar vesicles. Loaded vesicles were used for single-molecule experiments immediately

after preparation or within 48 hours of preparation. The vesicles were immobilized via biotin-streptavidin (Molecular Probes) linkages. The slides were first amine-functionalized (Vectabond, VectorLaboratories) and then coated with PEG polymers, 1% of which contains biotin (100 mg/mL m-PEG-SPA-5000 and 1 mg/mL biotin-PEG-NHS-3400 (Nektar Therapeutics)). 300 μL of streptavidin at a concentration of 0.2 mg/mL was then flowed in and incubated for 10 minutes. Unbound streptavidin was washed out with buffer containing 0.1 mg/mL BSA, which helps to block nonspecific binding sites. Protein-loaded vesicles were flowed in at a total Cy3-tyrosinase concentration of 20 pM and incubated for 10 min before unbound vesicles were washed out with Buffer A. To keep the nanovesicles porous, the temperature of the flow cell and the objective was maintained at 24^{o}C using a stage warmer. [33] All solutions were also incubated at 24^{o}C water bath prior to use.

The porosity of the nanovesicles to small molecules and their ability to trap large ones was tested using smFRET measurements on a Holliday junction's structural interconversion in the presence of divalent metal ions (Chapter 2).[40] The DMPC lipid film was hydrated with 1 μM HJC2a (labeled with Cy3 and Cy5) solution containing 2mM $MgCl_2$ and 10 mM NaCl in 10 mM Tris buffer pH 7.35. The single-molecule fluorescence intensities of both dyes were monitored in the presence of the divalent ion. To wash out Mg^{2+}, 10 mM Tris buffer without salt was flowed in before another set of movies to monitor fluorescence intensities of Cy3 and Cy5 was taken. Lastly, both $MgCl_2$ and NaCl were re-introduced into the chamber, after which another set of movies were taken. From the intensities of both Cy3 and Cy5, E_{FRET} was calculated for all three conditions.

3.4.4 Single-molecule fluorescence experiments and data analysis

Single-molecule fluorescence measurements were performed on a homebuilt prism-type total internal reflection microscope based on an Olympus IX71 inverted microscope. A continuous wave circularly polarized 532 nm laser beam (CrystaLaser, GCL-025-L-0.5%) of 1-5 mW was focused onto an area of ~150 × 75 μm^2 on the sample to directly excite the probe. The fluorescence of Cy3/TAMRA was collected by a 60X NA1.2 water-immersion objective (UPLSAPO60XW, Olympus), filtered to reject the excitation laser light (HQ550LP, Chroma Technology Corp.), and projected onto the camera (Andor iXon EMCCD, DV887DCS-BV), controlled by an Andor IQ software. The time resolution was 30 ms/frame for tyrosinase immobilized on amine-functionalized surfaces and 10 ms/frame for those trapped inside porous nanovesicles. A home-written IDL program was used to extract individual fluorescence intensity trajectories of Cy3 from the movies. To obtain the turnover rate for each enzyme, autocorrelation analysis was done on individual intensity trajectories.[12,43] For traces that show clear two-state transitions, "thresholding" analysis was also performed.[40,41]

Prior to catalysis, the immobilized enzymes were incubated with excess NH_2OH in Buffer A to convert all met-Tyr (resting form of the enzyme) to deoxy-Tyr for subsequent binding of O_2. Catalysis was initiated by flowing in the substrate solution (0.01 mM and 1.0 mM L-tyrosine). In the control experiments, the fluorescence intensity of the probe was monitored in the absence of L-tyrosine.

REFERENCES

(1) Antikainen, N. M.; Smiley, R. D.; Benkovic, S. J.; Hammes, G. G. *Biochemistry* **2005**, *44*, 16835-16843.

(2) Brender, J. R.; Dertouzos, J.; Ballou, D. P.; Massey, V.; Palfey, B. A.; Entsch, B.; Steel, D. G.; Gafni, A. *J. Am. Chem. Soc.* **2005**, *127*, 18171-18178

(3) Chen, Y.; Hu, D.; Vorpagel, E. R.; Lu, H. P. *J. Phys. Chem. B* **2003**, *107*, 7947-7956.

(4) Edman, L., FiSldes-Papp, Z., Wennmalm, S. & Rigler, R. *Chem. Phys.* **1999**, *247*, 11-22

(5) Edman, L.; Rigler, R. *Proc. Natl. Acad. Sci. USA* **2000**, *97*, 8266-8271.

(6) English, B. P.; Min, W.; van Oijen, A. M.; Lee, K. T.; Luo, G.; Sun, Y.; Cherayil, B. J.; Kou, S. C.; Xie, X. S. *Nat. Chem. Biol.* **2005**, *2*, 87 - 94

(7) Flomenbom, O.; Velonia, K.; Loos, D.; Masuo, S.; Cotlet, M.; Engelborghs, Y.; Hofkens, J.; Rowan, A. E.; Nolte, R. J. M.; van der Auweraer, M.; de Schryver, F. C.; Klafter, J. *Proc. Natl. Acad. Sci. USA* **2005**, *102*, 2368-2372

(8) Funatsu, T.; Harada, Y.; Tokunaga, M.; Saito, K.; Yanagida, T. *Nature* **1995**, *374*, 555-559.

(9) Ha, T.; Ting, A. Y.; Liang, J.; Caldwell, W. B.; Deniz, A. A.; Chemla, D. S.; Schultz, P. G.; Weiss, S. *Proc. Natl. Acad. Sci. USA* **1999**, *96*, 893-898.

(10) Kuznetsova, S.; Zauner, G.; Aartsma, T.; Engelkamp, H.; Hatzakis, N.; Rowan, A.; Nolte, R.; Christianen, P.; Canters, G. *Proc. Natl. Acad. Sci. USA* **2008**, *105*, 3250-3255.

(11) Levene, M. J.; Korlach, J.; Turner, S. W.; Foquet, M.; Craighead, H. G.; Webb, W. W. *Science* **2003**, *299*, 682-686.

(12) Lu, H. P.; Xun, L. Y.; Xie, X. S. *Science* **1998**, *282* 1877-1882

(13) Myong, S.; Rasnik, I.; Joo1, C.; Lohman, T. M.; Ha, T. *Nature* **2005**, *437*, 1321-1325.

(14) Paige, M.; Fromm, D. P.; Moerner, W. E. *Proc. Soc. Photo Opt. Instrum. Engr.* **2002**, *4634*, 92-103

(15) Rajagopalan, P. T. R.; Zhang, Z.; McCourt, L.; Dwyer, M.; Benkovic, S. J.; Hammes, G. G. *Proc. Natl. Acad. Sci. USA* **2002**, *99* 13481-13486.

(16) Velonia, K.; Flomenbom, O.; Loos, D.; Masuo, S.; Cotlet, M.; Engelborghs, Y.; Hofkens, J.; Rowan, A. E.; Klafter, J.; Nolte, R. J. M.; de Schryver, F. C. *Angew. Chem., Int. Ed.* **2005**, *44*, 560-564

(17) Yasuda, R.; Noji, H.; Yoshida, M.; Kinosita, K. J.; Itoh, H. *Nature* **2001**, *410* 898-904

(18) Zhang, Z.; Rajagopalan, P. T. R.; Selzer, T.; Benkovic, S. J.; Hammes, G. G. *Proc. Natl. Acad. Sci. USA* **2004**, *101*, 2764-2769.

(19) Austin, R. H.; Beeson, K. W.; Eisentein, L.; Frauenfielder, H.; Gunsalus, I. C. *Biochemistry* **1975**, *14*, 5355-5373.

(20) Min, W.; English, B.; Luo, G.; Cherayil, B.; Kou, S. C.; Xie, X. S. *Acc. Chem. Res.* **2005**, *38*, 923-931.

(21) Chen, P., Andoy, N. M. In *Comprehensive Natural Products Chemistry II: Chemistry and Biology* Mander, L., Lui, H.-W., Ed.; Elsevier: Oxford: 2010; Vol. Vol. 9, p 751.

(22) Chen, P.; Andoy, N. M. *Inorg. Chim. Acta* **2008**, *361*, 809-819.

(23) Erker, W.; Schoen, A.; Basche, T.; Decker, H. *Biochem. Biophys. Res. Commun.* **2004**, *324*, 893-900.

(24) Erker, W.; Sdorra, S.; Basche, T. *J. Am. Chem. Soc.* **2005**, *127*, 14532-14533

(25) Schmauder, R.; Librizzi, F.; Canters, G.; Schmidt, T.; Aartsma, T. *ChemPhysChem* **2005**, *6*, 1381-1386

(26) Holm, R.; Kennepohl, P.; Solomon, E. I. *Chem. Rev.* **1996**, *96*, 2239-2314.

(27) Lever, A. B. P. *Inorganic electronic spectroscopy* Elsevier Science Amsterdam, The Netherlands, 1984.

(28) Decker, H.; Dillenger, R.; Tuczek, F. *Angew. Chem. Int. Ed.* **2000**, *39*, 1591-1595.

(29) Matoba, Y.; Kumagai, T.; Yamamoto, A.; Yoshitsu, H.; Sugiyama, M. *J. Biol. Chem.* **2006**, *281*, 8981-8990.

(30) Yamazaki, S.; Itoh, S. *J. Am. Chem. Soc.* **2003**, *125*, 13034-13035.

(31) Solomon, E. I.; Sundaram, U. M.; Machonkin, T. E. *Chem. Rev.* **1996**, *96*, 2563-2605.

(32) Haugland, R. P.; Corp., I., Ed. 2005.

(33) Malicka, J.; Gryczynski, I.; Fang, J. Y.; Kusba, J.; Lakowicz, J. R. *J. Fluor.* **2002**, *12*, 439-447.

(34) Lacowicz, J. R. *Principles of fluorescence spectroscopy*; Kluwer/Plenum: New York, 1999.

(35) Duckworth, H. W.; Coleman, J. E. *J. Biol. Chem.* **1970**, *245:*, 1613-1625.

(36) Huber, M.; Hintermann, G.; Lerch, K. *Biochemistry* **1985**, *24*, 6038-6044.

(37) Benitez, J.; Keller, A. M.; Chen, P. *Method. Enzymol.* **2010**, *472*, 41-60.

(38) Cisse, I.; Okumus, B.; Joo, C.; Ha, T. *Proc. Natl. Acad. Sci. USA* **2007**, *104*, 12646-12650

(39) Monnard, P. A. *J. Membr. Biol.* **1996**, *191*, 87–97.

(40) Andoy, N. M.; Sarkar, S. K.; Wang, Q.; Panda, D.; Benitez, J. J.; Kalininskiy, A.; Chen, P. *Biophys. J.* **2009**, *97*, 844-852

(41) McKinney, S. A.; Declais, A. C.; Lilley, D. M. J.; Ha, T. *Nat. Struct. Biol.* **2003**, *10*, 93-97.

(42) Garcia-Molina, F.; Penalver, M. J.; Fenoll, L. G.; Rodriguez-Lopez, J. N.; Varon, R.; Garcia-Canovas, F.; Tudela, J. *J. Mol. Catal. B* **2005**, *32*, 185-192.

(43) Xu, W.; Kong, J. S.; Yeh, Y.-T. E.; Chen, P. *Nat. Mater.* **2008**, *7*, 992-996.

(44) Weston, K. D.; Carson, P. J.; Metiu, H.; Buratto, S. K. *J. Chem. Phys.* **1998**, *109*, 7474-7485.

(45) Bagshaw, C. R., Conibear, P. B. *Single Mols.* **2000**, *1*, 271-277.

(46) Bagshaw, C. R.; Cherny, D. *Biochem. Soc. Trans.* **2006**, *34*, 979-982.

(47) Wang, X.; Ren, X.; Kahen, K.; Hahn, M.; Rajeswaran, M.; Maccagnano-Zacher, S.; Silcox, J.; Cragg, G.; Efros, A.; Krauss, T. *Nature* **2009**, *450*, 686-689.

CHAPTER FOUR

SUPERRESOLUTION OPTICAL IMAGING OF CATALYSIS ON SINGLE GOLD NANOPARTICLES

4.1 Introduction

Metal nanoparticles have been used as catalysts for chemical transformations ranging from organic synthesis to energy conversion.[1-4] Owing to their nanometer sizes, many of their atoms are located on the surface, making their surface-to-volume ratio significantly larger than that of bulk materials. This high surface to volume ratio gives nanoparticles novel and sometimes new properties in catalysis. Materials that exhibit very limited reactivity on the bulk scale can be catalytically active in nanoscale clusters.[2,5-7] This property makes nanoparticles a cost-effective alternative to bulk materials and therefore highly attractive for catalysis. It is therefore important to understand the fundamental principles governing their catalytic properties in order to improve current nanoparticle catalysts and to have better control in designing new ones.

Extensive work has been done in trying to characterize the catalytic properties of nanoparticles at the ensemble level.[2,4,6-8] From these studies, significant insights were obtained in correlating a nanoparticle's catalytic property to its structure. For instance, it has been demonstrated that variations in size, shape and crystal structure can lead to different catalytic activities. Shapes with more corner and edge atoms are shown to have higher reactivity than those with fewer corner and edge atoms.[4,5,8] However, the intrinsically inhomogeneous catalytic properties arising from the structural dispersion in a population of nanoparticles still remains a challenge to the fundamental understanding of nanocatalysis. Even for a single nanoparticle, a distribution of atoms on facets, edges, and corners are observed on its surface,[4]

making ensemble-averaged characterizations inadequate for directly correlating structure to the different catalytic properties of the individual particles.

Recent developments in single-molecule fluorescence microscopy have enabled the study of catalysis of individual nanocatalysts.[9-12] With single turnover resolution on each nanoparticle, it has been shown that inhomogeneous reactivity is still observed even when nanoparticles have a monodisperse size distribution and composition. Also, the catalytic rate of a single nanoparticle fluctuates with time as a result of surface restructuring.[11] However, no direct correlation between the differences in activity and the structure of individual nanoparticles was reported, due to the low spatial resolution of optical microscopy. Transmission electron microscopy (TEM) and scanning electron microscopy (SEM) can characterize nanoparticle structure with very high resolution (down to atomic resolution for TEM) but cannot monitor catalytic reactions *in situ*.[4,13-19] Thus, there is a need to combine high temporal resolution single-molecule fluorescence imaging with high spatial resolution electron microscopy, to enable direct correlation of activity and structure.

Here I present a combination of super-resolution (SR) optical fluorescence imaging of single nanoparticle catalysis and SEM to directly correlate the structure and catalytic properties of gold nanoparticles. SR optical imaging techniques, such as stochastic optical reconstruction microscopy (STORM) and photoactivation localization microscopy (PALM), can spatially resolve and accurately localize the positions of individual fluorescent molecules that reside in areas smaller than the diffraction limit.[20-22] Using these methods, I was able to localize, within a few nanometers, the locations of the fluorescent product molecules generated catalytically *in situ* on a single nanocatalyst.[10] The morphology of the same set of nanoparticles was obtained from SEM imaging. Combining these two imaging techniques I was able to directly correlate the catalytic properties of the nanoparticle with its structure and

differentiate the reactivity of different type of surface atoms (e.g. corners and edges). This direct structure-activity correlation of nanoparticle catalysts down to the single-particle level can provide unprecedented insights into the fundamental principles of nanocatalysis.

4.2 Results and Discussion

4.2.1 Methodology: mapping of catalytic sites on single nanoparticles

Nanoparticle catalysts have sizes comparable to or smaller than the diffraction limit of optical microscopes (a few hundred nanometers). *In situ* optical mapping of the active sites (where the product is generated) on the nanoparticle surface will therefore requires accurate localization beyond the diffraction limit. Recently, SR imaging methods based on single-molecule fluorescence detection, such as STORM and PALM, have made it possible to achieve high spatial (~20 nm) and temporal resolution (a few milliseconds to seconds) of immobilized fluorescent molecules with optical microscopy.[20-22] These methods utilize two features of single molecule fluorescence detection to achieve spatial resolution with an order of magnitude higher than the diffraction limit. The first is the nanometer-accurate localization of single fluorophores achieved by fitting the point spread function (PSF) of the fluorescence of the molecule with a Gaussian distribution.[23] This highly precise localization method has been used to track single fluorophores in studying biological systems, as well as to monitor diffusion in mesoporous materials.[23-26] The other is temporal separation of the fluorescence detection of emitters located within a diffraction-limited area. In PALM and STORM, this separation is achieved through photoinduced temporal switching of very few fluorescent molecules in such a way that the emissive ones do not reside in a diffraction-limited spot.[20-22] In single nanoparticle catalysis, since successive catalytic reactions often do not occur at the same time, the fluorescence signal coming from the

catalyzed fluorogenic reactions are naturally time separated and can therefore be localized with high accuracy using SR-imaging techniques. Very recently, SR-imaging has been used to visualize catalytic reactivity on single-walled carbon nanotubes[10] and micrometer-sized zeolite crystals.[27]

Our approach to spatially resolve catalysis on the surface of a single nanoparticle is illustrated in Figure 4.1. The nanoparticle catalyst, similar to the gold nanoprism depicted in Figure 4.1A (not drawn to scale), catalyzes a fluorogenic reaction where a non-fluorescent reactant is transformed to a fluorescent product. This fluorogenic reaction is the gold nanoparticle-catalyzed reduction of resazurin to resorufin by NH_2OH whose oxidation product is probably nitrite (NO_2^-) or related products.[9,11] Movies of these events were taken and analysis of these movies gives, for each nanoparticle, a fluorescence intensity trajectory similar to Figure 4.1B with the characteristic digital on (high intensity) and off (low intensity) behavior. Each sudden fluorescence increase comes from a product formation, and the amount of time the product molecule stays on the nanoparticle surface is the on-time (τ_{on}). When the product dissociates, a sudden intensity decrease is observed, generating an off-state, and τ_{off} is the time it takes for another product to form on the nanoparticle surface.[11] Each τ_{on} is comprised of a series of images of the fluorescence coming from a product molecule on the surface of the nanoparticle (Figure 4.1B inset). All images within a single on-time can be added and point spread function fitting can be used to determine the location of the product molecules with nanometer accuracy (Figure 4.1C).[10] Doing these localizations one at a time for all the product molecules generated on the surface of the nanoparticle would give the precise locations of where these resorufin molecules are generated (Figure 4.1C inset). The reconstructed image of these localizations gives the SR optical image of nanoparticle catalysis. Overlaying this SR image with the SEM image of the nanoparticle will then map the catalytic sites on the

nanoparticle surface (Figure 4.1D). With this coupled *in situ* SR-optical and SEM imaging, differences in the catalytic properties of individual nanoparticles can now be directly correlated to their structure. Also, reactivity differences at different locations (i.e. corners, edge, and flat surface) on the same nanoparticle can now be directly obtained.

Here I use this correlated SR-imaging and SEM of single-nanoparticle catalysis to spatially resolve catalytic reactions on the surface of nanoparticles with different shapes and sizes. Since nanoparticles' shape and crystal structure have been shown to affect their catalytic rates, the combined imaging methodology can provide direct link between their structure and catalytic properties.

4.2.2 Catalysis on Gold Nanoprisms

4.2.2.1 Synthesis, structure characterization, and ensemble activity assay

Gold nanoprisms were synthesized by reducing $AuCl_4^-$ with extract from lemon grass.[28] This biosynthetic method generated a variety of nanoprisms (triangles, pentagons, and hexagons), with a wide range of edge lengths, as well as spherical nanoparticles (Figures 4.2A, B). (For the rest of the chapter "gold nanoprisms" and "spherical nanoparticles" are used to refer to each of the components, while "bio-synthesized nanoparticles" is used to refer to the mixture.) The distribution of the nanoprism's edge lengths, ranging from a few tens to a few hundreds of nanometers, and the distribution of the diameter of spherical nanoparticles (average ~55 nm), are plotted in Figure 4.2C and Figure 4.2D, respectively. The absorption spectrum of the solution containing these bio-synthesized nanoparticles is shown in Figure 4.2E. The peak at ~550 nm primarily results from the localized surface plasmon resonance

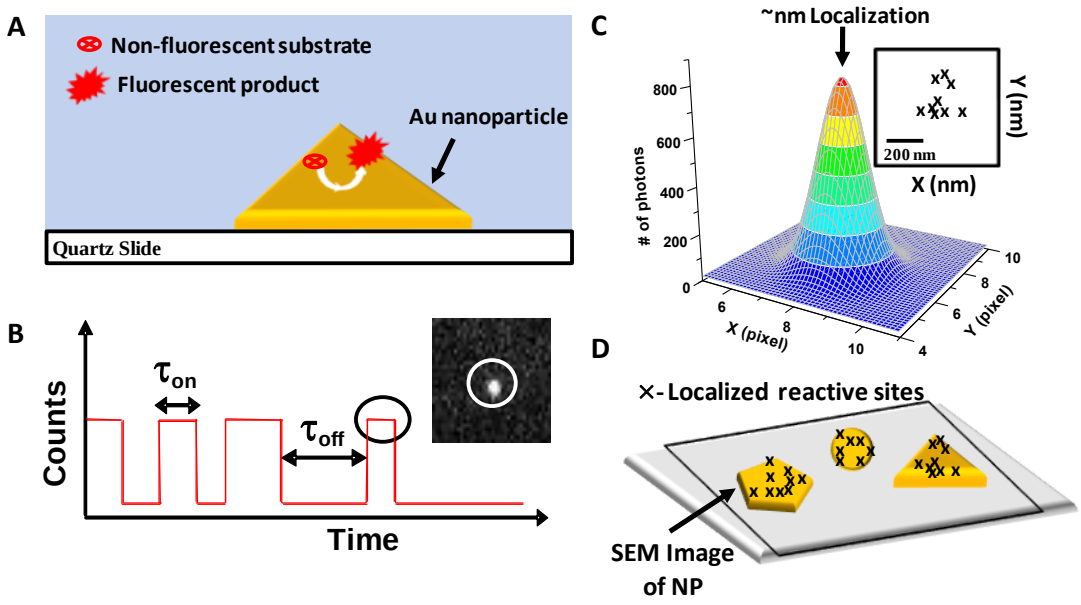

Figure 4.1 Direct correlation of SR optical imaging with SEM images of NP. (A) Scheme of NP (a triangular nanoprism here) as it catalyzes a fluorogenic reaction where a non-fluorescent reactant is transformed to a fluorescent product. Fluorescence excitation is via the evanescent wave of total internal reflection laser excitation geometry (green background). (B) Idealized fluorescence intensity versus time trajectory for single-nanoparticle catalysis. Inset: a representative conventional wide-field fluorescence image of a single-particle catalysis during an on-time. (C) Gaussian fit of the point spread function (PSF) of the fluorescent spot in C inset. The center of the PSF gives a nanometer-accuracy determination of the location of the fluorescent molecule. Inset: schematic scatter plot of the localizations from many fluorescent product molecules. (D) Schematic of overlaying the product molecule locations obtained from SR imaging and a high resolution structural image (e.g. SEM) of the nanoparticle.

(LSPR) of the spherical nanoparticles. The broad feature at >800 nm is due to the LSPR of nanoprism; its large width comes from the wide distribution of edge lengths of nanoprisms.[17,18,28,29]

The catalytic activity of the bio-synthesized nanoparticles towards the reduction of resazurin to resorufin was tested at the ensemble level before single molecule experiments were performed. The *in situ* absorption spectrum of the catalytic conversion of resazurin to resorufin by NH_2OH is shown in Figure 4.3A. The activity of the bio-synthesized nanoparticles towards this reaction is shown by the disappearance of the resazurin absorption at ~602 nm and the concurrent appearance of the resorufin absorption at ~568 nm. Figure 4.3B shows the substrate concentration dependence of the initial reaction rate, which shows a saturation behavior similar to what was observed for a 6 nm spherical gold nanoparticles.[11] The data were fitted with the Langmuir-Hinshelwood rate equation:[11,30,31]

$$r = \frac{k_{eff} K[NP][S]}{1 + K[\mathrm{S}]} = \frac{V_{\max f} K[S]}{1 + K[\mathrm{S}]} \qquad \text{Equation 4.1}$$

where r is the observed rate of reaction, [NP] is the naoparticle concentration, [S] is the substrate concentration, k_{eff} is the effective rate constant per particle (rate constant per active site × total number of the active sites in one particle), $V_{\max}$ is the maximum reaction rate, and K is the substrate adsorption equilibrium constant. The fit gives an adsorption equilibrium constant of $K = 0.21 \pm 0.06\ \mu M^{-1}$ and maximum rate $V_{\max} = 1.2 \pm 0.1$ nM-s^{-1}. These constants include contributions from both the spherical nanoparticles and nanoprisms, assuming both are catalytically active, since I could not completely purify the resulting mixture. However, with the coupled SR-optical and SEM imaging, the reactivity of these two types of nanoparticles can be differentiated, as described below.

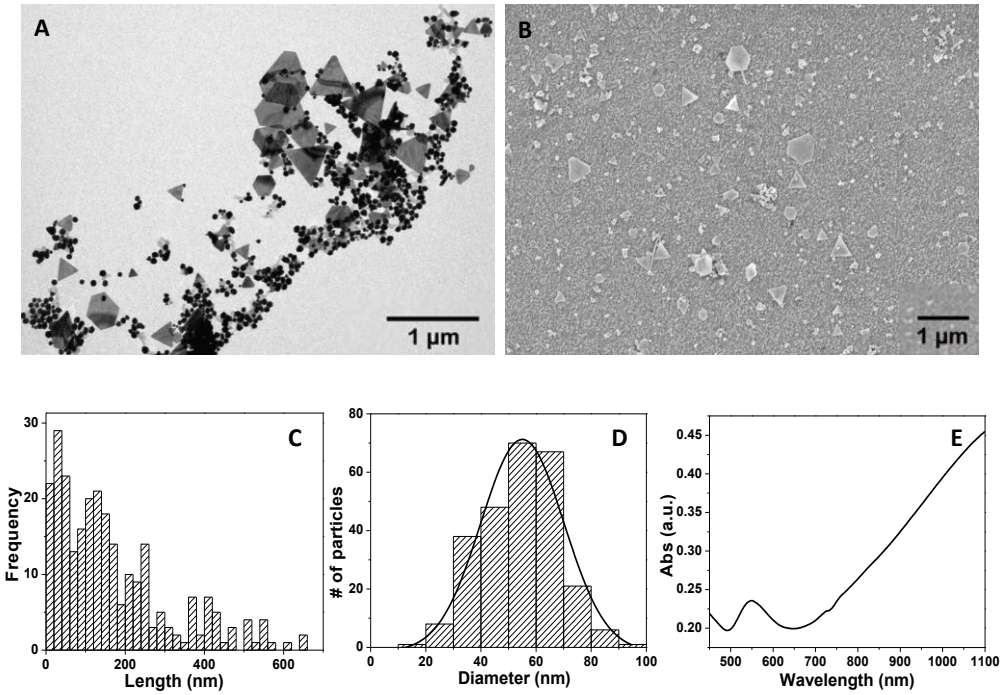

Figure 4.2 (A) TEM and (B) SEM images of bio-synthesized nanoparticles. (C) Edge length distribution of the nanoprisms. (D) Size distribution of the pseudo-spherical nanoparticles. (E) Absorption spectrum of the nanoparticle solution.

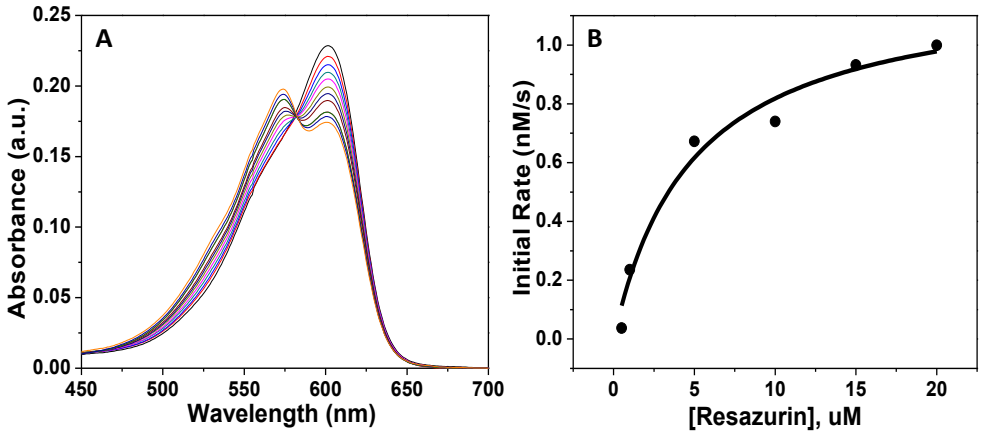

Figure 4.3 Ensemble measurements of catalytic activity. (A) *In situ* absorption measurements of resazurin reduction to resorufin by NH_2OH, catalyzed by gold nanoprism in aqeous solution: $[\text{resazurin}]_o = 5$ μM; $[NH_2OH]_o = 1.0$ mM. (B) Substrate concentration dependence of the catalytic rate of resazurin reduction where the solid line is the Langmuir-Hinshelwood rate equation fit with maximum rate $V_{max} = 1.2 \pm 0.1$ nM-s^{-1} and substrate adsorption equilibrium constant $K = 0.21 \pm 0.06$ μM^{-1}.

4.2.2.2 Correlation of optical image and SEM image of nanoparticles

In order to map the locations where product molecules are generated (obtained from SR-imaging analysis) onto a nanoparticle's SEM image, I first verified if direct overlaying of optical images and SEM images was feasible. To this end, markers etched on the surface of the quartz slide were used as guides for imaging the same area on the sample for both SEM and optical measurements (See Section 4.4.3). Figure 4.4 demonstrates how to locate and correlate the same nanoparticles via the two imaging methods. Figure 4.4A shows the negative fluorescence image (particles appear as black dots and the background is white/bright) of the bio-synthesized nanoparticles immobilized in the vicinity of marker "4.1", also faintly visible due to the small amount of scattered light that passed through the filter. The marker is clearer in the scattered-light image (data not shown), obtained when the optical filter used to block the excitation laser is removed.

To investigate whether the fluorescence observed in Figure 4.4A is coming from gold nanoparticles, the same marker was located in SEM imaging. Figure 4.4B is the SEM image of the area shown in panel A (boxed area). The image shows that the three fluorescent spots observed in panel A (inside oval) are individual nanoparticles immobilized near marker "4". This image correlation clearly shows that the bio-synthesized nanoparticles, both prism and spherical ones, are emissive and that their emission is visible as diffraction-limited spots in the single nanoparticle catalysis experiments. This image also demonstrates that optical images from single-molecule experiments can be correlated with those taken by SEM, which can directly visualize the nanoparticle morphology and structure.

The origin of the emission of the bio-synthesized gold nanoparticles (as well as the emission of the citrate reduced 40- and 60-nm gold nanoparticles as will be shown

later, Section 4.2.3) has not been studied in detail.[32-34] Previous works have reported photoluminescence from nanosize gold clusters with diameters less than 5 nm but not for bigger particles.[35] The photoluminescence in small particles was assigned to the radiative recombination of Fermi level electrons and *sp*- and *d*-band holes created after photoexcitation. For larger nanoparticles, only the origin of luminescence from gold nanorods with different aspect ratio (i.e., different length; width of 20 nm) has been studied.[32,36] The source of this emission is believed to be electron and hole interband recombination enhanced via coupling to the surface plasmon resonance. Excitation of the gold nanorods leads to excitation of the surface plasmon coherent electronic motion as well as the d-electrons. Relaxation of these electronic motions followed by the recombination of the sp-electrons with holes in the d-band is believed to lead to the observed emission. However, for both the pseudo-spherical nanoparticles and nanoprisms studied, the origin of their emission is not yet well understood and still remains to be explored. A possible mechanism to consider is the radiative recombination of electron and hole interband created after photoexcitation, similar to what is seen in gold nanorods.

4.2.3 SR imaging of catalysis and SEM image correlation

Single-particle catalysis with single-turnover resolution experiments were performed in a manner similar to previous studies on smaller (6nm) gold nanoparticles.[11] A typical time trajectory of the fluorescence intensity from a single nanoparticle is shown in Figure 4.5A, which displays the characteristic stochastic on and off behavior of a single nanoparticle catalyst. Each sudden increase in fluorescence intensity marks the formation of one product molecule. The actual chemical transformation cannot be time-resolved with millisecond time resolution since it occurs at subpicosecond time scale. The product molecule remains on the

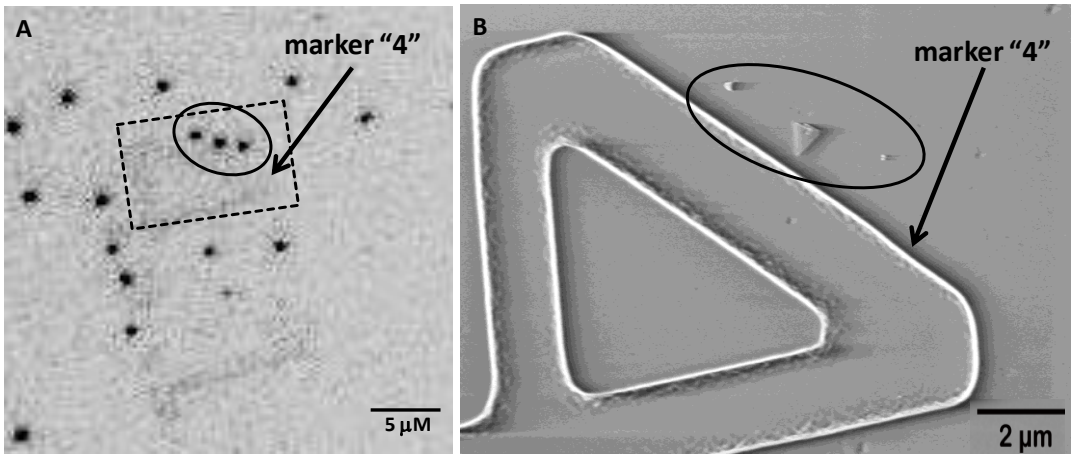

Figure 4.4 Fluorescence and SEM image correlation. (A) Fluorescence image of bio-synthesized gold nanoparticles immobilized on quartz slides with etched markers. The boxed area is the image of an etched marker (marker "4" of "4.1") and inside the oval is the fluorescence image of nanoparticles near marker "4" . (B) SEM image of the area corresponding to the boxed area in panel A, showing the three gold nanoparticles (inside oval), one nanoprism and two pseudo-spherical nanoparticles, near marker "4".

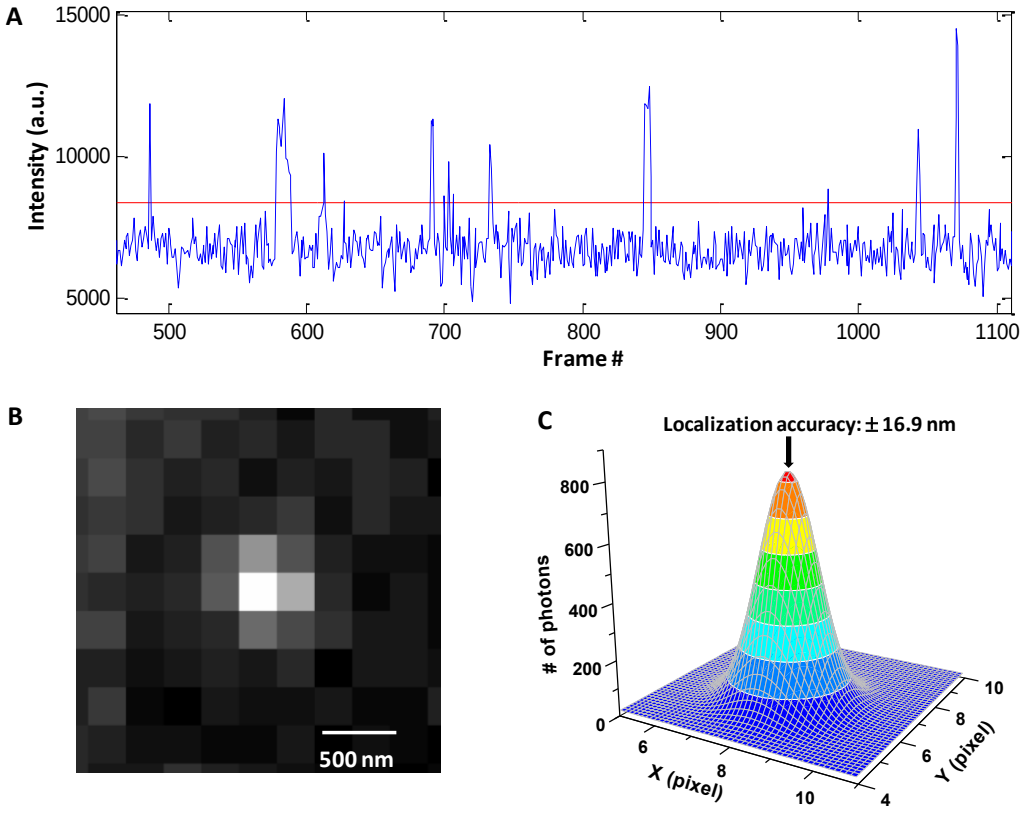

Figure 4.5 SR imaging of the reactive sites on gold nanoparticles. (A) Fluorescecne intensity trajectory of a singe nanoparticle under catalysis. The fluorescence bursts (on-state) correspond to the catalytic generation of resorufin on the surface of the nanoparticle and the off-state is the nanoparticle's own emission (intensity ~6500 a.u.) (B) Conventional wide-field fluorescence image of a single resorufin molecule on the nanoparticle surface during one τ_{on} period (pixel size = 267 nm). (C) Two-dimensional Gaussian fit to the PSF in panel B. The full-width at half-maximum of the fit is ~430 nm and the center localization is determined to ± 17 nm.

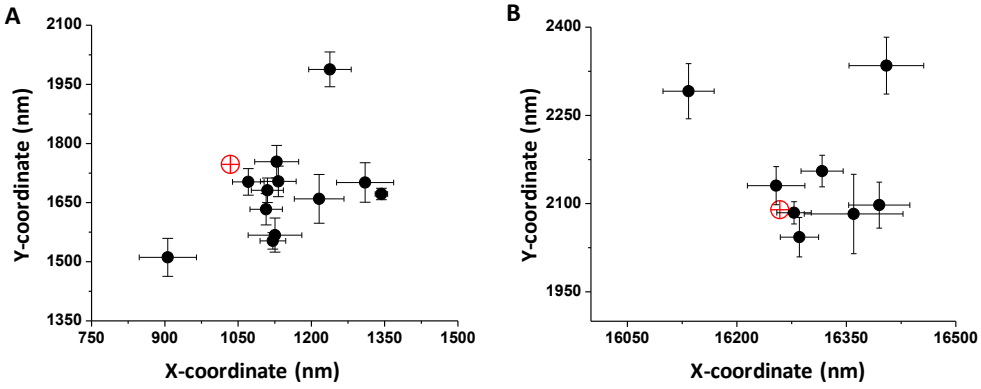

Figure 4.6 (A, B) Scatter plots of positions (•) of catalytic product molecules determined from SR analysis of the fluorescence images from two different nanoparticles. The location of the center of the nanoparticle (⊕) is also shown on each plot.

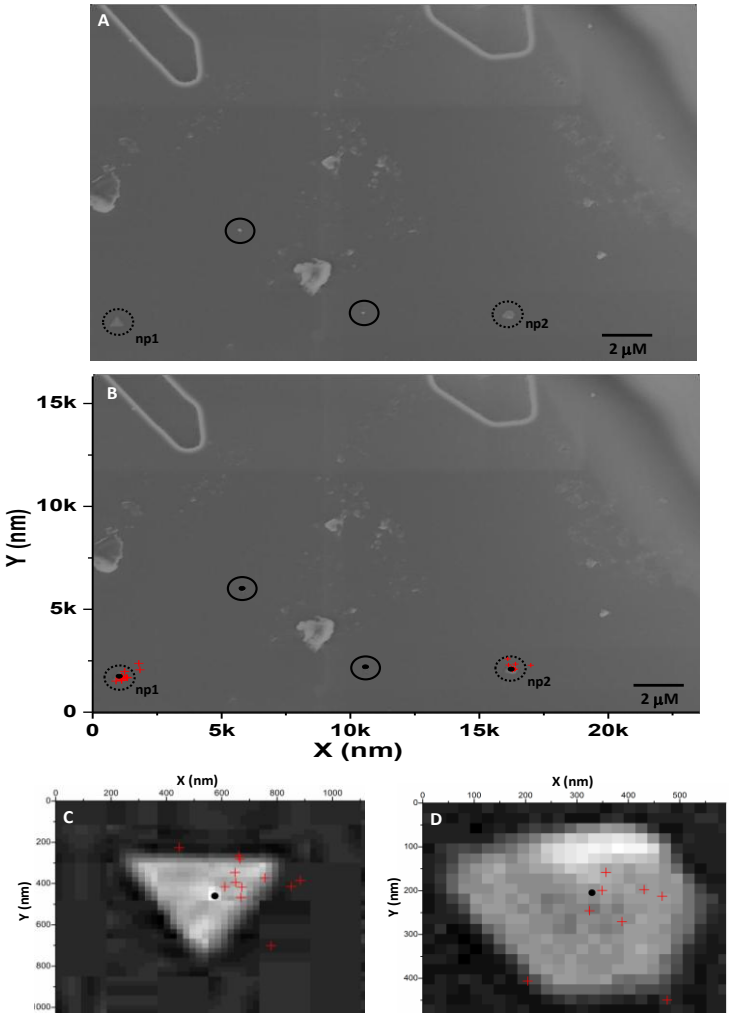

Figure 4.7 Correlated SEM and SR images of gold nanoparticle catalysis. (A) SEM image of gold nanoparticles on etched quartz slide after single molecule fluorescence imaging. Nanoprims *np1* and *np2* are inside dashed-oval and the pseudo-spherical particles are inside solid-oval. Etched markers are shown on the upper part of the image. (B) Overlay of SEM image and the location of the catalytic sites (red cross) obtained from SR imaging of single nanoparticle catalysis. The center of the nanoparticle, also obtained from SR imaging, is shown as solid black dot. (C, D) Zoomed-in SEM image of nanoprism *np1* and *np2* from panel A, with superimposed coordinates for the locations of catalytic product molecules (+) and nanoparticle center (•).

Table 4.1 Overlay of SEM and SR Optical Images[a]

SEM		SR-optical Imaging		Difference		
X	Y	X	Y	ΔX (nm)	ΔY (nm)	ΔDistance (nm)
30808	29192	30800	29209	8	-17	19
54606	27490	54593	27491	12	-1	12
51692	26827	51684	26838.	8	-11	14
55962	13096	55999	13087	-37	9	38
40904	33750	40867	33751	37	-1	37
16240	2092	16221	2090	19	-2	19
1034	1747	1082	1753	48	6	48
10585	2195	10592	2191	7	-4	8
				Mean± s.d.		**24**

[a] First two columns are the center positions (X and Y coordinates) of the nanoparticles in the SEM image. Columns 3 and 4 are the coordinates for the center positions of the nanoparticles obtained from SR-optical imaging. The deviation in the coordinates between the two images are in the last column, calculated from the difference in X and Y position (Columns 5 and 6).

surface of the nanoparticle for the duration of the on-time (τ_{on}) until it dissociates and its intensity decreases. Once the molecule dissociates, it can no longer be detected due to its fast diffusion. The intensity of the off state is not zero since the nanoparticle itself is emissive.

Figure 4.5B is a typical fluorescence image of a product resorufin on the nanoparticle surface. This image was generated by subtracting the background emission of the nanoparticle from the sum of all images during the duration of a single on-time. Subtraction of the nanoparticle's emission was necessary in order to obtain an accurate localization of the product molecule. This point spread function (PSF) was then fitted with the 2D-Gaussian function whose center determines the location where the product is generated (Figure 4.5C), with precision down to a few nm. The precision of localization is primarily determined by the number of photons detected. The more photons collected, the higher the precision of the center of the PSF, and therefore the higher the precision of the location of the emitter (See Materials and Methods Section 4.4.4).[23,25]

The SR-imaging analysis of the PSFs from many τ_{on} periods for a single nanoprism generates the center localizations of the product molecules. Figure 4.6A and B are the scatter plots of these locations, with error bars, for two nanoprisms. Since the nanoprisms are emissive, their center positions (shown as ⊕ in Figure 4.6) were also localized by fitting their PSFs to a two-dimensional Gaussian. Since they have high emission intensities and they don't photobleach (at least for the duration of the experiment), a large number of photons were collected, rendering the localization of their center positions very precise, ~2-3 nm.[23,25] These center positions were used in the alignment of SEM and optical images. The alignment will determine the accuracy of localization of the center positions of the nanoparticle using super-resolution imaging.

Figure 4.7A is the SEM image of the sample that contains the nanoparticles analyzed in Figures 4.6A and B, labeled *np1* and *np2* respectively (inside dashed oval). In the vicinity of the nanoprisms are two pseudo-spherical nanoparticles (solid oval). The etched marker on the upper portion of the image was used to locate this area during both optical and SEM imaging. To overlay SEM and SR-optical images with high accuracy, the center positions of all four nanoparticles, obtained from both imaging methods, were used in the alignment. The positions of the particles in the SEM image were used as fixed references, and the center positions of the same particles obtained from SR-imaging were rotated, translated, and scaled to overlay onto the SEM image. These transformations were then applied to the locations of the catalytic product molecules (in Figure 4.6) to map them on top of the SEM image (See Section 4.4.6). Figure 4.7B shows the result of the image correlation analysis, where the transformed center coordinates (•) of the nanoparticles and the locations (+) of catalytic product molecules from Figure 4.6 are overlaid with the SEM image in Figure 4.7A. Figure 4.7 C and D show the zoomed-in images of the nanoprisms in Figure 4.7B. The center position obtained from SR-imaging (•) correlates well with the center of the nanoparticles in the SEM image. These correlated images also show that the locations (+) of the catalytic product molecules, obtained from SR-image analysis, coincide well with the location of the nanoparticles. This agreement indicates that the fluorescent product molecules are indeed catalytically generated on the nanoparticles. For all overlaid images, the deviation in the center positions of the markers (between SEM and SR-optical images) is 24 ± 15 nm (mean ± s.d.), which was calculated from eight overlaid markers (Table 4.1).

Now that the catalytic reactions can be mapped directly on the nanoparticle structure, the structure-activity correlation can be studied. To the best of my knowledge, this is the first time that a direct spatial correlation of structure and

catalytic reactivity has been achieved on a single nanoparticle catalyst. However, the statistics of the catalytic events obtained from my single-molecule experiment is too low at this moment for detailed analysis of spatially resolved structure-reactivity correlation. The data presented here indicates, nevertheless, that the combined optical/SEM studies are a promising approach for characterizing the catalytic properties of individual nanoparticles at sub-particle spatial resolution.

4.2.4 Pseudo-spherical gold nanoparticles

In this section, SR imaging of the catalysis on pseudo-spherical gold nanoparticles, of 40 nm and 60 nm diameters, were done as proof of principle experiments to show that SR-imaging can also be used to measure the size of the nanoparticle using optical microscopy. Nanoparticles with 40 nm and 60 nm diameters were chosen because they are bigger than the typical spatial resolution for SR-imaging analyses (~20nm) [20-22] but are smaller than the conventional diffraction-limit resolution of optical microscopy (a few hundred of nanometers).

4.2.4.1 Characterization and ensemble activity assay

Figure 4.8 A and B show the TEM images of 40 nm and 60 nm gold nanoparticle with their respective size distributions in Figure 4.8C and D. To test the activity of these spherical nanoparticles towards the fluorogenic reaction, the reduction of resazurin to resorufin,[9,11] ensemble catalytic activity assay was done for 40 nm and 60 nm gold nanoparticle. Both exhibit catalytic activity towards this reaction (data not shown). The substrate concentration dependence of the initial reaction rate, for both 40 nm and 60 nm nanoparticles, was fitted with Langmuir-Hinshelwood rate equation to obtain the values for the substrate adsorption equilibrium constant, *K*, and maximum

reaction rate, $V_{max,}$ and from V_{max}, the effective turnover rate constant k_{eff} is calculated.[31] The fit parameters obtained are: $K \sim 4 \pm 1\ \mu M^{-1}$, $V_{max} \sim 6.63$ nM-s^{-1}, $k_{eff} \sim 180\ s^{-1}$ for 40 nm gold nanoparticles; and $K \sim 1.6 \pm 0.2\ \mu M^{-1}$, $V_{max} \sim 3.32$ nM-s^{-1}, $k_{eff} \sim 300\ s^{-1}$ for 60 nm.

4.2.4.2 Single-molecule experiment and SR imaging

Figure 4.9A shows the negative image of light scattering of the 532 nm laser by 60 nm nanoparticles immobilized on amine-modified quartz slide (particles are dark spots and background is bright). The 40 nm nanoparticle also scatters but with lower intensity than 60 nm under the same illumination power. The 60-nm spherical nanoparticles are emissive as shown in Figure 4.9B, the fluorescence image (negative image) of the same set of 60 nm gold nanoparticle is shown in panel A. Single 40 nm nanoparticle is also emissive but with lower intensity compared to the emission of 60 nm under the same excitation power (18-20 mW focused onto an area of ~ 80 × 40 μm^2). The intensity line profiles of the fluorescence of two representative 60-nm nanoparticles, marked (i) and (ii) in panel B, are shown in Figure 4.9 C and D. Since these particles are smaller than the diffraction limit, their intensity line profiles have diffraction-limited width having a FWHM of ~380 nm. Their emissive nature allowed for the nanoparticles to be located easily for single-nanoparticle catalysis imaging. Their emission also enabled the determination of their center position with high accuracy (within ~3nm) and allowed for the accurate alignment of many particles together to increase statistics of detected catalytic events.

Single particle catalysis with single turnover resolution experiments were carried out using methods similar to previous studies on smaller spherical gold nanoparticles.[11] The fluorescence intensity versus time trajectories obtained for both 40 and 60 nm display the characteristic stochastic on and off behavior of single

nanoparticle catalysis similar to the one shown in Figure 4.5A. Each on-off cycle corresponds to one catalytic turnover. Since the 40 nm and 60 nm nanoparticles are emissive, the off-state intensity is not zero, and the fluorescence signal coming from the catalytic product appears on top of the emission of each nanoparticle.

SR-imaging of the catalytic turnovers on both 40 and 60 nm nanoparticles was carried out following the same procedure used in SR-imaging experiments on gold nanoprisms (Section 4.2.2). Figure 4.10A and B show the scatter plots (with error bars) of the locations of products obtained from a single 40 nm nanoparticle and a single 60 nm nanoparticle, respectively. The center of the nanoparticle, the hollow circle, was obtained from fitting the PSFs of the nanoparticle's intrinsic emission. The center coordinates for each particle were then used to align many particles together; Figure 4.10C and D are the corresponding two-dimensional histograms of all the catalytic product locations. 2D-Gaussian fits of these distributions gave full width half maximum (FWHM) of ~42 nm for ~40 nm for 40- for 60- nm gold nanoparticles, close to the expected physical sizes of the nanoparticles. It is not yet understood why the spatial distribution of product locations seems broader for 40 nm than for 60 nm nanoparticles. More experiments are underway to gain better understanding of the data. To date, control experiments show that the fluorescence signals observed from these experiments, with gold nanoparticles immobilized on amine-coated slide, arise not from the fluorescence of resorufin adsorbed on the particle but rather the ones that adhere to the quartz surface in the vicinity of the particles. This adsorption could be due to resorufin being negatively charged under experimental conditions (pH 7.3), while the amine surface is positively charged.

4.2.5 Potential complications and alternative tactics

Potential fluorescence quenching due to energy transfer could be one reason

why only few catalytic products are detected on the nanoparticle surface.[37-40] Fast dissociation kinetics, where the product molecules leave the nanoparticle faster than the time resolution of a few milliseconds, is another major reason for not detect sufficient events per particle. To circumvent this problem of fast product dissociation, nanoparticles could be coated with porous silica in order to trap the product temporarily after it dissociates from the nanoparticle surface.[41] This coating would make the molecule stay around the nanoparticle longer before it diffuses away into the solution. Furthermore, since metal surface-induced fluorescence quenching is proportional to ~ $1/d^4$ (d = distance of the fluorescent molecule from the surface)[40], the coating thickness could be adjusted to lower the effect of quenching. Both modifications should enable the detection of more catalytic events.

4.3 Summary

With the combined approach of SR optical imaging of single-nanoparticle catalysis and SEM imaging of these nanoparticles, I have shown that catalytic activity of individual particles can be directly correlated to their structure in a spatially resolved manner. Through image correlation analysis, I was able to align, down to ~26 nm accuracy, SR optical imaging and SEM images. For nanoparticles of anisotropic shapes (i.e. nanoprisms), results revealed that each product molecule detected is indeed localized on the nanoparticle surface in the entire duration of the on-time. The locations of these product molecules can provide information on the activity of the different types of surface atoms on the nanoprism. This spatially resolved single-particle structure-activity correlation could provide insights into the fundamental principles governing the reactivity of nanocatalysts. It is expected that this methodology can be applied to study other types of nanoparticle catalysts.

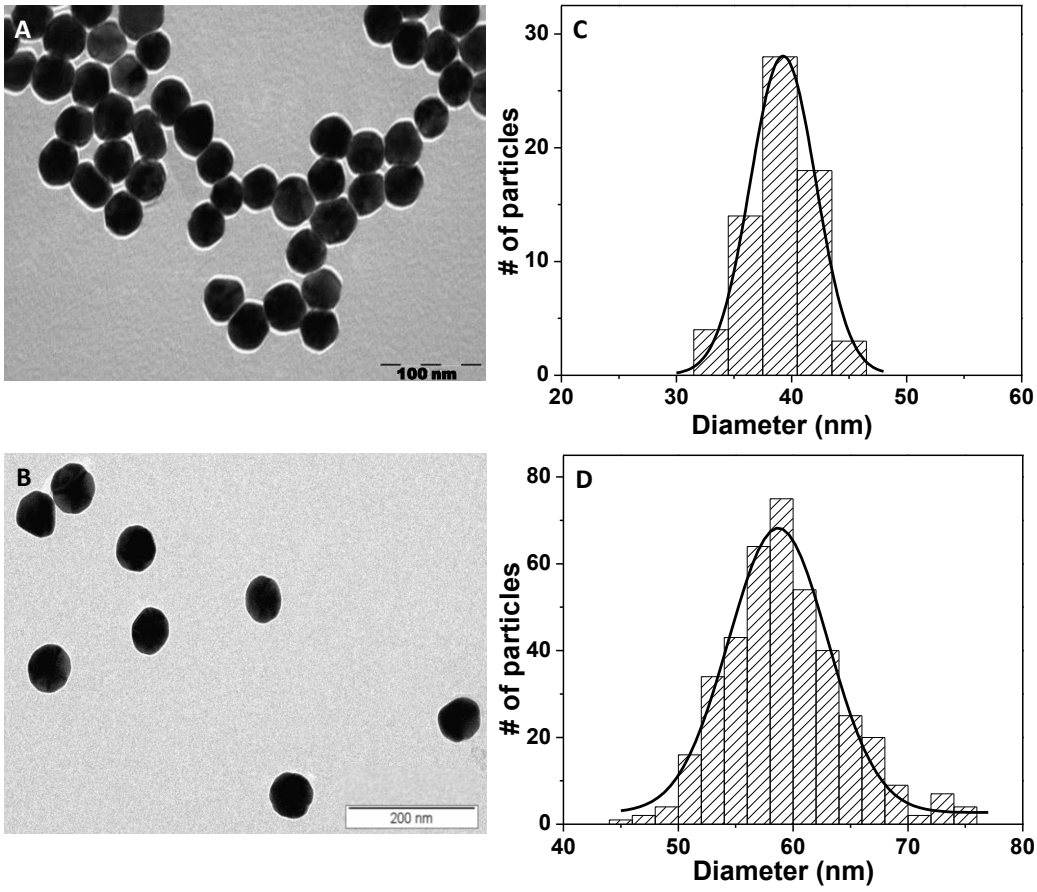

Figure 4.8 TEM images of 40 nm (A) and 60 nm (B) spherical colloidal gold nanoparticles, with their size distribution centered at 39.87 ± 0.1 nm (C) and 58.7 ± 0.2 nm (D), respectively.

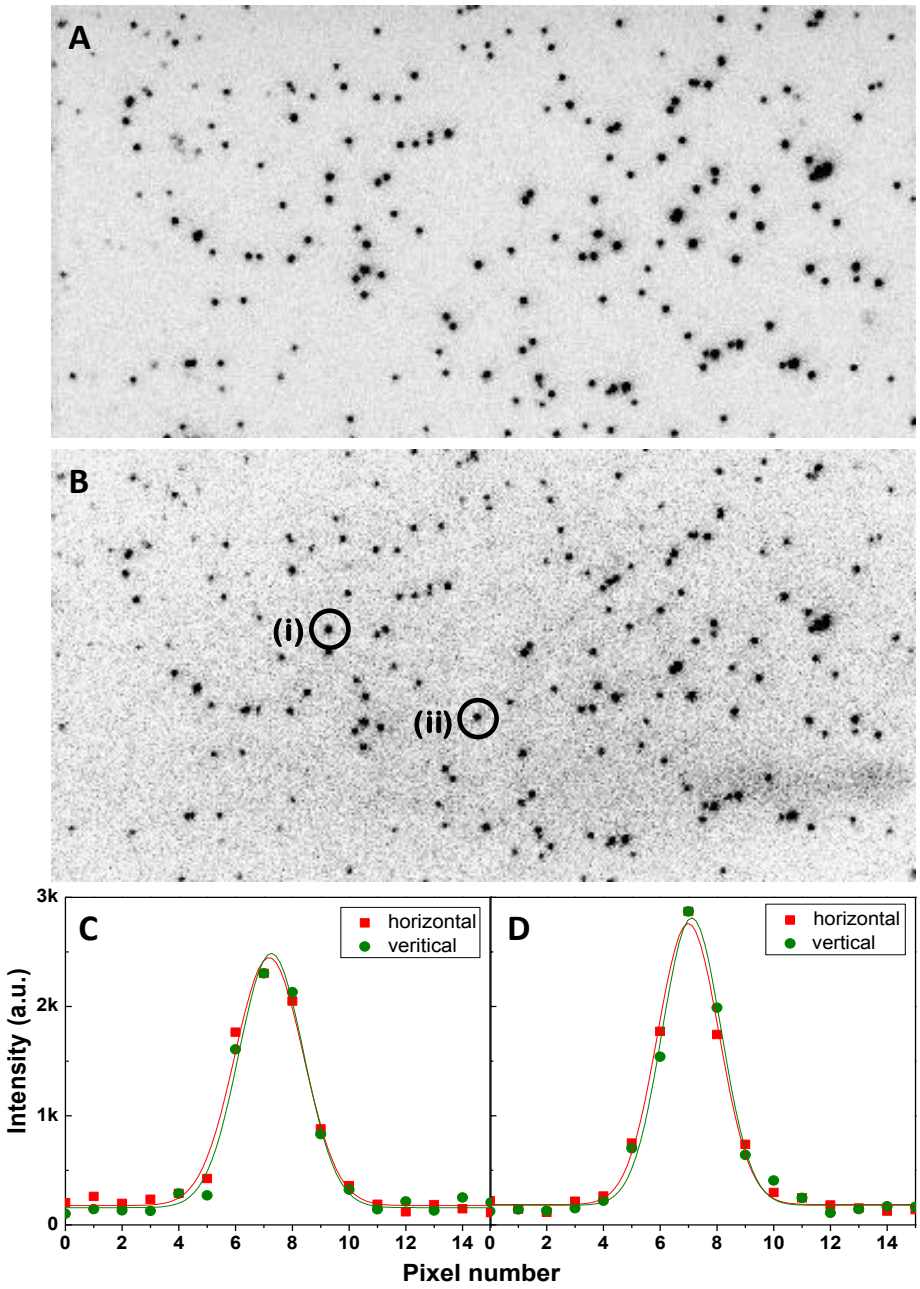

Figure 4.9 Negative scattering (A) and fluorescence (B) images of 60 nm gold nanoparticles immobilized on quartz slide, excited at 532 nm. (C, D) Vertical and horizontal line profiles of the diffraction-limited fluorescence image of single 60-nm gold nanoparticles marked (i) and (ii) in the fluorescence image in (B), with their respective Gaussian fits in solid lines (pixel size = 167 nm fwhm of Gaussian fit ~380 nm).

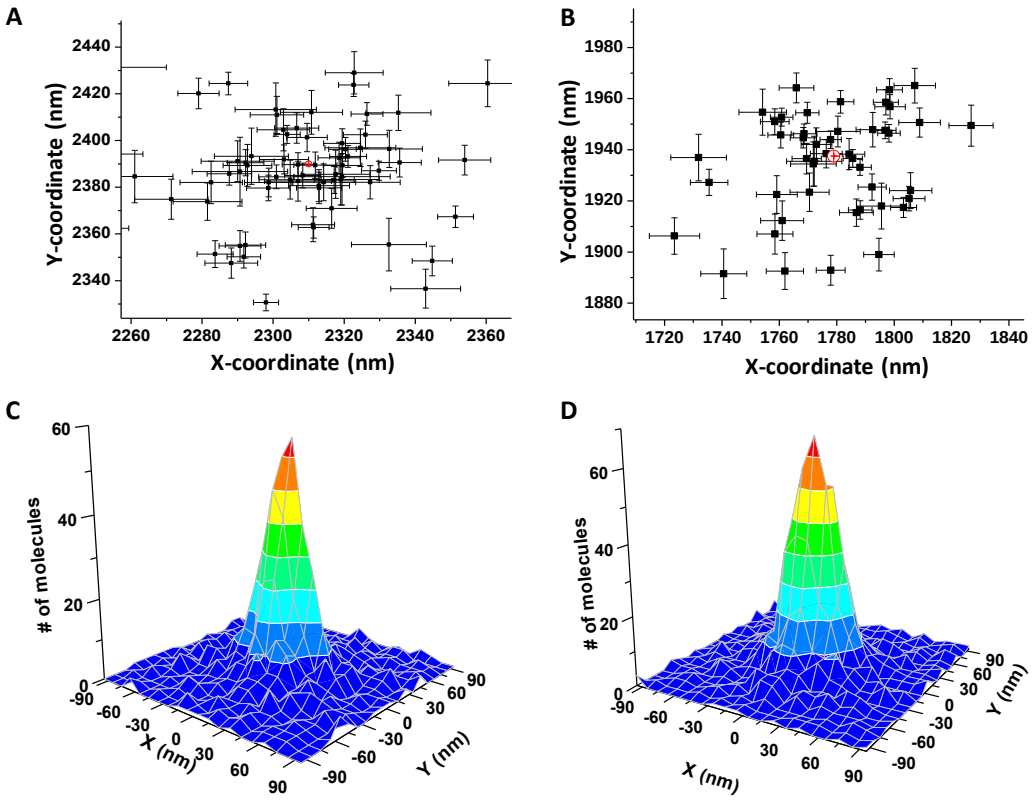

Figure 4.10 SR imaging on pseudo-spherical gold NP. Center localizations determined from many τ_{on} periods on a single (A) 40 nm and (B) 60 nm pseudo-spherical gold NP. The hollow circle represents the center of the particle obtained from localizing the intrinsic emission of the nanoparticle during τ_{off}. Two-dimensional histogram of the locations of all the catalytic product molecules on (C) 40- and (D) 60-nm gold NPs, obtained from overlaying 59 and 93 particles, with FWHM of ~42 nm and ~40 nm, as obtained from 2D Gaussian fits, respectively (bin size = 10 nm). The center of the nanoparticle, obtained from SR imaging of the fluorescence of the particle, was used in the aligning individual particles.

4.4 Materials and Methods

4.4.1 Gold nanoprism synthesis and characterization

Gold nanoprisms were synthesized following the literature.[28] Briefly, 50 g of lemongrass leaves are boiled in 250 mL water for 5 min. After cooling to room temperature, 5.0 mL of the resulting broth was added to 45.0 mL of 1.0 mM $HAuCl_4$ (Sigma) solution and was incubated for at least 6 hours at room temperature. It was then centrifuged at 3400 *g* and the precipitate resuspended in water. Centrifugation and washing cycle was repeated three times.

The spherical colloidal Au nanoparticles (40- and 60- nm in diameter) were obtained from Ted Pella. They had been prepared from a citrate reduction of $HAuCl_4$ (private communication). The bio-synthesized nanoparticles together with the spherical ones were characterized by TEM (FEI Tecnai 12) and SEM (LEO 1550VP FESEM) at the Cornell Center for Materials Research.

4.4.2 Ensemble Catalysis

Catalytic activity of the nanoparticles towards the reduction of resazurin (Invitrogen) to resorufin by NH_2OH (Sigma) was measured at the ensemble level before single molecule experiments were performed. A stock solution of gold nanoparticle was diluted to ~10^{-11} M and was incubated in 1.0 mM NH_2OH, pH 7.35 for ~15 min. The reaction was initiated by adding the substrate, resazurin (~1 to 20 μM), into the nanoparticle solution. UV-Vis absorption of the reaction solution was used to monitor the progress of the reaction.

4.4.3 Single molecule experiment

Single-molecule fluorescence experiments were carried out as previously described.[9,11] A homebuilt prism-type total internal reflection microscope (Olympus IX71) was used in all experiments. A continuous-wave circularly polarized 532nm laser (CrystaLaser) of power ~18-20 mW was focused onto a ~ 80 × 40 μm^2 area of the sample to directly excite the fluorescence of the product resorufin. The fluorescence of resorufin was collected by a 60X NA 1.2 water-immersion objective (Olympus), filtered by two filters (Chroma Technology), to reject the excitation wavelength and scattering of gold nanoparticles, and projected onto an EMCCD camera (Andor Technology), controlled by Andor IQ software. An extra 1.6X magnification on the microscope was also used on occasions. The movies were then analyzed using a custom-written IDL program, which extracted the individual fluorescence intensity trajectories from localized fluorescence spots across the entire movie.[11]

For single-molecule experiments on gold nanoprisms, a flow cell was made from a quartz slide with micron-size markers (to aid in correlating images obtained from single-molecule fluorescence and SEM measurements). The markers are etched on the quartz surface using photolithography performed at Cornell Nanofrabication Facility (Prof. Park's group, Dept. of Chemistry and Chemical Biology, Cornell University) using the following procedure: (i) Vapour prime clean quartz slide with HMDS (Hexamethyldisilazane) using YES furnace; (ii) Spin SPR700-1.2 photoresist (4000 rpm, 5000 r/s, for 30 s); (iii) Bake resist using a hotplate at 115 ^oC for 90 s; (iv) Exposure using Autostep i-line Stepper, AS 200; (v) Develop resist with MIF 300 developer (90 s immersion) using the Hamatech automated wafer processor; (vi) Etched quartz with Oxford Plasma Lab 80+ RIE System using CHF_3/O_2 for 5 minutes in three cycles separated by short O_2 plasma cleans. (vii) Lift-off photoresist by

soaking in hot piranha solution for one hour then soaking in Shipley 1165 Remover solution for an additional 1-2 days.[c]

For the spherical Au nanoparticle, slides without markers were used (Technical Glass or Finkenbeiner). Before flow cell assembly, the slide was amine-functionalized with an aminoalkylsiloxane reagent (Vectabond, Vector Laboratory) for nanoparticle immobilization. To keep the particles spatially separated during single molecule experiments, a low concentration (~10^{-12} M) of nanoparticle solution was flowed in and incubated for 5 min before washing out excess nanoparticles. For gold nanoprisms, non-functionalized slides were used for immobilization; prior to flow cell assembly, 100 μL of ~10^{-11} M of nanoparticle solution was added onto the slide and incubated for 30 min.

4.4.4 SR imaging[d]

Fluorescence images of the individual resorufin product generated on the nanoparticle were analyzed using a custom-made Matlab program that fits the diffraction-limited fluorescence spot with a Gaussian function.[10] This analysis primarily follows the procedure in locating active sites on carbon nanotube but with slight modifications. Specifically, to determine the center of the emission point spread function (PSF) of a single product molecule on the surface of the nanoparticle, an image area of 13 × 13 pixels (~3.5 × 3.5 μm^2) around the particle were used for two-dimensional Gaussian fitting. Since the nanoparticles are also emissive, their fluorescence intensity was first subtracted before fitting. However, for the localization of the center of the nanoparticle, the PSF of the nanoparticle's emission was used

[c] Quartz slides with etched markers were made by Michael Segal from Prof. Park's group, Cornell University.

[d] The MatLab programs used for this section were coded by Xiaochun Zhou.

removing the fluorescence image coming from the product formed on its surface by just fitting τ_{off}.

To localize the product molecules, all image frames in a single τ_{on} period were combined to form a single image, in order to have a large number of fluorescence photons for analysis. Because the camera chip consists of square pixels of finite size, the image is fitted to:[10]

$$I(x,y) = A + Bx + Cy + \int_{x-\delta}^{x+\delta} dx \int_{y-\delta}^{y+\delta} I_o \exp\left[-\frac{1}{2}\left(\frac{x-x_o}{\sigma_x} \right)^2 - \frac{1}{2}\left(\frac{y-y_o}{\sigma_y} \right)^2 \right] dy \quad \text{Equation 4.2}$$

to improve fitting accuracy. Here, *I(x,y)* is the intensity counts of the fluorescent molecule in the image at position (*x*,*y*), $I_o \exp\left[-\frac{1}{2}\left(\frac{x-x_o}{\sigma_x} \right)^2 - \frac{1}{2}\left(\frac{y-y_o}{\sigma_y} \right)^2 \right]$ is the two-dimensional Gaussian function, and δ is half width of the pixel size. Along *x* or *y* axis, the integration over each pixel is done numerically by dividing each pixel into 11 equal segments (further increasing the number of segments does not improve the fitting accuracy). Because the laser excitation in these experiments, *I(x,y)* is not homogeneous over the entire illumination area (note the area analyzed for one molecule is very small relative to the laser beam size), we used a sloping plane A+B*x*+C*y* to account for the background in the fitting. Here (x_0,y_0) represents the center location of the PSF. The accuracy of the center localization was determined according to Thompson et al:[23]

$$Er_i = \sqrt{\frac{\sigma_i^2}{N} + \frac{a^2}{12N} + \frac{8\pi\sigma_i^4 b^2}{a^2 N^2}} \qquad \text{Equation 4.3}$$

Here Er_i (i = *x* or *y*) is the *x* or *y* accuracy of the center location of the PSF, σ_i is of the best two-dimensional Gaussian describing the emission PSF, *N* is the total number of fluorescence photons detected, *a* is the pixel size in the fluorescence image, and *b* is the standard deviation of the background. Provided that a large number of fluorescence photons are detected, Er_i can be as small as 1-2 nm. In these single-molecule experiments, localizations that have accuracy lower than ±20 nm because of insufficient photon counts were filtered out. Similarly, those pixels with peak ellipticity, $\left|2\left(\sigma_x-\sigma_y\right)/\left(\sigma_x+\sigma_y\right)\right|$, greater than 15%, which indicates poor image quality or the possible presence of multiple products formed, were also filtered out. To obtain the number of photons, *N*, detected for each molecule, the total integrated signal counts under the fitted 2D Gaussian function was converted to photon counts, according to the formula provided by the camera supplier (Andor Technology):

$$E_v=\left(cts/g\right)*\left(S/QE\right)*3.65 \qquad \text{Equation 4.4}$$

Here E_V is the total energy of photons, *cts* is the counts from the EMCCD camera (unitless), *g* is EM gain (unitless), *S* is CCD sensitivity (electrons per count) provided by the EMCCD camera manufacturer, QE is the quantum efficiency of the camera in the spectral region of the detected fluorescence, and 3.65 is a physical constant for electron creation in silicon (eV per electron). The total number of photons, *N*, equals the total energy of photons E_V divided by the energy of a single photon, for which the center wavelength of the detected spectral region is used. To obtain the standard deviation of the background, *b*, we first obtain the background image by subtracting the fitted 2-D Gaussian function from the original data image. The counts in the background image were then converted to the number of photons before *b* was calculated.

4.4.5 Scanning electron microscopy (SEM)

After single molecule fluorescence measurements, the flow cell was disassembled for SEM imaging. The surface of the slide was coated with carbon (Edwards Auto 306 Evaporator) to a thickness of less than 10 nm. SEM images were obtained using LEO 1550VP FESEM operated at 2-5 keV. Markers on the surface of the quartz served as guides to locate the area where single-molecule fluorescence movies were taken.

4.4.6 Image correlation analysis

Custom-written Matlab programs were used in image correlation analysis to overlay locations of product molecules from the fluorescence image onto SEM images of nanoparticles. The emission of the nanoparticles was also used as markers (nanoparticle-markers) in image correlation. The alignment used the nanoparticle-markers' positions in the SEM images as fixed references, and coordinates of the same markers obtained from SR-imaging were rotated, translated, and scaled to overlay onto the SEM image. The transformations needed to overlay the markers were then applied to the locations of product molecules to map them on top of the SEM image of the nanoparticle.

REFERENCES

(1) Xu, W. L.; Shen, H.; Liu, G. K.; Chen, P. *Nano Res.* **2009**, *2*, 911-922.

(2) Somorjai, G. A.; Contreras, A. M.; Montano, M.; Rioux, R. M. *Proc. Natl. Acad. Sci. USA* **2006**, *103*, 10577-10583.

(3) Chen, P.; Xu, W. L.; Zhou, X. C.; Panda, D.; Kalininskiy, A. *Chem. Phys. Lett.* **2009**, *470*, 151-157.

(4) Burda, C.; Chen, X. B.; Narayanan, R.; El-Sayed, M. A. *Chem. Rev.* **2005**, *105*, 1025-1102.

(5) Eustis, S.; El-Sayed, M. A. *Chem. Soc. Rev.* **2006**, *35*, 209-217.

(6) Valden, M.; Lai, X.; Goodman, D. W. *Science* **1998**, *281*, 1647-1650.

(7) Choudhary, T. V.; Goodman, D. W. *Applied Catalysis a-General* **2005**, *291*, 32-36.

(8) Narayanan, R.; El-Sayed, M. A. *J. Phys. Chem. B* **2005**, *109*, 18460-18464.

(9) Zhou, X. C.; Xu, W. L.; Liu, G. K.; Panda, D.; Chen, P. *J. Am. Chem. Soc.* *132*, 138-146.

(10) Xu, W. L.; Shen, H.; Kim, Y. J.; Zhou, X. C.; Liu, G. K.; Park, J.; Chen, P. *Nano Lett.* **2009**, *9*, 3968-3973.

(11) Xu, W. L.; Kong, J. S.; Yeh, Y. T. E.; Chen, P. *Nat. Mater.* **2008**, *7*, 992-996.

(12) Xu, W. L.; Kong, J. S.; Chen, P. *Phys. Chem. Chem. Phys.* **2009**, *11*, 2767-2778.

(13) Sun, Y.; Xia, Y. *Science* **2002**, *298*, 2176-2179.

(14) Lee, H.; Habas, S. E.; Kweskin, S.; Butcher, D.; Somorjai, G. A.; Yang, P. D. *Angew. Chem. Int. Ed.* **2006**, *45*, 7824-7828.

(15) Hansen, P. L.; Wagner, J. B.; Helveg, S.; Rostrup-Nielsen, J. R.; Clausen, B. S.; Topsoe, H. *Science* **2002**, *295*, 2053-2055.

(16) Ahmadi, T. S.; Wang, Z. L.; Green, T. C.; Henglein, A.; ElSayed, M. A. *Science* **1996**, *272*, 1924-1926.

(17) Millstone, J. E.; Hurst, S. J.; Metraux, G. S.; Cutler, J. I.; Mirkin, C. A. *Small* **2009**, *5*, 646-664.

(18) Millstone, J. E.; Metraux, G. S.; Mirkin, C. A. *Adv. Funct. Mater.* **2006**, *16*, 1209-1214.

(19) Daniel, M. C.; Astruc, D. *Chem. Rev.* **2004**, *104*, 293-346.

(20) Rust, M. J.; Bates, M.; Zhuang, X. W. *Nat. Method* **2006**, *3*, 793-795.

(21) Hess, S. T.; Girirajan, T. P. K.; Mason, M. D. *Biophys. J.* **2006**, *91*, 4258-4272.

(22) Betzig, E.; Patterson, G. H.; Sougrat, R.; Lindwasser, O. W.; Olenych, S.; Bonifacino, J. S.; Davidson, M. W.; Lippincott-Schwartz, J.; Hess, H. F. *Science* **2006**, *313*, 1642-1645.

(23) Thompson, R. E.; Larson, D. R.; Webb, W. W. *Biophys. J.* **2002**, *82*, 2775-2783.

(24) Zurner, A.; Kirstein, J.; Doblinger, M.; Brauchle, C.; Bein, T. *Nature* **2007**, *450*, 705-708.

(25) Yildiz, A.; Selvin, P. R. *Account Chem. Res.* **2005**, *38*, 574-582.

(26) Ghosh, R. N.; Webb, W. W. *Biophys. J.* **1994**, *66*, 1301-1318.

(27) Roeffaers, M. B. J.; De Cremer, G.; Libeert, J.; Ameloot, R.; Dedecker, P.; Bons, A. J.; Buckins, M.; Martens, J. A.; Sels, B. F.; De Vos, D. E.; Hofkens, J. *Angew. Chem. Int. Ed.* **2009**, *48*, 9285-9289.

(28) Shankar, S. S.; Rai, A.; Ankamwar, B.; Singh, A.; Ahmad, A.; Sastry, M. *Nat Mater* **2004**, *3*, 482-488.

(29) Millstone, J. E.; Park, S.; Shuford, K. L.; Qin, L. D.; Schatz, G. C.; Mirkin, C. A. *J. Am. Chem. Soc.* **2005**, *127*, 5312-5313.

(30) Satterfield, C. N. *Heterogeneous catalysis in practice*; McGraw-Hill: New York, 1980.

(31) Xu, W. L.; Kong, J. S.; Chen, P. *J. Phys. Chem. C* **2009**, *113*, 2393-2404.

(32) Mohamed, M. B.; Volkov, V.; Link, S.; El-Sayed, M. A. *Chem. Phys. Lett.* **2000**, *317*, 517-523.

(33) He, H.; Xie, C.; Ren, J. *Anal. Chem.* **2008**, *80*, 5951-5957.

(34) Geddes, C. D.; Parfenov, A.; Gryczynski, I.; Lakowicz, J. R. *Chem. Phys. Lett.* **2003**, *380*, 269-272.

(35) Wilcoxon, J. P.; Martin, J. E.; Parsapour, F.; Wiedenman, B.; Kelley, D. F. *J. Chem. Phys.* **1998**, *108*, 9137-9143.

(36) Eustis, S.; El-Sayed, M. *J. Phys. Chem. B* **2005**, *109*, 16350-16356.

(37) Nerambourg, N.; Werts, M. H. V.; Charlot, M.; Blanchard-Desce, M. *Langmuir* **2007**, *23*, 5563-5570.

(38) Lakowicz, J. R. *Anal. Biochem.* **2001**, *298*, 1-24.

(39) Dulkeith, E.; Ringler, M.; Klar, T. A.; Feldmann, J.; Javier, A. M.; Parak, W. J. *Nano Lett.* **2005**, *5*, 585-589.

(40) Chhabra, R.; Sharma, J.; Wang, H. N.; Zou, S. L.; Lin, S.; Yan, H.; Lindsay, S.; Liu, Y. *Nanotechnology* **2009**, *20*.

(41) Joo, S. H.; Park, J. Y.; Tsung, C.-K.; Yamada, Y.; Yang, P.; Somorjai, G. A. *Nat Mater* **2009**, *8*, 126-131.

CHAPTER FIVE

CONCLUDING REMARKS

Optical detection of single molecules has found a wide range of applications in many scientific disciplines. The work in this thesis has shown that single-molecule fluorescence detection has helped address important and new problems about protein-DNA interactions, enzyme catalysis, as well as catalysis on nanostructured materials. Different single-molecule fluorescence detection strategies were used in studying these systems: (i) smFRET for protein-DNA interactions, (ii) single-probe fluorescence quenching for enzyme catalysis, and (iii) super-resolution imaging of fluorogenic reactions for nanoparticle catalysis.

5.1 Protein-DNA Interactions

Protein-DNA interaction dynamics and changes on DNA structures upon protein binding define the functions of many gene regulatory proteins. In Chapter 2 of this thesis, CueR-DNA interaction dynamics was studied with the use of engineered DNA HJ and smFRET detection. The single-molecule kinetic analysis of HJ structural dynamics in the presence and absence of CueR has helped in elucidating the functional differences between apo- and holo-CueR. To be able to define these differences is essential since the interplay between these two forms helps in maintaining copper homeostasis. In addition, being a member of the MerR-family of regulators, CueR is proposed to induce only subtle structural changes on DNA which are challenging to measure using the conventional smFRET experiments. These subtle structural changes were detected when engineered HJ was used as the smFRET reporter and differences in the structures between HJ bound to apo- and holo-CueR were also distinguished.

The use of engineered HJs as smFRET reporters provides a new tool to

elucidate the correlation of structure, dynamics and function of DNA-binding proteins. This methodology could be applied to many other DNA-binding proteins. The HJ can be designed to specifically bind to any protein of interest by changing the sequences encoded in its arms, making this methodology applicable to other DNA-binding proteins. In addition, since protein-induced changes on DNA are converted and amplified by the changes in the structure and dynamics of the HJ, proteins that only induce small structural changes on DNA can now be studied.

5.2 Single-molecule enzymology

In Chapter 3, catalysis-coupled fluorescence quenching (CCFQ) was used to study the single-molecule enzymology of tyrosinase. This methodology directly probes the active site of the enzyme which has a binuclear-copper center. Direct probing of the active site bridges the gap between monitoring substrate binding and that of product generation, two of the most common methods used in single-molecule enzymology.

Aside from tyrosinase, CCFQ can also be applied to a wide variety of enzymes that have catalytic intermediates with strong absorption features. The development of site-directed mutagenesis has made site-specific labeling of proteins achievable. Many fluorescent probes that cover a wide spectral range have also become readily available. Combining all these, CCFQ can efficiently be applied to probe the versatile chemistry of transition-metal-based biological catalysts, since they often exhibit intense ligand-to-metal charge transfer absorptions. However, single-molecule kinetic analysis of the fluorescence trajectories showed that the intrinsic photophysical properties of the probe significantly affect the observed intensity fluctuations. This then requires the need for a photo-stable, nonblinking fluorescent probe for applications using single-molecule CCFQ.

5.3 Super-resolution imaging of nanoparticle catalysis

The catalytic properties of metal nanoparticles are generally controlled by their sizes and shapes. Unfortunately, the synthetic methods available to date could not generate metal nanoparticles with identical structures. It is therefore necessary to correlate catalytic activity and structure of metal nanoparticles on a single-particle level. The fourth chapter of this work presented a methodology developed to achieve this goal.

The emergence of super-resolution imaging techniques using single-molecule fluorescence microscopy has made it possible to localize with high precision the center positions of multiple emitters concentrated within a diffraction limited area. This methodology has been applied to spatially resolve catalytic sites on single nanoparticle catalysts. As successive catalytic reactions on a single particle do not overlap in time, precise nanometer-localizations of where the fluorescent products are generated provided the locations of these catalytically active areas on the nanoparticle surface. Correlating the reconstructed super-resolution images with those obtained from SEM imaging (of the same set of nanoparticles) allowed the direct correlation of the structure and activity of nanocatalysts on a single-particle level. This methodology could be applied to study other nanoparticle catalysts and correlate their structural features with catalytic activity. Structure-activity correlation of bulk heterogeneous catalysts could also be examined using this methodology.